ANGLE-RESOLVED PHOTOEMISSION SPECTROSCOPY OF EPITAXIALLY STRAINED RUTHENATES

A Dissertation

Presented to the Faculty of the Graduate School

of Cornell University

in Partial Fulfillment of the Requirements for the Degree of

Doctor of Philosophy

by

Bulat Burganov

January 2017

ANGLE-RESOLVED PHOTOEMISSION SPECTROSCOPY OF EPITAXIALLY STRAINED RUTHENATES

Bulat Burganov, Ph.D.

Cornell University 2017

Complex oxides provide a platform for designing new functional material systems and manipulating the properties of the existing ones thanks to a vast array of their tunable and exotic ground states. The interactions between the internal degrees of freedom in such systems often cannot be fully accounted for by modern theory, and it is necessary to directly probe the electronic structure underlying a complex phase to reveal its nature. The emergent properties of ruthenates are particularly tunable, as evidenced by their wide variety of electronic and magnetic instabilities including unconventional superconductivity, metamagnetism and formation of electronic liquid crystalline states, ferro- and antiferromagnetism, and spin-glass behavior. Some of these phases occur in closely related compounds, or are switchable within the same compound by a small external perturbation, such as pressure, strain or magnetic field. This dissertation presents direct measurements of the electronic structure in Ba_2RuO_4 and $BaRuO_3$, close analogues of the spin-triplet superconductor Sr_2RuO_4 and ferromagnetic $SrRuO_3$, respectively, using a unique integrated oxide molecular-beam epitaxy and angle-resolved photoemission spectroscopy. This approach allows us to access compounds that have no stable bulk form and deliberately manipulate their electronic properties via epitaxial strain and dimensionality confinement.

We first discuss the ARPES measurements of Ba_2RuO_4 and Sr_2RuO_4. By varying the amount of biaxial in-plane strain through epitaxial stabilization on different substrates, we reveal a systematic evolution of the Fermi surface and quasiparticle mass enhancements. We

reveal a topological transition in the circular electron Fermi pocket centered at zone center as a function of strain and cation size. Near the topological Lifshitz transition, we observe clear signatures of quantum criticality. The quasiparticle mass enhancements are found to increase rapidly and monotonically with increasing Ru-O bond distance. By next studying atomically thin films of $BaRuO_3$ we are able to directly see how the dimensional confinement drives the transition from a ferromagnetic ground state to a strongly fluctuating paramagnetic state. Our results provide new insights into the physics of perovskite ruthenates and demonstrate the possibilities for using epitaxial strain and dimensional confinement as disorder-free means of manipulating emergent properties and many-body interactions in correlated quantum materials.

Biographical Sketch

Bulat Burganov was born and grew up in Kazan, a city in Russia. From an early age he benefitted greatly from his parents' home library, mainly cherry-picking popular books on popular science and engineering, among which Yacov Perelman's books on Popular physics take a special place. He was extremely fortunate to have Nail Afletonov as his physics teacher at high school, who sparked his interest in Physics and gave the first glimpse of the basic constituents of scientific research method. As a result of their project, Bulat won the first prize at a regional conference and was granted an exam-free admission to Kazan State University. That allowed him to get his first exposure to experimental research with a group at Kazan State University collecting and analyzing geophysical data in oil fields in Tatarstan, Russia. But his dream then was to study at Moscow Institute of Physics and Technology, the famous PhysTech. The dream came true, and a student at MIPT, Bulat performed research at the Lebedev Physical Institute and, later, at the Radio-Technical Institute of Russian Academy of Sciences and was awarded a Mintz fellowship for excellent studies. He graduated *summa cum laude* from MIPT with Bachelor of Science and, later, Master of Science degrees in Applied Physics and Mathematics. After graduation in 2008, he started working as a quantitative trader at Barclays Capital in London alongside other Math and Physics (mostly PhD) graduates. It did not take long before he realized that physics was more exciting and he went to graduate school at Cornell University. He joined Professor Kyle Shen's group where the exciting cutting edge research was performed on angle-resolved photoemission spectroscopy of thin films grown by molecular-beam epitaxy. The results of research performed in this laboratory form his doctoral dissertation presented here.

To my family.

Acknowledgments

I am grateful to a number of people who supported me throughout the graduate school at Cornell, and without whose help this thesis would not have been possible. I am immensely grateful to my advisor, Kyle Shen, for his support, advice and guidance, and for letting me pursue my interests in research. I was fortunate to work with the team of exceptionally talented and bright people. I am truly grateful to John Harter, Eric Monkman and Daniel Shai who were the first members of Kyle's group and showed me the ropes of ARPES measurements and data analysis. I was taught a great deal about ARPES and oxide film growth by a number of brilliant postdocs in Kyle Shen's and Darrell Schlom's groups, including Yuefeng Nie, Arsen Soukiassian, Phil King, Masaki Uchida, Yang Liu, Jason Kawasaki and Carolina Adamo. I am deeply grateful to Carolina Adamo and Hanjong Paik for heroically growing the metastable phases of Ba_2RuO_4 and $BaRuO_3$ studied in this thesis. I would like to appreciate Andrew Mulder for performing the density functional theory calculations. It has been a great pleasure to work with Shouvik Chatterjee, Ed Lochocki, Haofei Wei, Jacob Ruf, Brendan Faeth, and Jocienne Nelson.

Bulat Burganov

August 2016

Table of Contents

List of Figures

List of Tables

CHAPTER 1

Introduction

The deep connection between structural and electronic degrees of freedom in the strongly correlated electron materials hints to an attractive route for fine-tuning the macroscopic physical properties of these materials, controlling the phase transitions, as well as rationally designing the entirely novel electronic systems. Some examples of such structural controlling knobs available in experiment are physical or chemical pressure and strain, dimensionality and interface engineering, and epitaxial strain. Often what makes a correlated system highly tunable is its intrinsic proximity to a phase transition, or availability of nearly degenerate ground states. While there is an exhaustive experimental record of structure-property relations for many of such systems, there is still a fundamental shortage of the direct spectroscopic evidence of how microscopic many-body degrees of freedom respond to the structural perturbations. Our understanding here is mostly based on theoretical modeling, however, for some important cases the theoretical description is still unsettled. Pressure plays a key role in modifying the properties of materials with strong electronic correlations, for instance, enhancing the transition temperature of the cuprate superconductors or driving quantum phase transitions in heavy fermion systems. Unfortunately, leading techniques for investigating the electronic structure, such as ARPES and STM, are incompatible with typical high pressure / strain apparatus. The epitaxial growth of thin films on deliberately lattice mismatched substrates provides a clean and accessible analogue to external pressure and has been used to dramatically alter the electronic phases of many complex oxides [1–4].

In the family of ruthenium oxides, the strong structure-property relationship leads to a

wide variety of ground states including unconventional superconductivity[5], metamagnetism and electronic liquid crystalline states [6–8], ferromagnetism, antiferromagnetism and spin-glass behavior [9–11], without changing the formal oxidation state of the Ru ion. We chose to study the $n = 2$ members of Ruddlesden-Popper series of ruthenates, Sr_2RuO_4 and Ba_2RuO_4, and the perovskites $SrRuO_3$ and $BaRuO_3$ as ideal examples of correlated materials with high structural tunability and proximity to various electronic instabilities. The ground state of Sr_2RuO_4 is spin-triplet superconductor and the interest in this material stems from the possibility of topological superconductivity and proposals for application in stable topological quantum computations. The normal state, from which the exotic superconductivity condenses, is a moderately correlated Fermi liquid. Some very high-level questions concerning the superconducting state in Sr_2RuO_4 are still unsettled, such as identification of the band with the largest gap, identification of the primary fluctuations responsible for pairing, existence of related compounds with the same ground state. The perovskites $SrRuO_3$ and $BaRuO_3$ are ferromagnets that exhibit signatures of both itinerant band magnetism and strong local moments. While a number of factors affecting ferromagnetic transition temperature and the saturation moment are known, there is still no single consistent picture of how ferromagnetism responds to changes in the structural degrees of freedom and parameters of the band structure. These ground states result from a delicate interplay between strong itinerancy of the extended Ru-4*d* orbitals, the local Coloumb correlations enhanced by the Hund's rule coupling, and the spin-orbit interaction.

We employ the structural tuning in three distinct ways. First, we substitute Ba for Sr, which inhibits the octahedral rotations on the surface of A_2RuO_4 and the bulk of $ARuO_3$. This greatly simplifies the band structure in both cases due to the increased symmetry of the structures. We use epitaxial strain to systematically study the evolution of the many-body interactions and the Fermi surface as a function of biaxial strain. Lastly, we use dimensional confinement of $BaRuO_3$ thin films to reveal the suppression of the ferromagnetic state and

emergence of fluctuating paramagnetic phase. We then investigate the role of the proximity of the van Hove singularity to the Fermi level. The vHs has been suggested to be responsible for the enhancement of superconductivity under application of uniaxial strain, stronger mass renormalization in the quasi-two-dimensional band in Sr_2RuO_4, and ferromagnetism in $SrRuO_3$. Since this role of the vHs was never confirmed experimentally, we perform a controlled study where the changes in quasiparticle properties are measured in response to the varations of the vHs energy.

CHAPTER 2

Angle-Resolved Photoemission Spectroscopy

Angle-resolved photoemission spectroscopy (ARPES) is the primary experimental technique used in this thesis. It has evolved as a probe of condensed matter systems since nearly a hundred years ago and continues to be remarkably fruitful. In this chapter, we review the history of photoemission as experimental technique. We then discuss the theory of the photoemission process, overview some details of the experimental setup, and discuss the aspects of measurements and data analysis.

2.1 History of photoemission spectroscopy as a probe of condensed matter systems

2.1.1 Photoelectric effect

Photoemission spectroscopy is based on the photoelectric effect - emission of electrons from the surface on absorption of incident photons. This effect was discovered by Hertz in 1887 [12]. Hertz was working on the experiments on generation of electrical oscillation with the setup consisting of two arcs. He noticed that the ultraviolet radiation emitted by one of the arcs triggered the other arc. In the following years, Hallawachs used continuous light sources instead of arcs and studied the influence of light on electrostatically charged bodies. He found that negatively charged plates discharged when exposed to the UV light, while the positively charged did not [13]. These results were puzzling at the time, since the concept of

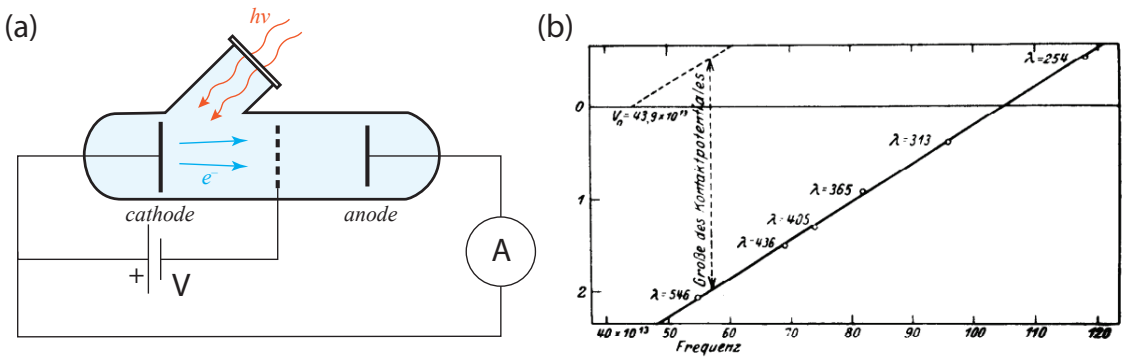

Figure 2.1: (a) Typical setup for measurement of the photoelectric effect. (b) Data measured by R. Millikan for verification of Einstein's equation.

electron was unknown. Only a decade later J. J. Thompson [14], when studying the nature of cathode rays, discovered that the cathode rays were made up of tiny identical particles with negative charge. Later, the experiments on photoemission were refined by P. Lenard [15], who made systematic measurements of dependence on the intensity and frequency of incident light. He concluded that the number of emitted electrons was proportional to the light intensity, whereas their kinetic energy depended only on its frequency. This seemingly contradicted Maxwell's theory of electromagnetism, according to which the intensity of electromagnetic waves is directly related to the energy they carry.

In 1905, Albert Einstein was able to explain the systematics of these experiments by proposing that light was not a wave propagating through space but a beam of discrete wave packets[16]. The energy carried by these wave packets, or photons, is quantized, and the quantum of energy depends on the frequency of light $E = \hbar\omega$. This relation was earlier used by Max Planck to explain the spectrum of black body radiation but had no physical interpretation. Einstein's famous equation relates the maximum kinetic energy of the emitted electron to the frequency of absorbed light ω:

$$eU = E_{\text{kin,max}} = \hbar\omega - \phi,$$

where U is the retarding voltage, and ϕ is the metal-specific *work function*. The work function

is the part of energy that's needed to surmount the potential barrier near the surface to escape from the solid. Einstein was awarded Nobel prize in 1921 for explaining the photoelectric effect. A schematic drawing of the photoemission experiment (used e.g. by Lenard) and typical experimental data are shown in figure 2.1. Einstein's equation was experimentally confirmed by Robert A. Millikan in 1916 [17]. By using a versatile vacuum chamber, in which he could prepare a clean alkali metal surface by cutting thin slices from large pieces of material, he could confirm the linear dependence of the retarding voltage as a function of light frequency ω and show that the slope was independent of the specific metal. From the slope he could experimentally determine Planck's constant $\hbar$. Millikan was awarded the Nobel prize for his work in 1923. Later theoretical advances came from G. Beck [18], G. Wentzel [19] and R. Oppenheimer [20], who simultaneously submitted reports all dealing with the theory of the photoeffect and angular distribution of electrons.

2.1.2 History of photoemission spectroscopy

Photoemission was first used as a probe in 1921 by de Broigle, who confirmed Einstein's relation at high photon energies. The rapid development and application of the technique began after 1950, when two significant instrumental improvements helped establish photoemission spectroscopy as a probe for the study of atoms, molecules and solids. Kai Siegbahn developed a high resolution x-ray photoemission spectrometer in early 1950's to measure photoemission data for many solids and gases [21–23]. In the 1960's D. Turner built the first differentially pumped helium discharge lamp. This development helped to bring the experimental resolution to about 20 meV [24–26]. Starting in 1958, Berglund and Spicer measured band gaps and electron affinities and the first valence band spectra of metals by photoemission experiments in a series of groundbreaking works [27].

Lower vacuum levels accessible in measurement chambers enabled studying surface and

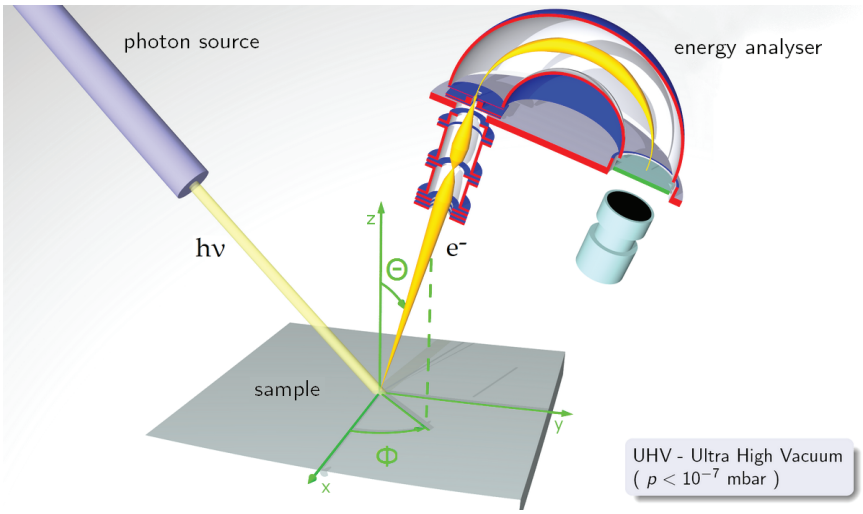

Figure 2.2: Schematic drawing of ARPES experiment.

bulk states separately. Compared to the early years, when photoemission was considered almost purely a surface effect, the focus started to shift towards the bulk photoemission, due to understanding that it is directly related to the electronic band structure of metals and semiconductors. The first angle-resolved measurements on Si and Ge were carried out by Gobeli, Allen and Kane in1964 [28; 29], that laid the path to direct investigation of the band structure of solids. Since the discovery of high-temperature cuprate superconductors in 1980's, ARPES was immensely useful in determining their unconventional nature and the gap symmetry. To this day, ARPES is a unique experimental tool that allows to directly study some of the most exotic state of electronic matter, like superconductivity, topological states, etc. In addition to energy and angular resolution, the modern capabilities include electron spin resolution, time resolution down to picosecond time scales.

2.2 The theory of photoemission

2.2.1 Kinematics of the photoemission process

Angle-resolved photoemission spectroscopy provides direct information about the electronic band structure of solids. In a typical ARPES experiment, a beam of monochromatic radiation from either a gas-discharge lamp or synchrotron beamline is incident on a sample surface (Figure 2.2). The electrons are emitted into vacuum in all directions. The energy and emission angle of the photoemitted electron can be related to the binding energy and crystal momentum of the electrons in solid, respectively, by energy and momentum conservation laws. The electron can be emitted from the solid if its energy exceeds the binding energy of the electron E_B and the potential barrier between the sample surface and vacuum, or work function ϕ. Within the non-interacting electron picture, the kinetic energy can be used to measure its binding energy:

$$E_{\text{kin}} = h\nu - \phi - E_B,$$

Figure 2.3 represents the relation between the energy levels of electron in the solid and the measured spectrum (i.e. number of photoemitted electron vs kinetic energy).

The momentum of the photoelectron in vacuum can be related to the momentum of the electron in the solid via momentum conservation laws. The magnitude of the photoelectron momentum in vacuum is determined from its kinetic energy by $K = \sqrt{2mE_{kin}}$, where m is the electron mass. Spatial components are given in terms of the polar (θ) and azimuthal (ϕ) emission angles:

$$K_x = \sqrt{2mE_{kin}} \sin\theta \cos\phi,$$

$$K_y = \sqrt{2mE_{kin}} \sin\theta \sin\phi,$$

$$K_z = \sqrt{2mE_{kin}} \cos\theta.$$

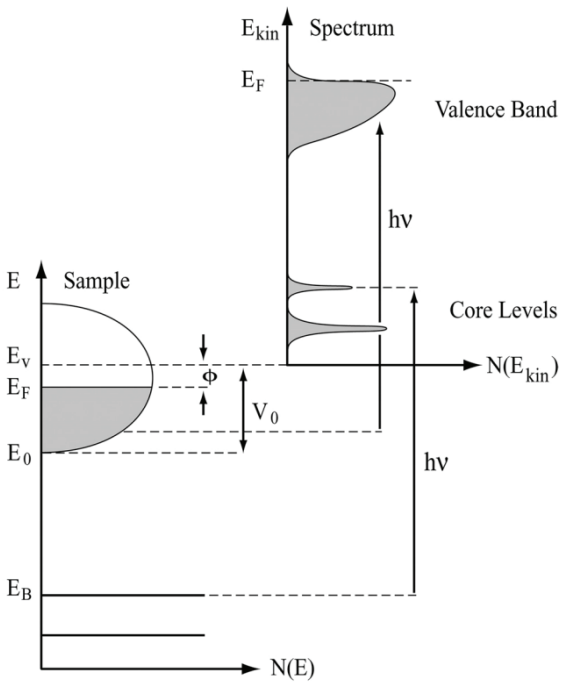

Figure 2.3: Relation of energy bands within the solid to the energy of the photoelectron.

To relate this to the original momentum in the crystal, we invoke the momentum conservation: $\mathbf{k}_f - \mathbf{k}_i = \mathbf{k}_{h\nu}$. For the typical UV photon energies used in ARPES, $h\nu \simeq 100$ eV, photon momentum is much smaller than the typical Brillouin zone size $2\pi/a$, and can be neglected. Then the transition between the initial and final states can be described by a direct transition in the reduced-zone scheme, $\mathbf{k}_f - \mathbf{k}_i = 0$, or, equivalently, by a transition between momentum points connected by a reciprocal-lattice vector $\mathbf{G}$ in the extended-zone scheme, $\mathbf{k}_f - \mathbf{k}_i = 0$.

The sample surface breaks the translational symmetry of the crystal in the direction perpendicular to it, so the out-of-plane momentum $\mathbf{k}_\perp$ is not conserved during the emission. On the contrary, the in-plane momentum $\mathbf{k}_\parallel$ is conserved:

$$k_{i,\parallel} = k_{f,\parallel} = \sqrt{2mE_{kin}} \cdot \sin\theta,$$

where $k_{i,\parallel}$ is the in-plane crystal momentum in the extended-zone scheme. At higher angle θ one actually probes higher order Brillouin zones. Figure 2.4 illustrates the kinematics of the

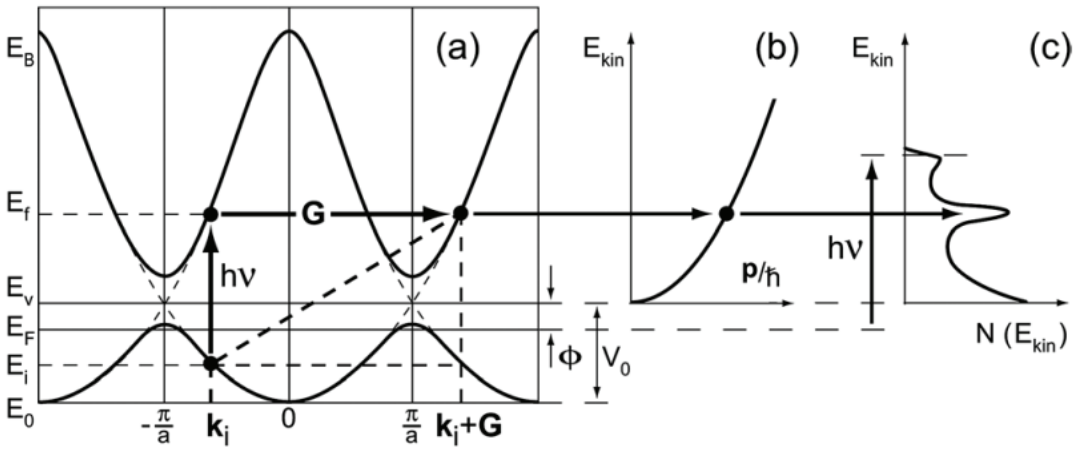

Figure 2.4: Kinematics of photoemission in three-step model

photoemission process. Determination of the out-of-plane crystal momentum $\mathbf{k}_\perp$ is, in general, more complex. Direct measurement requires additional experimental data [30], or making some simplifying assumptions about the electron final states. The simplest is nearly-free-electron model, where the electron energy in the final state within the solid is given by:

$$E_f(\mathbf{k}) = \frac{\mathbf{k}^2}{2m} - E_0 = \frac{\mathbf{k}_\parallel{}^2 + k_\perp^2}{2m} - E_0.$$

The energy of the final state in solid differs from E_{kin} in vacuum by work function ϕ. Perpendicular component of momentum is given by

$$k_\perp = \sqrt{2m(E_{kin}\cos^2\theta + V_0)},$$

where the inner potential, V_0, is the difference between the vacuum level E_v and the bottom of the valence band E_0, $V_0 = E_0 + \phi$. By counting the number of electrons emitted with particular energy and at particular angle, one can use the above equation to map the dispersion of electrons in the solid – energy as a function of momentum $E(\mathbf{k})$. In practice, V_0 is usually unknown, and one can use photon energy dependent mappings and use periodicity **G** of the photoemission in reciprocal space to determine V_0. When the band dispersion is low-dimensional, for example, in case of Sr_2RuO_4, where the electron motion is

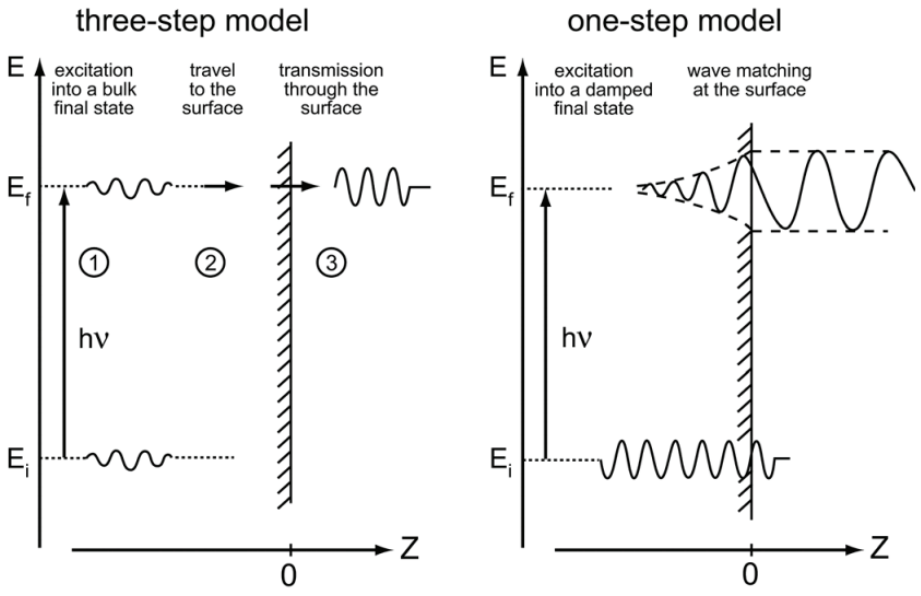

Figure 2.5: One-step and two-step descriptions of photoemission.

confined to RuO_2 planes and dispersion along k_z is negligible, the uncertainty in $\mathbf{k}_\perp$ is less relevant, and dispersion is solely determined by $\mathbf{k}_\parallel$. We will use the above equations to analyze the periodic intensity modulations of photoemission along k_z from the quantum-well states in ultra thin films of $BaRuO_3$.

2.2.2 Three-step model of the photoemission

The full quantum mechanical description if the photoemission process is extremely complex. Quantitative analysis of experimental data is typically performed under the simplifying assumptions of the *independent-particle picture* and the *sudden approximation* (i.e. assuming that the system response to the creation of the photohole is instantaneous and there is no interaction between the escaping electron and the rest of system).

The optical transition between the initial Ψ_i^N and final Ψ_f^N many-body states is driven by interaction H_{int} with the absorbed photon. The initial state is N-electron ground state, and

the final state is $(N-1)$-electron state (or one hole) and the photoelectron. Assuming a small perturbation H_{int} the transition probability is calculated by Fermi's Golden Rule, which gives

$$w_{if} = \frac{2\pi}{\hbar}|\langle\Psi_f^N|H_{int}|\Psi_f^N\rangle|^2\delta(E_f - E_i - h\nu),$$

where $E_i^N = E_i^{N-1} - E_B(\mathbf{k})$ and $E_f^N = E_f^{N-1} + E_{kin}$ are the initial and final state energies of the N-electron system, $E_B(\mathbf{k})$ is the binding energy of the photoelectron with momentum $\mathbf{k}$. The interaction with the photon H_{int} is treated in the usual way by transforming the momentum operator to include the electromagnetic field $\mathbf{p} \rightarrow \mathbf{p} - \frac{e}{c}\mathbf{A}$ in the unperturbed Hamiltonian, where $\mathbf{p}$ is the electronic momentum operator and $\mathbf{A}$ is the electromagnetic vector potential. The scalar potential can be set to zero by choosing the convenient gauge $\Phi = 0$. By using the dipole approximation $\nabla \cdot \mathbf{A} = 0$, which holds when the wavelength is large relative to the atomic dimensions, and neglecting quadratic term $\mathbf{A} \cdot \mathbf{A}$, which is only relevant for very high intensities of the exciting radiation, the interaction can be written as

$$H_{int} = \frac{e}{2mc}(\mathbf{A} \cdot \mathbf{p} + \mathbf{p} \cdot \mathbf{A}) = \frac{e}{mc}\mathbf{A} \cdot \mathbf{p}.$$

The dipole approximation works well for the bulk, but may not hold at the surface, where strong electric fields may develop due to discontinuity of the crystal. To evaluate the probability of the photoemission written above, one has to consider a single coherent process involving photon absorption, electron removal, and electron detection [31; 32]. This view is the so called *one-step model*, in which the Hamiltonian should include bulk of the crystal, its surface and vacuum. However, due to the complexity of the one-step picture, photoemission process is usually considered as a three-step process, where the steps are independent and sequential: 1) optical excitation of the electron in the bulk, 2) transport of the excited electron to the surface, and 3) escape of the photoelectron into vacuum. The total photoemission current is then given by the product of three independent factors: the probability of the optical transition, the scattering probability for the electrons traveling to the surface, and the transmission probability through the surface potential barrier. The three-step model,

introduced by Berglund and Spicer [27], is purely phenomenological but has proven rather useful in practice.

To evaluate the probability of the first step it is convenient to factorize the initial and final state wavefunctions into photoelectron and $(N-1)$-electron terms. This can only be done if the photoemission is considered *sudden*, i.e. the interactions between the photoelectron and the remaining system after the photoionization are neglected. The final state can be written as

$$\Psi_f^N = \mathcal{A}\phi_f^k \Psi_{f,m}^{N-1}$$

where $\mathcal{A}$ is an antisymmetric operator that properly antisymmetrizes the N-electron wavefunction to satisfy the Pauli principle, ϕ_f^k is the wavefunction of photoelectron with momentum k, and $\Psi_{f,m}^{N-1}$ is the m^{th} excited $(N-1)$-electron state of the remaining system. The total probability is the sum over all excited states. The *sudden approximation* does not hold, however, for electrons with low kinetic energy, since the system starts relaxing before the photoelectron escapes the solid. In this case, or *adiabatic limit*, the wavefunctions cannot be factorized into two independent parts and the screening of the photoelectron and photohole have to be considered. For the initial state, the factorization is simply $\Psi_i^N = \mathcal{A}\phi_i^k \Psi_i^{N-1}$, where the $(N-1)$-state is obtained by acting with annihilation operator c_k on the N-electron state: $\Psi_i^{N-1} = c_k \Psi_i^N$. Then, the transition matrix element can be written as

$$\langle \Psi_f^N | H_{int} | \Psi_i^N \rangle = \langle \phi_f^k | H_{int} | \phi_i^k \rangle \langle \Psi_m^{N-1} | \Psi_i^{N-1} \rangle$$

The two factors on the r.h.s. are, respectively, $M_{f,i}^{\mathbf{k}} = \langle \phi_f^{\mathbf{k}} | H_{int} | \phi_i^{\mathbf{k}} \rangle$ – the one-electron dipole matrix element, and $c_{m,i} = \langle \Psi_m^{N-1} | \Psi_i^{N-1} \rangle$ – the probability that the system is left in the m^{th} excited state. In the non-interacting electron picture, only one of the $c_{m,i}$ coefficients is non-zero for a particular $m = m_0$. On the contrary, for strongly-correlated systems, since Ψ_i^{N-1} is not an eigenstate of $(N-1)$-electron system after removal of photoelectron, it will

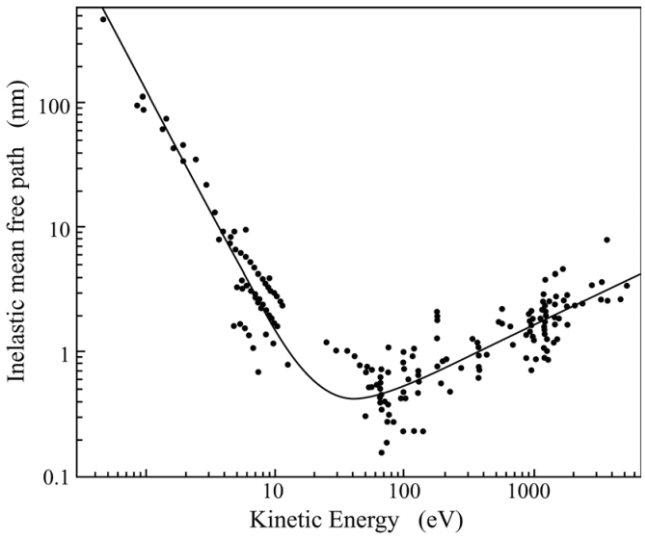

Figure 2.6: Inelastic mean-free path as a function of kinetic energy of the photoelectron. Reprinted from [33].

overlap with many excited states, so that many of the $|c_{m,i}|$ will be non-zero. The total photoemission intensity as a function of E_{kin} and momentum $\mathbf{k}$ is given by

$$I(E_{kin}, \mathbf{k}) \propto \sum_{f,i} |M^{\mathbf{k}}_{f,i}|^2 \sum_{m} |c_{m,i}|^2 \delta(E_{kin} + E^{N-1}_m - E^N_i - h\nu)$$

In the second step, during the transport of the photo-excited electrons to the surface of the crystal they experience elastic and inelastic scattering with some probability. Inelastic scattering contributes to the non-dispersive continuous background in the measured spectra, which can be calculated using a specific model (for example, [34]) or estimated directly from the spectra and subtracted. Elastic scattering makes distinct contribution only at high electron energies and the high incident photon energies. Only the photoelectrons that did not undergo scattering during transport to the surface can be used to extract the original dispersion relations in the crystal. As a result of scattering, electrons lose kinetic energy by exciting secondary electrons, phonons and plasmons. This limits the the escape depth of photoelectrons λ, the so-called *inelastic mean free path* (IMFP). The intensity of the electrons

emitted from depth d is given by

$$I(d) = I_0 \exp(-\frac{d}{\lambda}).$$

The energy dependence of the inelastic mean free path was measured by Seah and Dench [33]. IMFP values are roughly material independent and follow the so-called "universal curve" (Figure 2.6).

In most ARPES measurements, performed in vacuum ultraviolet (VUV) range, the typical electron kinetic energies are 10-100 eV, and, thus, their mean free path is about 1 nm, or about 2-3 monolayers for a perovskite crystal. The finite escape depth modifies the final-state wave function by a dampening factor:

$$\phi(z) = \frac{1}{\sqrt{\lambda}} \exp(ik_z^0 z) \exp(z/2\lambda).$$

In the momentum space this leads to line broadening in the k_z direction:

$$|\phi(k_z)|^2 \propto \frac{1}{\lambda} \frac{1}{(k_z - k_z^0)^2 - (1/2\lambda)^2}.$$

2.2.3 Many-body interactions and spectral function

To quantitatively describe the photoemission from strongly interacting electron systems, where many of the $|c_{m,i}|^2$ are different from zero, the most commonly used approach is based on Green's function formalism [35–37]. The particle propagation is described in terms of the one-electron Green's function, $\mathcal{G}(\mathbf{k}, t - t')$, which can be interpreted as the probability amplitude that an electron added to the system with momentum $\mathbf{k}$ at time zero will still be in the same state after a time $|t - t'|$. By taking the Fourier transform, we can express the Green's function in energy-momentum representation. The removal of an electron from the N-particle system at $T = 0$ is then given by

$$G^-(\mathbf{k}, \omega) = \sum_m \frac{|\langle \Psi_m^{N-1} | c_\mathbf{k} | \Psi_i^N \rangle|^2}{\omega - E_m^{N-1} + E_i^N - i\eta}$$

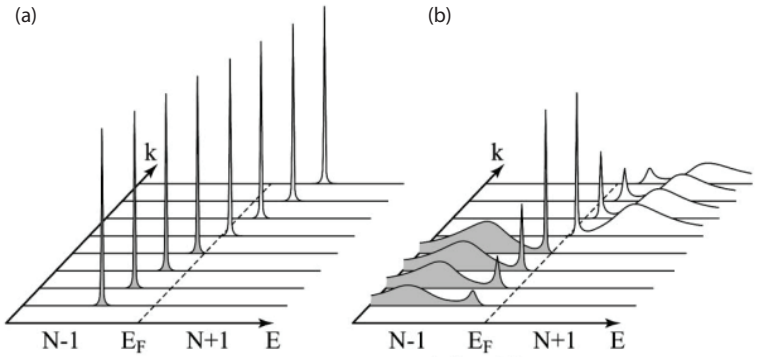

Figure 2.7: Momentum-resolved spectral function for (a) a non-interacting electron system, and (b) an interacting Fermi-liquid system. Reprinted from [38].

where η is a positive infinitesimal. The *spectral function* for removal of one particle can be obtained in the limit $\eta \to 0^+$

$$A^-(\mathbf{k},\omega) = \frac{1}{\pi}\mathrm{Im}G^-(\mathbf{k},\omega) = \sum_m |\langle \Psi_m^{N-1}|c_\mathbf{k}|\Psi_i^N\rangle|^2 \delta(\omega - E_m^{N-1} + E_i^N)$$

The measured ARPES intensity within the sudden approximation is then given by

$$I(\mathbf{k},\omega) = I_0(\mathbf{k},\nu) f(\omega) A^-(\mathbf{k},\omega),$$

where $I_0(\mathbf{k},\nu)$ is proportional to the squared one-electron matrix element $|M_{f,i}^\mathbf{k}|^2$ and $f(\omega) = (e^{\omega/kT}+1)^{-1}$ is the Fermi function. The corrections to one-electron propagator from the many-body interactions can be expressed in terms of the complex self-energy:

$$\Sigma(\mathbf{k},\omega) = \Sigma'(\mathbf{k},\omega) + i\Sigma''(\mathbf{k},\omega)$$

that contains all information on energy renormalization and lifetime of an electron with momentum $\mathbf{k}$ and dispersion $\epsilon_\mathbf{k}$. The Green's function is then expressed as $G(\mathbf{k},\omega) = (\omega - \epsilon_\mathbf{k}^0 - \Sigma(\mathbf{k},\omega))^{-1}$ and the spectral function is

$$A(\mathbf{k},\omega) = -\frac{1}{\pi}\frac{\Sigma''(\mathbf{k},\omega)}{[\omega - \epsilon_\mathbf{k}^0 - \Sigma'(\mathbf{k},\omega)]^2 + [\Sigma''(\mathbf{k},\omega)]^2}.$$

Calculation of spectral function is, in general, a rather difficult task. We will briefly discuss the spectral function of a Fermi liquid, relevant for the analysis of ARPES spectra of

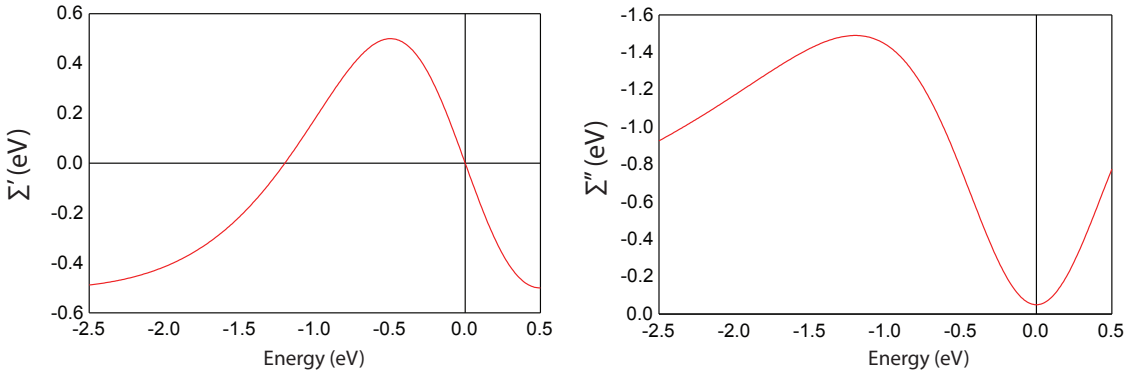

Figure 2.8: Real and imaginary parts of self-energy of a Hund's metal.

the ruthenates. In the trivial case of a non-interacting system, the self-energy is $\Sigma(\mathbf{k}, \omega) = 0$, and the spectral function is given by

$$A(\mathbf{k}, \omega) = \frac{1}{\pi}\delta(\omega - \epsilon^0_{\mathbf{k}}).$$

This corresponds to sharp peaks at energies satisfying the bare band dispersion $\omega = \epsilon^0_{\mathbf{k}}$ (Figure 2.7 (a)). In this case, the occupation numbers at specific momenta $n_{\mathbf{k}\sigma} = c^\dagger_{\mathbf{k}\sigma} c_{\mathbf{k}\sigma}$ are good quantum numbers and for a metallic system the momentum distribution is characterized by a discontinuous drop from 1 to 0 at $\mathbf{k} = \mathbf{k}_F$, which defines a sharp Fermi surface.

In the Fermi liquid model the electron-electron interactions are turned on adiabatically and the scattering rates are small. The spectral function then has a sharp peak of width $2\Sigma''(\mathbf{k}, \omega)$ corresponding to *coherent quasi-particles* at renormalized energy $\epsilon_{\mathbf{k}} = \epsilon^0_{\mathbf{k}} + \Sigma'(\mathbf{k}, \omega)$ with finite lifetime, and a smooth *incoherent* background created by the continuum of the particle-hole excitations (Figure 2.7 (b)). We can linearly expand the real part of self energy in ω: $\omega - \epsilon^0_{\mathbf{k}} - \Sigma'(\mathbf{k}, \omega) \approx Z^{-1}_{\mathbf{k}}(\omega - \epsilon_{\mathbf{k}})$ where $Z_{\mathbf{k}} = (1 - \partial\Sigma'/\partial\omega)^{-1}$ is the quasiparticle residue and write

$$A(\mathbf{k}, \omega) = Z_{\mathbf{k}} \frac{\Gamma_{\mathbf{k}}/\pi}{(\omega - \epsilon_{\mathbf{k}})^2 + \Gamma^2_{\mathbf{k}}} + A_{incoh},$$

where $\Gamma_{\mathbf{k}} = Z_{\mathbf{k}}|\Sigma''|$ is the quasiparticle lifetime broadening. It must be noted that the Fermi

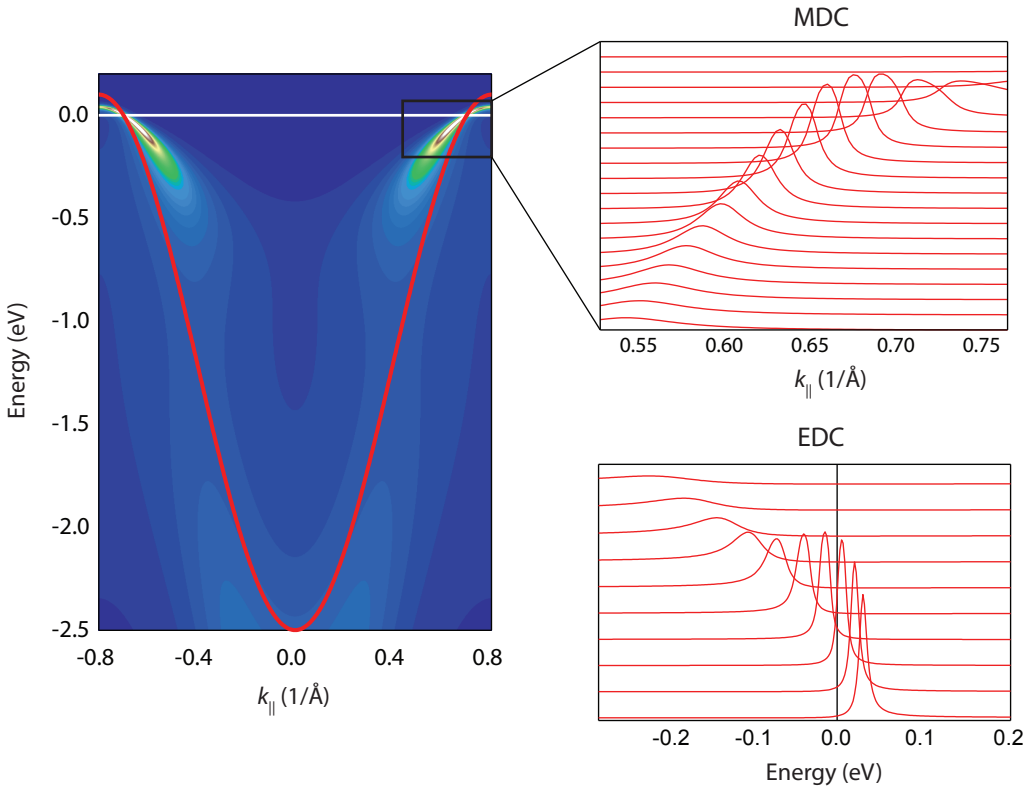

Figure 2.9: Spectral function of a Hund's metal. Momentum and energy distribution curves.

liquid description is valid only in the vicinity of the Fermi surface, and under condition $|\Sigma''(\mathbf{k},\omega)| \ll \epsilon_{\mathbf{k}} - \mu$. The quasiparticle residue is proportional to mass renormalization, and if the dispersion is linear, $\epsilon_k = v_F \cdot (k - k_F)$, it can be determined form the velocity ratio:

$$Z = \frac{v_F^0}{v_F}.$$

For a Fermi liquid at a finite temperature the lifetime broadening due to electron-electron interaction follows quadratic energy and temperature dependence: $\Gamma \propto (\pi k_B T)^2 + (\epsilon_{\mathbf{k}} - \mu)^2$. Figure 2.8 shows the real and imaginary parts of model self energy fitted to experimental dispersion of Sr_2RuO_4 from [39]. At low energy ω, the self-energy follows the Fermi liquid form: $\Sigma^{FL} \propto \alpha\omega + i\beta\omega^2$. The band is strongly renormalized at low energies but the total bandwidth is almost unaffected, which is characteristic of electronic correlations arising from Hund's rule coupling [40], discussed more in the next chapter. The corresponding spectral function is shown in figure 2.9.

2.2.4 Effects of matrix elements and finite resolution

For a quantitative analysis of ARPES spectra one must take into account the effects of finite experimental resolution, the matrix elements and background. The measured intensity is

$$I(\mathbf{k},\epsilon) = [I_0(\mathbf{k}, h\nu, \mathbf{A})\frac{1}{1+\exp(\frac{\epsilon-\epsilon_F}{k_B T})}A(\mathbf{k},\epsilon) + background] * R(\Delta\epsilon)Q(\Delta\mathbf{k}),$$

where B is the background, $R(\Delta\epsilon)$ and $Q(\Delta\mathbf{k})$ are the energy and momentum resolution functions. For accurate extraction of the quasiparticle dispersion near the Fermi level one must determine the Fermi energy ϵ_F, temperature T and energy and momentum resolutions. The first three quantities can be found my measuring reference spectra of well a studied metal, and fitting the spectra to the model intensity. In the work presented here, polycrystalline gold was used as reference measurement (Figure 2.10). $I_0(\mathbf{k}, h\nu, \mathbf{A}) \propto |M_{f,i}^{\mathbf{k}}|^2$ is

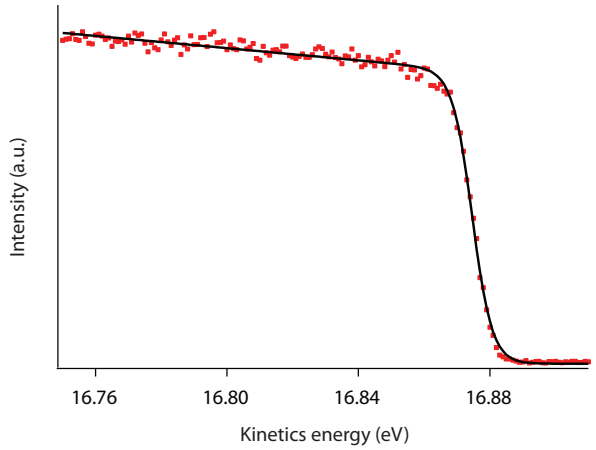

Figure 2.10: Reference photoemission spectrum edge from gold.

the factor coming from one-electron matrix element and depends on the symmetry of the band and light direction, polarization and wavelength, and the photoelectron momentum. In the dipole approximation it can be estimated as

$$|M^{\mathbf{k}}_{f,i}|^2 \propto |\langle \phi_{\mathbf{k},f}|\mathbf{A}\cdot\mathbf{p}|\phi_{\mathbf{k},i}\rangle|^2,$$

however, usually the dipole approximation does not yield accurate estimate and the matrix element effect can be eliminated by measuring spectra in the neighboring Brillouin zones.

Quasiparticle band structure can be determined from analyzing the momentum distribution curves (MDC) and energy distribution curves (EDC), shown as example in figure 2.9. The model spectral function $A(\omega,\mathbf{k}) = Z_{\mathbf{k}}/\pi\ \Gamma_{\mathbf{k}}/((\omega-\epsilon_{\mathbf{k}})^2+\Gamma^2_{\mathbf{k}})$ multiplied by the Fermi function and broadened by instrumental resolution is fitted MDC's and EDC's at fixed energies ω or momenta $\mathbf{k}$, respectively. The pole positions give information about the renormalized dispersion $\epsilon_{\mathbf{k}}$ and the line width – about the $\Gamma_{\mathbf{k}}$, or $\Sigma''(\omega)$. The self energy is an analytic function of energy and its real and imaginary parts are related via Kramers-Kronig transformation:

$$\Sigma'^{(''')}_{\mathrm{KK}}(\omega) = \pm\frac{1}{\pi}\mathcal{P}\int_{-\infty}^{\infty}\partial\omega'\frac{\Sigma''^{(')}(\omega')}{\omega'-\omega}.$$

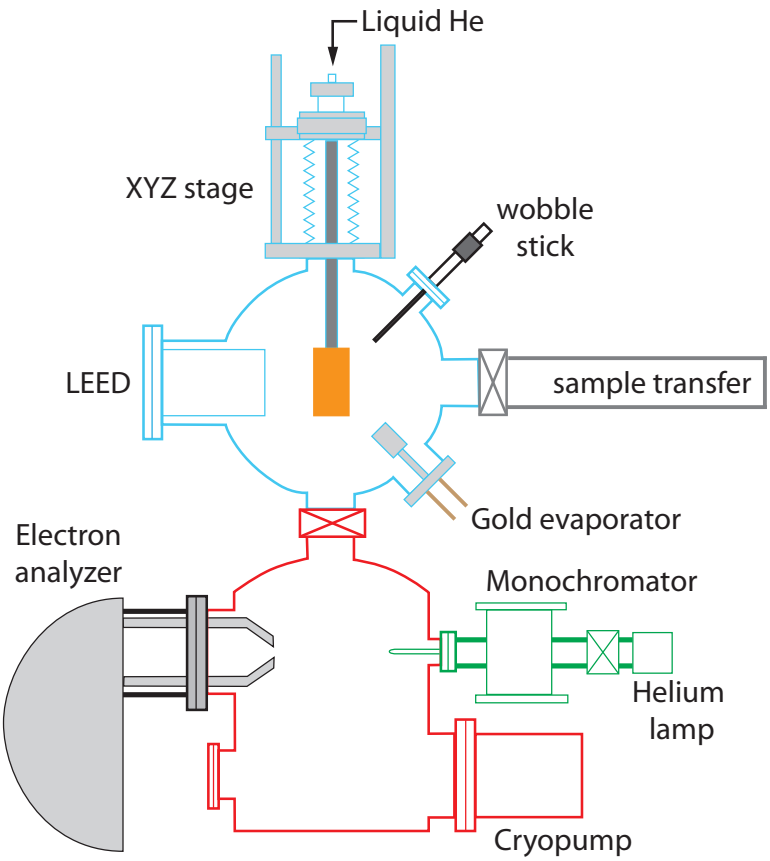

Figure 2.11: The schematic of ARPES setup at Cornell University.

Since only the electron-removal spectral function is measured in ARPES, it is necessary to make additional assumptions to use the formula above. Sufficiently close to the Fermi level the assumption of electron-hole symmetry usually holds and, thus, the full complex self energy can be found by measuring the lifetime broadening as a function of energy. In this work, the experimentally determined quasiparticle dispersions, related to bare band dispersions by $\epsilon_{\mathbf{k}} = Z_{\mathbf{k}}\epsilon^0_{\mathbf{k}}$, were used to calculate the real parts of self-energy. The LDA bands were used for bare band dispersions $\epsilon^0_{\mathbf{k}} = \epsilon^{LDA}_{\mathbf{k}}$. After that the KK relations were used to determine the imaginary part.

2.3 Experimental considerations

In this section we describe some experimental aspects of performing ARPES measurements and some technical details of the experimental setup developed and built at Cornell. The defining characteristic of the system at Cornell is integration of molecular-beam epitaxy (MBE) growth chamber with angle-resolved photoemission spectroscopy in a single ultra-high vacuum setup. Figure 2.11 shows the general schematic of the system excluding the MBE chamber, which is briefly discussed in the following chapters. The system consists of an upper and lower vacuum chambers separated by a gate valve and maintained at $\sim 4 \times 10^{-11}$ Torr pressure. The upper chamber is used for sample transfer, sample preparations, e.g. gold and alkali evaporation, and low-energy electron diffraction (LEED) measurements. The lower chamber is used for APRES and XPS measurements. The samples are inserted into the upper chamber via intermediate transfer chamber, maintained at $\approx 10^{-10}$ Torr, from either MBE system or the load lock. The single crystal samples can be cleaved either in the transfer chamber at an elevated pressure or in the upper chamber.

2.3.1 Surface sensitivity

In ARPES measurement, performed in VUV light range, only a few subsurface atomic layers are probed. For this reason, the technique is extremely surface sensitive and the chamber must be maintained at UHV pressures. Some estimates (for example in [30]) show that at 10^{-9} Torr pressure the full monolayer forms on the surface of the sample within 1000 seconds, assuming the sticking coefficient of 1. Thus, for a typical measurement lasting several days, the necessary pressure would have to be more than two orders of magnitude better. The sticking coefficient is usually much less than one, so the pressure of $\sim 10^{-11}$ Torr is enough to perform meaningful measurements. However, the sample surface evolution must be closely monitored during such measurements.

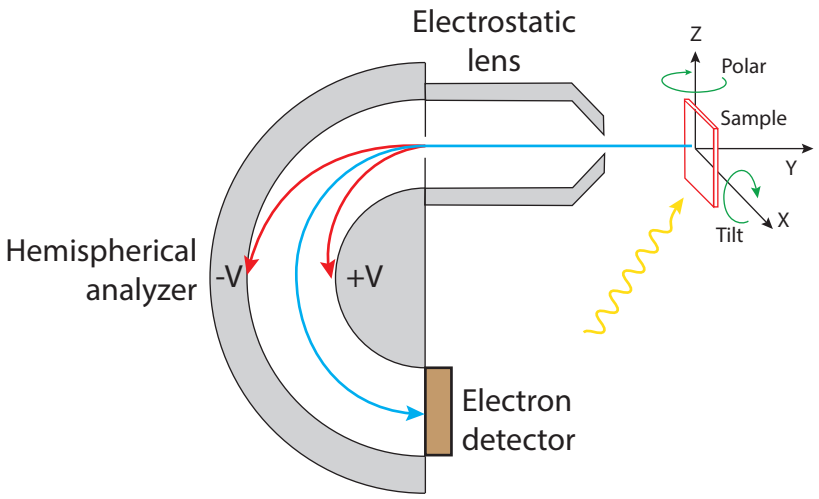

Figure 2.12: Hemispherical analyzer.

2.3.2 Light sources

The light source used in this setup consists of a commercial Scienta VUV5000 helium plasma discharge lamp and a toroidal grating monochromator, with the combined spectral bandwidth on the order of ~ 0.1 meV. The major advantage of a He plasma lamp is its low cost and size, compared to the synchrotron-based light sources, but the main drawbacks are the finite number of accessible photon energies, defined by He atomic transitions, and relatively low photon count rates at most of these energies. The two atomic transition lines used for measurements are He-Iα line at 21.2 eV and the He-IIα line at 40.8 eV. The light generated by He plasma is directed via a series of differentially pumped stages and a glass capillary to the sample in the main chamber.

2.3.3 Electron analyzer

The spectrometer used for measurements presented in this thesis is a VG Scienta R4000 hemispherical electron analyzer. Figure 2.12 shows a schematic drawing of hemispherical

	Slit Width (mm)	
E_p (eV)	0.5	0.8
5	7.63	10.92
10	–	16
20	–	40

Table 2.1: Measured instrumental energy resolution ΔE (meV) for various analyzer parameters.

analyzer. Incident electrons are retarded by an electrostatic lens to a fixed "pass energy". Then electrons enter a region between the two hemispheres held at a constant voltage difference. The trajectory of electrons between the hemispheres depends on their kinetic energy and initial emission angle. Finally, the electrons hit the detector, consisting of a multichannel plate (MCP), phosphor screen and a CCD camera. The energy resolution of the analyzer is determined by the kinetic energy of the electrons traveling between hemispheres, the radius of the hemispheres, and the size of the entrance aperture (slit) [30]. The tunable parameters are the pass energy E_p and the entrance slit size. Table 2.1 shows the estimated energy resolution at the settings used during the measurements presented in this thesis.

CHAPTER 3

Physics of Perovskite Ruthenates

Ruthenates are not typically considered a part of the strongly-correlated oxide family, in which the repulsion between the electrons on the same lattice site in conjunction with a small bandwidth underlie a plethora of exotic phases, such high-temperature superconductivity, colossal magnetoresistance, etc. In fact, up until the 1994, ruthenates were mainly intersting as high quality substrates and buffer layers for magnetic and ferroelectric oxide devices. Remarkably, the efforts to improve substrate quality made the crystals effectively defect-free and allowed to reveal the fascinating physics of ruthenates, e.g. novel spin-triplet superconductivity and electron nematic phases, both very fragile and sensitive to disorder.

First perovskite ruthenates were synthesized and characterized more than five decades ago by J. J. Randall and R. Ward who found that ternary compounds $SrRuO_3$ and $CaRuO_3$ formed pseudocubic perovskite phases, whereas $BaRuO_3$ crystallized in a hexagonal form [41]. The ferromagnetic ground state was found in $SrRuO_3$ shortly afterwards [42–45], and it attracted considerable attention thanks to its surprising properties. It was the only ferromagnetc among compounds with 4d transition metal and, unlike other ferromagnetic *d*-shell metals, characterized by strong local magnetic moments, $SrRuO_3$ exhibited signatures of collective-electron, or itinerant, magnetism. In addition, while $SrRuO_3$ is ferromagnetic below $T_{FM} = 160$ K, $CaRuO_3$ was found to be s a paramagnet, despite their very similar structure and the same number of 4d electrons; and $SrFeO_3$, also with the same number of outer *d* electrons is antiferromagnetic below $T_N \approx 130$ K.

The discovery of high-temperature superconductivity (HTSC) in the cuprate $La_{2-x}Ba_xCuO_4$ [46] in 1986 led to a surge of research activity in oxides, predominantly in hopes of finding non-cuprate oxide-based superconductors. Another major factor was the emerging field of all-oxide electronics and demand for suitable substrates for the functional oxides. C. B. Eom et al. [47] showed that $Sr_xCa_{1-x}RuO_3$ was very attractive as a conductive layer used in junctions with other oxides, notably superconductors and ferroelectrics. These metallic oxides could be used in epitaxial device structure as opposed to amorphous layers of Al or Pt used for ferroelectric devices before that. $Sr_xCa_{1-x}RuO_3$ has almost isotropic conductivity, films can be grown with high crystal quality and smooth surfaces [47], and magnetic properties and the lattice parameter could be tuned (3.83 to 3.93 Å) by varying Sr to Ca ratio, which provided the lattice matching and allowed to grow epitaxial multilayers with many oxide materials. The ruthenate films themselves could be grown on a variety of substrates ($SrTiO_3$, $LaAlO_3$, $NdGaO_3$, MgO).

A methodical improvement of sample quality followed and eventually resulted in a major breakthrough: in 1994 Y. Maeno and coworkers discovered superconductivity in Sr_2RuO_4 [48] by measuring samples down to dilution refrigerator temperatures. Sr_2RuO_4 has the same crystal structure as the prototypical cuprate parent compound La_2CuO_4. In both Sr_2RuO_4 and the cuprates the electron transport is confined to the planar MO_2 networks, where metal M=Ru or Cu. Despite this similarity this novel superconductor is different in several important ways. First, Sr_2RuO_4 is itself superconducting in contrast to cuprates, where the undoped parent compound is strongly correlated antiferromagnetic Mott insulator. Second, the T_C is a factor of 20-100 lower than what is typical for cuprates. Last, the proximity of Sr_2RuO_4 to $SrRuO_3$ suggests the presence of ferromagnetic (FM) fluctuations, unlike the strong antiferromagnetic fluctuations considered detrimental to the high temperature superconductivity. This observations suggested a possible new pairing mechanism in Sr_2RuO_4. Based on presence of FM interactions as well as the details of

quasiparticle band structure, known from quantum oscillations [49] and density functional studies [50], T. M. Rice and M. Sigrist proposed a model of superconductivity in Sr_2RuO_4 with unconventional symmetry involving spin-triplet pairing analogous to A-phase of superfluid 3He [51]. The evidence of spin S=1 Cooper pairs was later found by nuclear magnetic resonance (NMR) [52–54] and polarized neutron scattering experiments [55], and the presence of internal magnetic field below T_C was detected by muon spin-relaxation measurements [56] and magneto-optic Kerr effect (MOKE) [57]. That provided strong experimental support to a spin-triplet pairing with broken time reversal symmetry.

The discovery of superconductivity in Sr_2RuO_4 generated an explosion of interest in ruthenate physics. The field turned out to be fruitful with new exotic phases, such as metamagnetism and electronic liquid crystalline states in $Sr_3Ru_2O_7$ [58–60], spin-density waves, orbital-dependent Mott-insulating phase in $Ca_{2-x}Sr_xRuO_4$ [61], ferromagnetism, antiferromagnetism and spin-glasses [62; 63] colossal magnetoresistance in doped $Ca_3Ru_2O_7$ [64]. This fascinating diversity of electronic phases in compounds with only a little structural variety stems from the interplay between the crystal structure, local interactions and the details of quasiparticle dynamics and is a subject of an ongoing research. In the rest of this chapter we will review some details of microscopic physics responsible for the phases and properties of perovskite ruthenates.

3.1 Crystal structure

Perovskite structure commonly occurs in ternary compounds with formula ABO_3, where A is an alkaline earth or a lanthanoid, B is a transition metal and O is Oxygen. The crystal structure is a network of corner-sharing octahedra AO_6, where transition metal ion in the center is six-fold coordinated with oxygen ions in the vertices. The idea of all-oxide electronics is to utilize the common structure of functional oxides with closely matched

in-plane lattice parameters that enables epitaxial growth of multilayer heterostructures with custom-designed properties. The perovskite structure is an end member ($n = \infty$) of Ruddlesden-Popper series with general formula $A_{n+1}B_nO_{3n+1}$, in which n layers of octahedra are separated (disrupted) by rock-salt layer. The structure was first described by Victor Goldschmidt, who found that its stability in ambient conditions depends on the relative ionic radii, more specifically the tolerance factor

$$t = \frac{r_A + r_O}{\sqrt{2}(r_B + r_O)}$$

where r_A, r_B and r_O are, respectively, the radii of A, B and O ions. Let's consider perovskite ruthenates $ARuO_3$ where A=Ca, Sr, Ba. The ideal cubic structure with A-O-A bond angle of 180^o occurs when t is in the range of $0.9 - 1$. For $SrRuO_3$ and $CaRuO_3$ the values of the ratio are respectively $t_{SRO} = 0.85$, falling into the range $0.71 - 0.9$, for which the orthorhombic structure is stabilized as the mismatch between ionic radii is accommodated by cooperative rotation of RuO_6 octahedra. The reduction of Ru-O-Ru bond angle directly impacts the kinetic energy of the electrons moving in the crystal and the macroscopic physical properties, as will be discussed later in detail. In $BaRuO_3$, the A-site ion Ba is too large and $t_{BRO} = 1.0625 > 1$ [65]. For $t > 1$ hexagonal polytype 9R is stable at ambient conditions, where layers of corner-sharing and edge-sharing octahedra are interleaved. Recently C.-Q. Jin et al succeeded in synthesizing new phases of $BaRuO_3$ by sintering 9R phase under high pressure: 6H, 4H and cubic perovskite (1000^oC under 18 GPa pressure [66]. Higher sintering pressure leads to an increase in the relative number of layers with corner-sharing octahedra, hence the cubic phase requires the highest pressure and is the least stable in ambient conditions.

J. J. Randall and R. Ward showed that they could synthesize different structurally related phases (RP series) by varying Sr to Ru mixing ratio. K_2NiF_4 structure was formed when Sr/Ru=2, cubic perovskite for Sr/Ru=1 and multiple intermediate phases.

3.2 Local physics: crystal field and Hund's coupling

The stable crystal structure and physical properties of a solid are determined by electrons in the valence bands, which in $SrRuO_3$ and Sr_2RuO_4 are the states derived from hybridization of partially occupied Ruthenium-4d and Oxygen-2p orbitals. The A-site ion is electronically inactive, and has no weight near the Fermi level. From simple valence counting, the electronegative Oxygen assumes -2 oxidation state by completing its 2p shell with extra two electrons, Sr/Ca/Ba have +2 charge, which leaves Ru ion in +4 oxidation state in both $SrRuO_3$ and Sr_2RuO_4 with 4 electrons per Ru. The local octahedral crystalline environment around Ru ion formed by the cage of six O ions, splits the Ru-4d orbitals into t_{2g} and e_g manifolds, which can be thought of as eigenstates of the electrostatic ionic potential perturbed by a small crystal field. The Ru-4d e_g orbitals $d_{x^2-y^2}$, $d_{3z^2-r^2}$ have their lobes pointing to the oxygen ions and the antibonding states formed from e_g and O-p σ orbitals are fully unoccupied, lifted about 2 eV higher than antibonding states of Ru4d-t_{2g} (d_{xy}, d_{xz}, d_{yz}) and O-p π orbitals that cross the Fermi level. In the perfect cubic symmetry, the energy levels of three t_{2g} orbitals d_{xy}, d_{xz}, d_{yz} are degenerate. The symmetry is usually lower in the real materials, e.g. tetragonal in $(Sr/Ba)_2RuO_4$ and orthorhombic in $(Sr/Ca)RuO_3$ and Ca_2RuO_4; this splitting, however, is much less than the width of the energy bands. Thus, to a very good approximation the physics is determined by 4 electrons occupying 3 bands with the symmetry of the aforementioned t_{2g} orbitals [50; 67].

For an isolated Ru4+ ion, Hund's rule requires that the states with the largest value of the total spin angular momentum S have the lowest energy. Hund's rule coupling is not strong enough, however, to exceed the crystal field splitting and the low spin state with local moment $S = 1$ is favored. The importance of Hund's rule coupling for the formation of the local moment was confirmed by susceptibility measurements of $Sr_2Ir_{1-x}Ru_xO_4$ alloys, where the dilute Ru acts as a $S = 1$ moment impurity [68]. Further evidence for spin triplet $S = 1$

moments is the ferromagnetic metallic state observed in the perovskite, $SrRuO_3$, that shows a saturated moment of 1.4 μ_B. The role of Hund's rule coupling for the quasiparticle dynamics in the itinerant systems such as ruthenates and iron pnictides/chalcogenides was revealed in a recent series of works and will be discussed later.

3.3 p-wave order parameter in Sr_2RuO_4

In this section we briefly discuss the *p-wave* order parameter describing the symmetry of the pair wavefunction in Sr_2RuO_4. The superconducting order parameter is given as a function of spin and momenta $\Delta_{\sigma\sigma'}(\mathbf{k})$. It can be regarded as a wave fucntion of a pair of electrons $(\mathbf{k}, \sigma)$ and $(-\mathbf{k}, \sigma')$. For spin-triplet state in general the order parameter has three independent components and can be expressed as a 3-vector or a symmetric 2×2 matrix. A convenient notation was introduced by Balian and Werthamer where they use a complex d-vector:

$$\Delta_{\sigma\sigma'}(\mathbf{k}) = i[(\mathbf{d}(\mathbf{k}) \cdot \sigma)\sigma_y]_{\sigma\sigma'}$$

or

$$\begin{pmatrix} \Delta_{\uparrow\uparrow}(\mathbf{k}) & \Delta_{\uparrow\downarrow}(\mathbf{k}) \\ \Delta_{\downarrow\uparrow}(\mathbf{k}) & \Delta_{\downarrow\downarrow}(\mathbf{k}) \end{pmatrix} = \begin{pmatrix} -d_x(\mathbf{k}) + id_y(\mathbf{k}) & d_z(\mathbf{k}) \\ d_z(\mathbf{k}) & d_x(\mathbf{k}) + id_y(\mathbf{k}) \end{pmatrix},$$

where spin is quantized along z-axis. The d-vector is perpendicular to spin and behaves as a vector under spin rotations. Its components d_i define the orbital part of the wave function for spin perpendicular to $\hat{i}$. In review by Mackenzie and Maeno [69] the possible d-vectors are given for p-wave states on a cylindrical Fermi surface for a tetragonal crystal. We will put some constraints on the possible d-vector states for Sr_2RuO_4. The requirement of *unitarity* is given by $\mathbf{d}(\mathbf{k}) \times \mathbf{d} * (\mathbf{k}) = 0$. In unitary states the spins are not polarized, which exludes dependencies like $\hat{\mathbf{x}} \pm i\hat{\mathbf{y}}$. Next, Sr_2RuO_4 can be considered as a 2-dimensional system, excluding k_z-dependence from $\mathbf{d}(\mathbf{k})$. Down to low temperatures, Sr_2RuO_4 maintains a tetragonal structure with the crystal point group symmetry D_{4h}, which limits the possible

spin-triplet states to those for the two-dimensional square lattice with C_{4v} symmetry. The possible states are given in Table 3.1. These vectors only represent symmetries, and the state $\mathbf{d}(\mathbf{k}) \propto \hat{z}(\sin k_x \pm i \sin k_y)$ would be compatible with the last vector in the table. All the listed states are unitary with equal spin pairing. The last row represents states with broken time-reversal symmetry associated with orbital part of the wave function, $L_z = \pm 1$ and, thus, correspond to chiral states.

	d-vector	direction of $\mathbf{d}$	Time-reversal symmetry	Analogy to ^{3}He	Topological?
Γ_1^-	$\hat{x}k_x + \hat{y}k_y$	$\mathbf{d} \parallel ab$		BW state (B phase)	
Γ_2^-	$\hat{x}k_y - \hat{y}k_x$	$\mathbf{d} \parallel ab$			
Γ_3^-	$\hat{x}k_x - \hat{y}k_y$	$\mathbf{d} \parallel ab$			
Γ_4^-	$\hat{x}k_y + \hat{y}k_x$	$\mathbf{d} \parallel ab$			
Γ_5^-	$\hat{z}(k_x \pm ik_y)$	$\mathbf{d} \parallel c$	broken	ABM state (A phase)	Yes

Table 3.1: Possible d-vector states

3.4 Growth considerations

Ba_2RuO_4 synthesized at atmospheric pressure is not isostructural to Sr_2RuO_4, and the growth of polycrystalline samples with K_2NF_4 structure was possible using pressures of 64000 atm. The first epitaxially stabilized films of Ba_2RuO_4 isostructural to Sr_2RuO_4 were grown by pulsed laser deposition on (100) $SrTiO_3$ and were reported in [70]. The growth conditions are close to those found to be optimal for growth of Sr_2RuO_4, i.e. substrate temperature $T_{sub} \approx 1000^o$ C, $P_{O_2} \approx 10^{-5}$ Torr for PLD-grown films [70]. The growth conditions used for MBE growth are also very similar for both materials. Given the same structure, same B-site cation, charge neutrality of layers in both compounds it seems reasonable to assume that the defect formation mechanisms are identical in the two materials. The main growth parameters that have to be optimized in order to get high-quality films are the substrate temperature, oxygen partial pressure and correct dosage of the elements. The T_{sub} and P_{O_2} are not

independent parameters but rather define a pressure-temperature window, as illustrated in Figure 3.1. Sr_2RuO_4 forms at low oxygen pressure and high temperature, whereas $SrRuO_3$

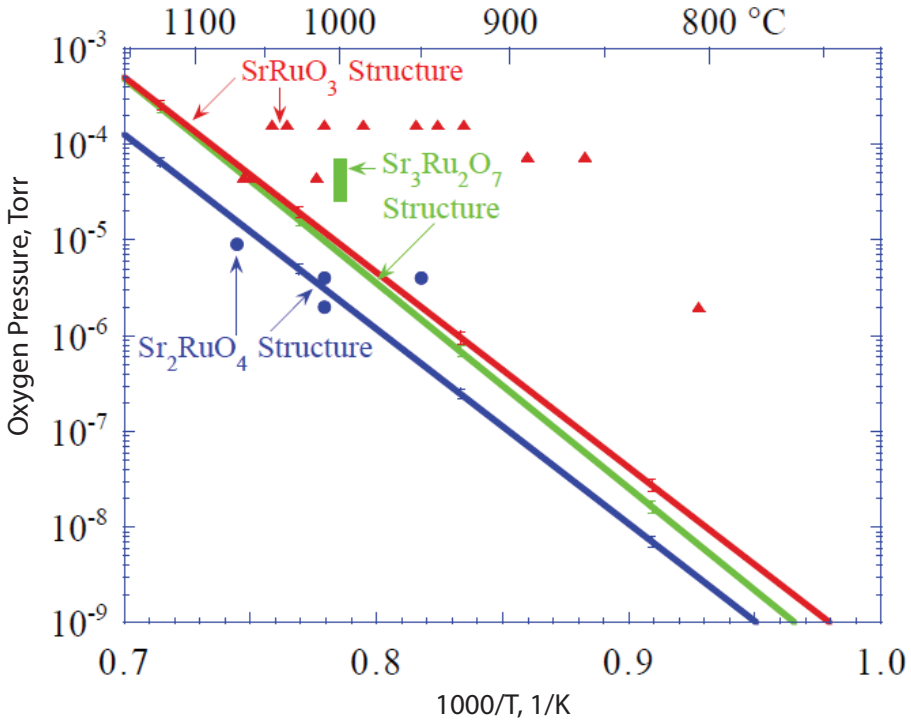

Figure 3.1: Pressure-temperature conditions yielding Sr_2RuO_4, $Sr_3Ru_2O_7$, and $SrRuO_3$ as the major phase for PLD growth on a $LaAlO_3$ (100) substrate [71].

is observed at high oxygen pressure and low temperature. The RP-compounds with intermediate n are observed in a narrow intermediate range between the $n = 1$ and $n = \infty$ regions. Also shown in the Figure 3.1 are the thermodynamic stability lines measured for $n = 1$, $n = 2$ and $n = \infty$ members. On and at higher pressures than each stability line, the corresponding phase is stable. At lower presures than each line, the corresponding oxide is thermodynamically unstable and should decompose. The decomposition reactions are:

$$Sr_2RuO_4 \rightarrow 2\,SrO + Ru + O_2,$$

$$2\,Sr_3Ru_2O_7 \rightarrow 3\,Sr_2RuO_4 + Ru + O_2,$$

$$3\,SrRuO_3 \rightarrow Sr_3Ru_2O_7 + Ru + O_2.$$

The observed trends are in accordance with the principle that the presence of more electropositive species in a compound favors a higher oxidation state of a transition metal. Sr_2RuO_4 has more electropositive strontium than $SrRuO_3$, and thus provides a stable environment for Ru^{4+} to lower oxygen partial pressures. Deviations from the optimal growth conditions as well as incorrect elemental dosage may result in intergrowth faults. These can be arrived at from an ideal phase pure $A_{n+1}B_nO_{3n+1}$ structure by replacing a single AO layer by double-AO layer or vice versa. Various computer simulations and TEM image analysis of the intergrowth faults were performed for $Sr_{n+1}Ti_nO_{3n+1}$ series and have revealed their nature [72]. The enthalpy of the following reactions to form $Sr_{n+1}Ti_nO_{3n+1}$ Ruddlesden-Popper phases from SrO and $SrTiO_3$ was calculated:

$$SrO + nSrTiO_3 \rightarrow Sr_{n+1}Ti_nO_{3n+1}.$$

The enthalpy for the formation of $n = 1$ phase was calculated to be $\Delta H = -11$kJ/mol and $\Delta H = -13$kJ/mol for the formation of the higher phases with $2 \leq n \leq 12$. This means that for high n there is no preference to form n'th member over the mixture of $n - k$ and $n + k$. The relevant quantity for synthesis is the Gibbs free energy of reaction $\Delta G = \Delta H - T\Delta S$, rather than ΔH. The random mixture of $Sr_{n+1}Ti_nO_{3n+1}$ phases has higher configurational entropy than a phase-pure sample and is thus favorable. Thus there is no sufficient driving force (ΔG) to form a phase-pure sample for bulk-growth methods relying on thermodynamics of phase formation. The layer-by-layer growth by reactive molecular beam epitaxy, on the other hand, allows step-by-step control of the deposited layers. High-quality single-phase films of $Sr_{n+1}Ru_nO_{3n+1}$ and $Sr_{n+1}Ti_nO_{3n+1}$ [73] with $n = 1..5$ of were reported to be grown by reactive MBE.

The defects discussed in this section are those that form at the interface between the substrate and the film and propagate through the entire film thickness. They are non-thermodynamic in the sence that their density expected from the energetics of formation

is less than one per crystal, as opposed to, for example, oxygen vacancies or n-phase intergrowths. An example of such crystallographic defects in Sr_2RuO_4 thin films is out-of-phase boundary. This is a translation boundary consisting of a fractional misalignment in the c-axis direction between two neighboring regions of the same crystal. Because any interruption of the structure can act as a pair-breaker, a linear density of OPBs on the order of $1/\xi_{ab}$ results in a non-superconducting film [74], where superconducting coherence length is $\xi_{ab} \approx 66$ nm. Schematically OPBs are shown in Figure 3.2.

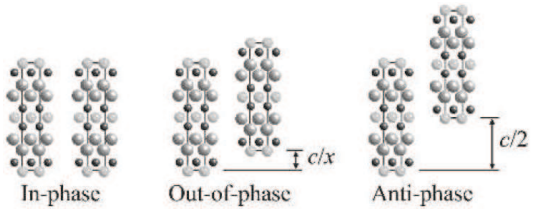

Figure 3.2: Two regions of a crystal that are out of registry by a fraction of the unit cell [75].

A translation boundary defect can result from a shift between regions of a crystal that is out of the plane of a substrate used for film growth or in the plane of the substrate. OPBs also exist in the bulk but are much more likely to occur in epitaxial films due to high crystalline anisotropy, a unidirectional growth front, and the limited structural rearrangement at typical film growth temperatures. At the typical epitaxial film growth temperatures the surface diffusion is much higher than the bulk diffusion, and OPBs that nucleate during the growth of the first layer of the film propagate through the entire film thickness.

OPBs in (001) films of A_2BO_4 are inclined typically at an angle of 73^o to (001). OPBs propagate through the film thickness, except when annihilated by another OPB of the opposite sign in the growing film. TEM images of Sr_2RuO_4 films grown by various methods show this morphology, including the superconducting films from Y. Krokenberger et.al. [76]. These films were grown by PLD on LSAT substrates. The apparent difference of the superconducting films is that they contain regions free of OPB defects larger than $\xi_{ab} = 66$ nm.

CHAPTER 4

Growth and characterization of $(Sr/Ba)_2RuO_4$ thin flims

4.1 Growth of thin films by Molecular-beam epitaxy

Thin films of Sr_2RuO_4 and Ba_2RuO_4 were grown by epitaxial stabilization on a series of substrates with varying lattice parameter by reactive-oxide molecular-beam epitaxy (MBE) in a Veeco GEN-10 system equipped with reflection high-energy electron diffraction (RHEED), and utilizing O_2 + approximately 10% O_3 as an oxidant. All Sr_2RuO_4 and Ba_2RuO_4 studied in

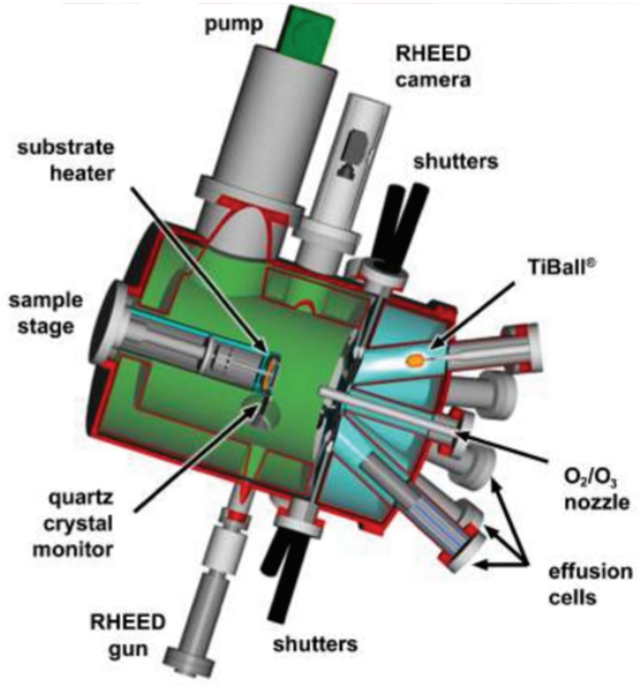

Figure 4.1: Schematic diagram of the growth chamber of molecular-beam epitaxy system. Reprinted from [77].

this work were grown by Carolina Adamo, a postdoc in Prof. Darrell Schlom's MBE laboratory. The in-plane lattice parameter of the films (here, equivalent to Ru-O-Ru bond distance) was varied between 3.87 Å to 3.97 Å ($\Delta a/a$ = 2.6%) through the selection of appropriate substrates (Figure 4.2). Films of Sr_2RuO_4 grown on (001) $SrTiO_3$ (STO, with a lattice constant of a = 3.905 Å) and (100) $Sr_{1.04}Al_{0.12}Ga_{0.35}Ta_{0.50}O_3$ (SAGT with a_p = 3.929 Å, where p denotes the pseudocubic lattice constant) are in tensile strain relative to bulk Sr_2RuO_4 with in-plane lattice parameter of 3.8694 Å[78]. Thin films of Ba_2RuO_4 were synthesized on (001) $SrTiO_3$, (110) $TbScO_3$ (TSO, with a_p = 3.9585 Å), and (110) $GdScO_3$ (GSO, a_p = 3.9678 Å) single crystal substrates [79], which induce a compressive strain. The in-plane lattice parameter of 3.99 Å is only reported for polycrystalline Ba_2RuO_4 synthesized at high pressure [80], since single crystals of Ba_2RuO_4 isostructural with Sr_2RuO_4 do not exist. Substrate temperatures 620 – 850 °C and a background oxidant partial pressure of 4×10^{-7} Torr were maintained during growth. All of the thin film samples were grown in an adsorption-controlled growth mode due to the volatility of ruthenium oxides. Bulk single crystals of Sr_2RuO_4 were grown by the floating zone technique.

4.2 Characterization by x-ray diffraction

The phase purity and crystallinity of the films were characterized by X-ray diffraction (XRD). Figure 4.3(a) shows the XRD curves of Sr_2RuO_4 films grown on $NdGaO_3$ and $SrTiO_3$ and Ba_2RuO_4 grown on $TbScO_3$ and $GdScO_3$. The rocking curve scans of the (006) Sr_2RuO_4 peak with the (002) STO substrate peak of the Sr_2RuO_4 / STO sample (Figure 4.3(b)) have full width at half maximum (FWHM) of 35 arcsec and 42 arcsec, respectively, indicating good crystallinity of films over large length scales.

Sr_2RuO_4 films have their lattice constant relaxed to nearly bulk value after first deposited monolayer when grown on substrates with lattice constants larger than 3.91 Å. This

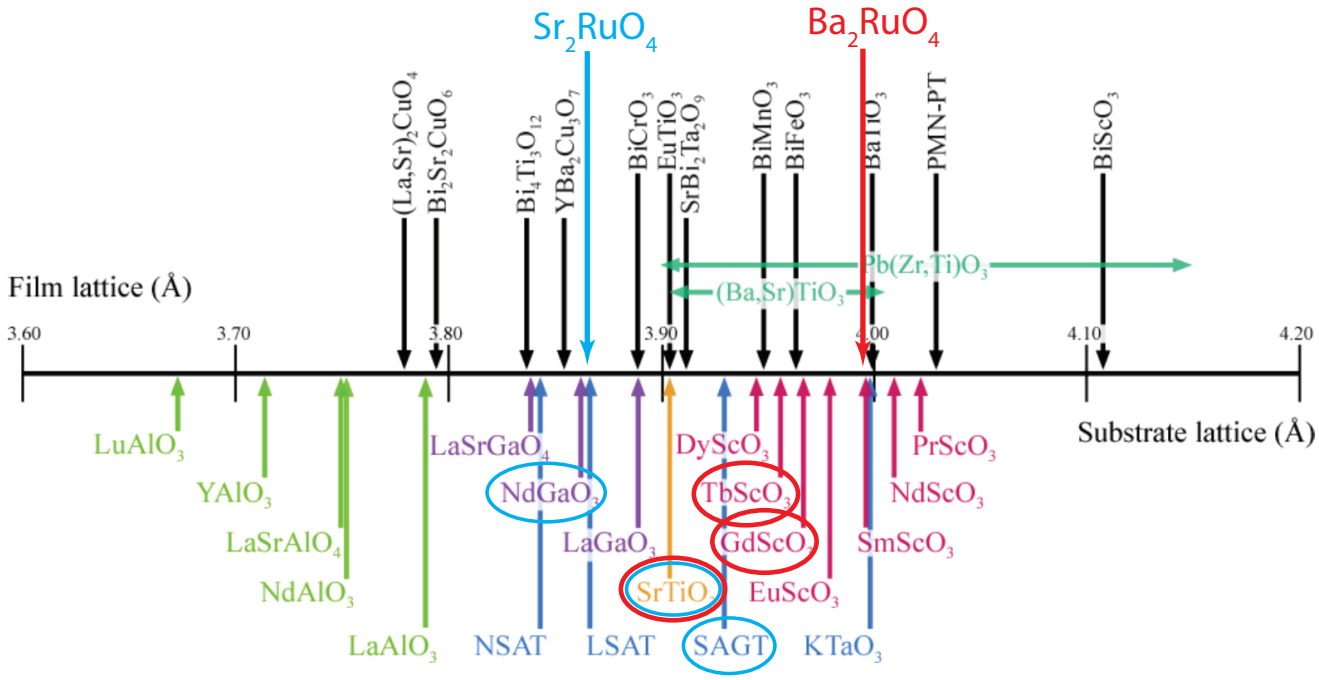

Figure 4.2: Perovskite number line. Substrates circled in blue and red were used for Sr_2RuO_4 and Ba_2RuO_4 growth, respectively.

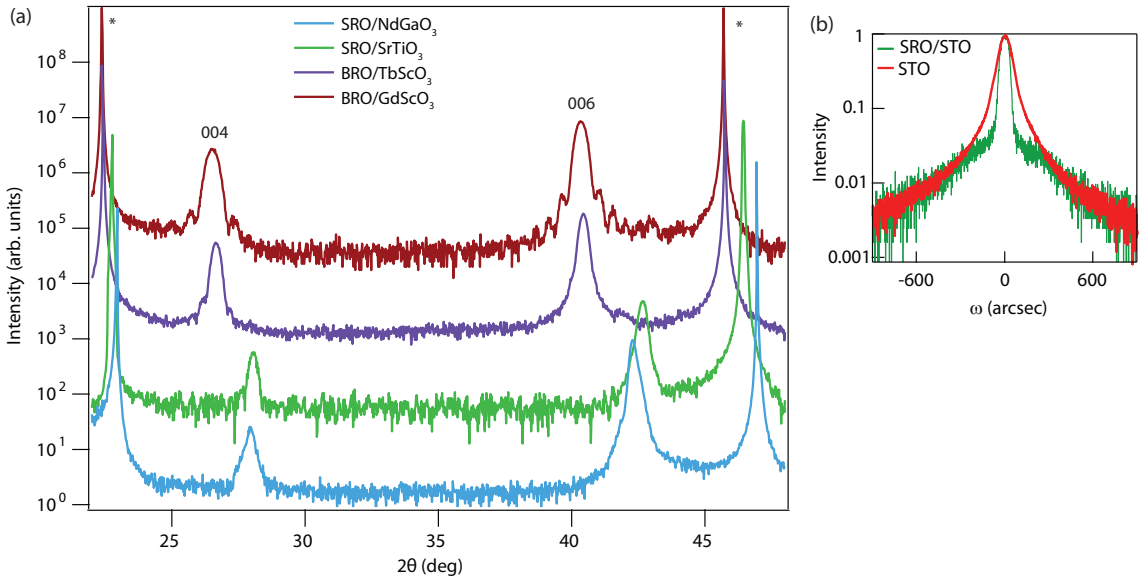

Figure 4.3: (a) X-ray diffraction curves of Sr_2RuO_4 and Ba_2RuO_4 thin films. Diffraction peak indices are indicated for the films; substrate peaks are denoted by the asterisk. (b) Overlay of the rocking curve scans of the (006) Sr_2RuO_4 peak with the (002) STO substrate peak of the Sr_2RuO_4 / STO sample.

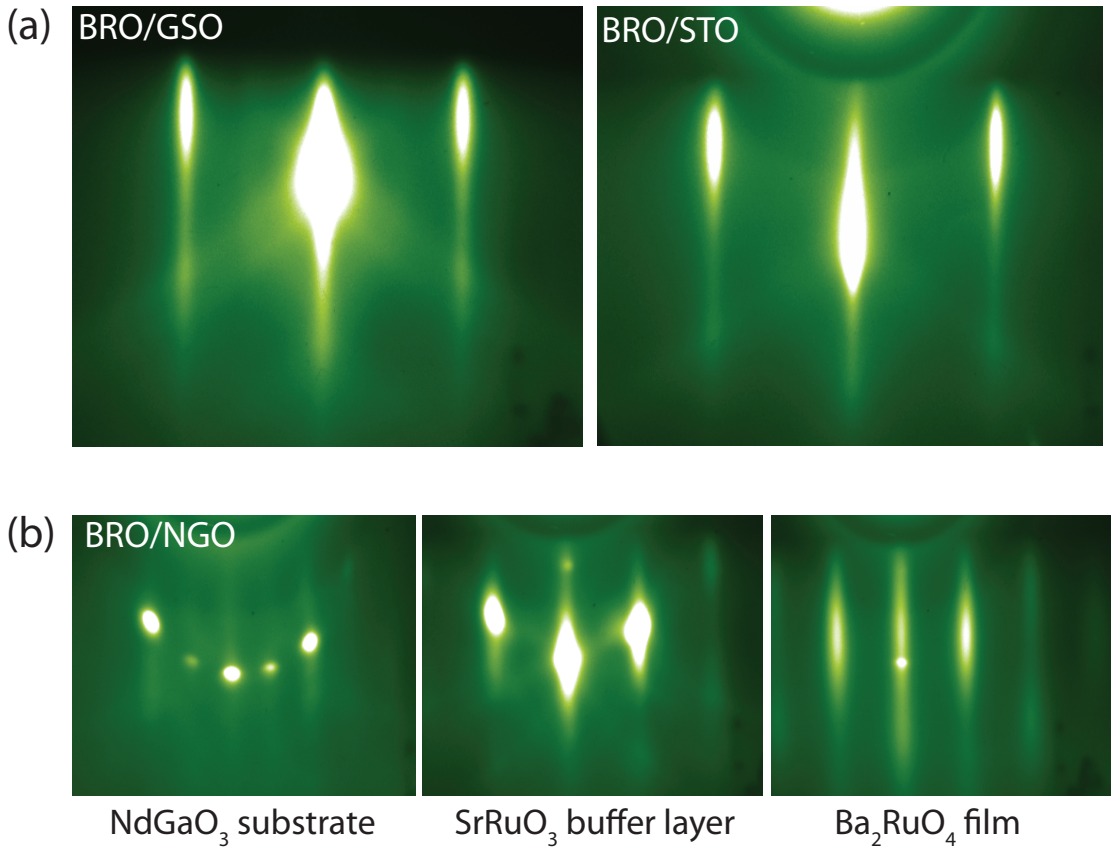

Figure 4.4: (a) Reflection high-energy electron diffraction (RHEED) patterns taken during growth of Ba_2RuO_4 on $GdScO_3$ and Sr_2RuO_4 on $SrTiO_3$ films after growth completion. (b) RHEED pattern snapshots taken for bare substrate (left), after the deposition of $SrRuO_3$ buffer layer (center) and after deposition of Ba_2RuO_4 film (right).

necessitated the substitution of Ba for Sr at the A-site to achieve even larger in-plane lattice constants. In bulk, Ba_2RuO_4 crystallizes in a hexagonal polymorph, and the K_2NiF_4 structure is metastable and has only been synthesized in polycrystalline form above 6 GPa [80]. Epitaxial stabilization has, however, been employed to realize thin films of tetragonal Ba_2RuO_4 [70] which, as we show, are isostructural and isoelectronic to Sr_2RuO_4.

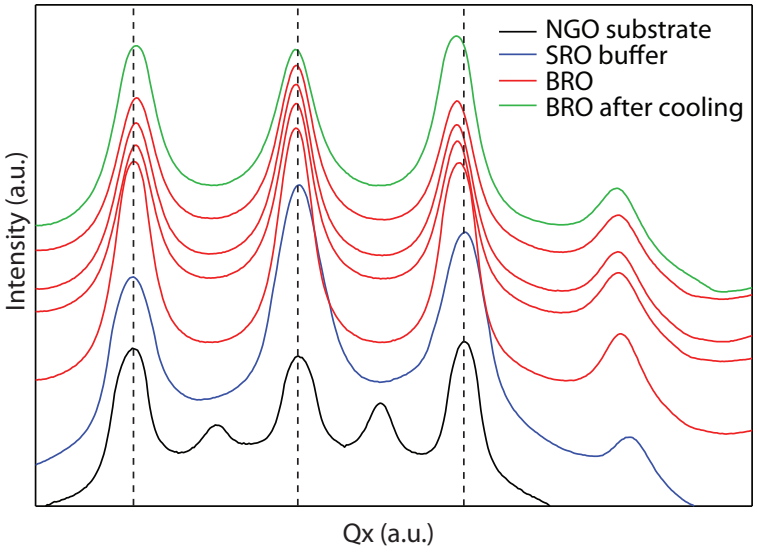

Figure 4.5: RHEED intensity profiles recorded during growth of Ba_2RuO_4 on $NdGaO_3$ substrate with Sr_2RuO_4 buffer layer, corresponding to snapshots in figure 4.4(b). Curves are shifted vertically for clarity. Horizontal axis has reciprocal space dimension, and the lengths are inversely proportional to the in-plane lattice parameter of the last deposited atomic layer. Vertical dashed lines indicate peak positions for the substrate. Atomic layers in Ba_2RuO_4 film (red and green lines) clearly have a larger in-plane lattice parameter.

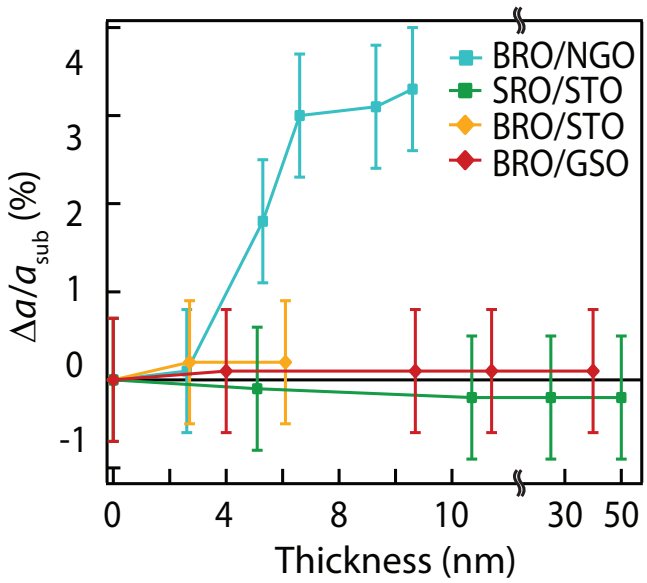

Figure 4.6: Quantitative estimation of the in-plane lattice parameter changes during the growth process.

4.3 RHEED

Figure 4.4 shows reflection high-energy electron diffraction (RHEED) images taken along the $[110]_p$ azimuth after growth for Ba_2RuO_4 / GSO (b) and Ba_2RuO_4 / STO. The evolution of the in-plane lattice parameter in the atomic layers deposited above the substrate was monitored during the growth process as a function of thickness, by measuring the distance between streaks in a series of RHEED images. Figure 4.5 shows an example of RHEED intensity profiles that were used to measure the distance between the streaks. The Ba_2RuO_4 / GSO, Ba_2RuO_4 / STO and Sr_2RuO_4 / STO films were found to be coherently strained for the grown thickness within the measurement error. In contrast, Ba_2RuO_4 grown on $NdGaO_3$ with a 2 u.c. Sr_2RuO_4 buffer layer begins to relax immediately to the bulk lattice parameter ≈3.99 Å or 3.3% relative to $NdGaO_3$, even though the Sr_2RuO_4 buffer layer is coherently strained (Figure 4.6(a,c)).

Table 4.1 lists the strain states of Sr_2RuO_4 and Ba_2RuO_4 studied in this work. The out-of-plane lattice parameter values were determined from Bragg peak positions in $\theta - 2\theta$ XRD scans, and in-plane lattice constant is the substrate value, since the films are coherently strained. The sample parameters from [80] and [70] are given for comparison.

Film / substrate	a_p (Å) [1]	c (Å)	Thickness (nm)
Sr_2RuO_4 (bulk crystal)	3.869	12.75	–
Sr_2RuO_4 / $NdGaO_3$ [2]	3.86	12.8 ± 0.1	40
Sr_2RuO_4 / $SrTiO_3$	3.905	12.7 ± 0.1	50
Sr_2RuO_4 / SAGT [3]	3.929	12.7 ± 0.1	19
Ba_2RuO_4 / $SrTiO_3$	3.905	13.55 ± 0.15	6
Ba_2RuO_4 / $TbScO_3$	3.958	13.4 ± 0.1	40
Ba_2RuO_4 / $GdScO_3$	3.968	13.4 ± 0.1	40
Ba_2RuO_4 [80]	3.99	13.4	–
Ba_2RuO_4 / $SrTiO_3$ [70]	3.905	13.35 ± 0.01	–

Table 4.1: The measured structural parameters of the samples.

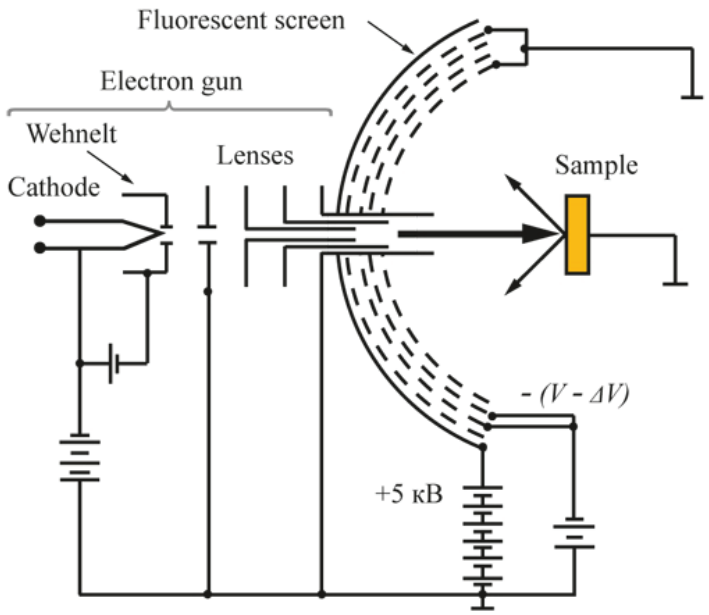

Figure 4.7: Low-energy electron diffraction setup.

4.4 LEED

The high structural quality of the film surface was verified *in situ* with low-energy electron diffraction (LEED). A typical LEED setup schematic is shown in Figure 4.7. In Figure 4.8 we present the LEED images for the Sr_2RuO_4 and Ba_2RuO_4 films taken at 200 eV immediately after the ARPES measurements. The LEED pattern from a cleaved surface of Sr_2RuO_4 single crystal is shown for comprison. We observe sharp diffraction peaks in all samples, and $\sqrt{2} \times \sqrt{2}$ surface reconstruction peaks in all Sr_2RuO_4 samples. The structural reconstruction on cleaved surfaces of Sr_2RuO_4 has been observed in ARPES [82; 83] and originates from freezing of the soft rotational Σ_3 mode of octahedra on the surface. This reconstruction is observed both on the cleaved surface of Sr_2RuO_4 and the pristine Sr_2RuO_4 film surfaces, but is absent in Ba_2RuO_4 samples.

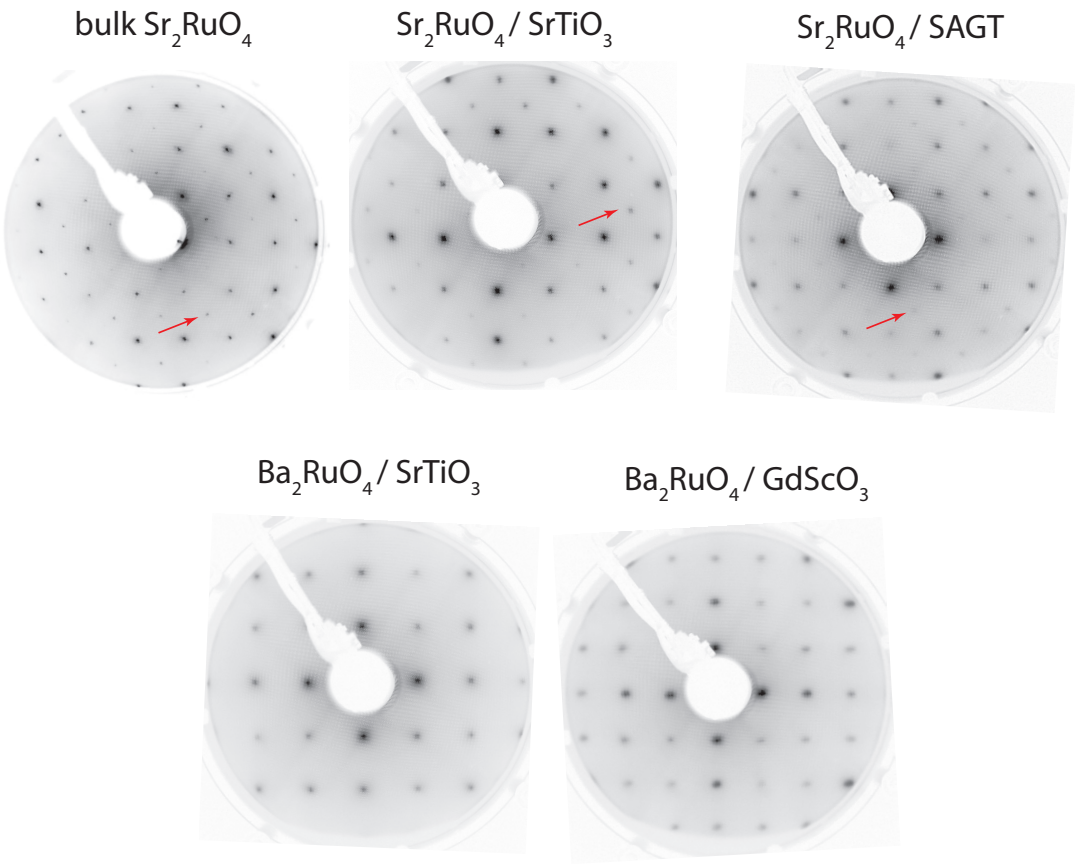

Figure 4.8: Low-energy electron diffraction patterns, recorded at 200 eV for a cleaved single crystal of Sr_2RuO_4 and the same thin films that were measured by ARPES. $\sqrt{2} \times \sqrt{2}$ surface reconstruction spots are indicated by red arrows. The reconstruction is observed on the cleaved surface of Sr_2RuO_4 as well as the pristine Sr_2RuO_4 film surfaces, but is absent for the Ba_2RuO_4 samples.

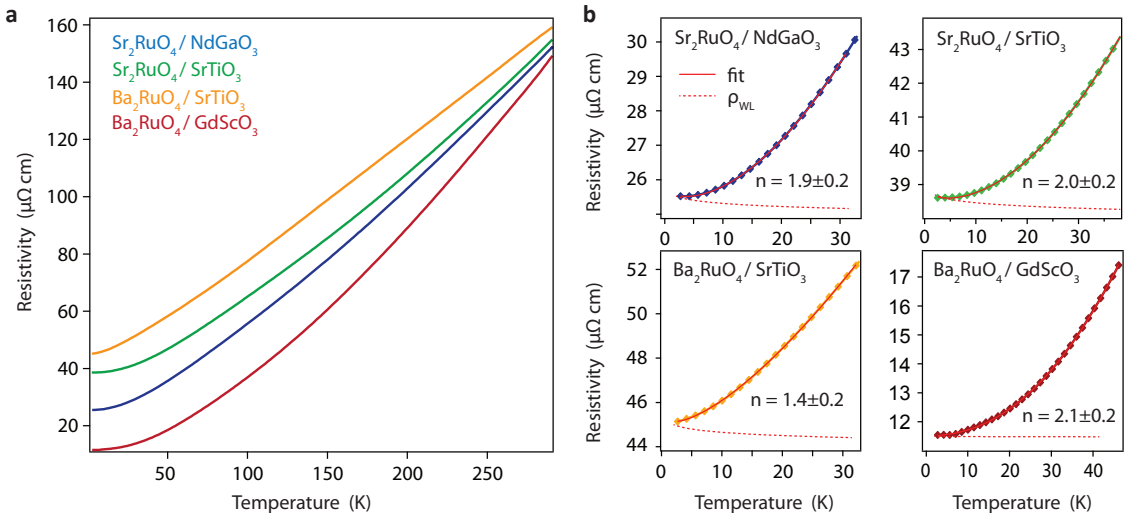

Figure 4.9: (a) Temperature dependence of resistivity for a set of Sr_2RuO_4 and Ba_2RuO_4 films. (b) Low-temperature resistivity fits to a Fermi-liquid (FL) model with weak-localization (WL) scattering in 2D: $\rho(T) = (\rho_{FL}^{-1} + b \ln T/T_0)^{-1}$, where $\rho_{FL} = \rho_0 + AT^n$. The weak-localization contribution $\rho_{WL}^{-1} = \rho_0^{-1} + b \ln T/T_0$ is shown as a red dashed line.

4.5 Electrical transport

The thin films presented here are non-superconducting, with residual resistivities $\rho_0 \approx 10^{-5}$ Ω·cm, although recent upgrades to the growth chamber should allow us to ultimately achieve superconducting films, as has been reported in unstrained thin films grown on LSAT [84]. Temperature dependence of resistivity for a set of Sr_2RuO_4 and Ba_2RuO_4 films is shown on Figure 4.9. Resistivity was measured *ex situ* in van der Pauw geometry [85]. At low temperature we observe an upturn in resistivity characteristic of weak localization (WL) due to impurity scattering. The weak-localization contribution to conductivity in two dimensional system is given by $\sigma_{2D}(T) = \sigma_0 + pe^2/(2\hbar\pi^2) \ln T/T_0$ [86]. We fit the low-temperature resistivity to a generalized Fermi-liquid (FL) model with WL scattering term in two dimensions: $\rho(T) = (\rho_{FL}^{-1} + b \ln T/T_0)^{-1}$, where $\rho_{FL} = \rho_0 + AT^n$. Red dashed line on Figure 4.9 shows the WL contribution $\rho_{WL}^{-1} = \rho_0^{-1} + b \ln T/T_0$.

CHAPTER 5

Manipulation of quasiparticle band structure in $(Sr/Ba)_2RuO_4$ via strain [1]

In this chapter we present the electronic structure of Ba_2RuO_4, measured by angle-resolved photoemission spectroscopy (ARPES), and its relation to the one of its isoelectronic counterpart, the spin-triplet superconductor Sr_2RuO_4. We demonstrate how the Fermi surface topology and quantum many-body interactions can be deliberately tuned via epitaxial strain in Sr_2RuO_4 and Ba_2RuO_4 using oxide molecular beam epitaxy (MBE), *in situ* ARPES, and transport measurements.

5.1 Introduction

Sr_2RuO_4 is the only known candidate for spin-triplet superconductivity among oxide superconductors [87]. It has the same layered structure as high-T_c cuprates, but its superconducting transition temperature of 1.5 K is much lower than that of most cuprates. In most of the unconventional superconductors, which are characterized by anisotropic gap function, the electrons are paired in spin-singlet states. In this way they are similar to conventional *s*-wave superconductors that do not possess spin degrees of freedom. Triplet superconductivity, sometimes called ferromagnetic superconductivity, is unusual in that the Cooper pairs have a non-zero spin magnetic moment, and thus contradict a naive expectation

[1] Much of the data presented in this Chapter has been published in B. Burganov *et al.* Phys. Rev. Lett. **108**, 267003 (2016) and is reproduced here with permission.

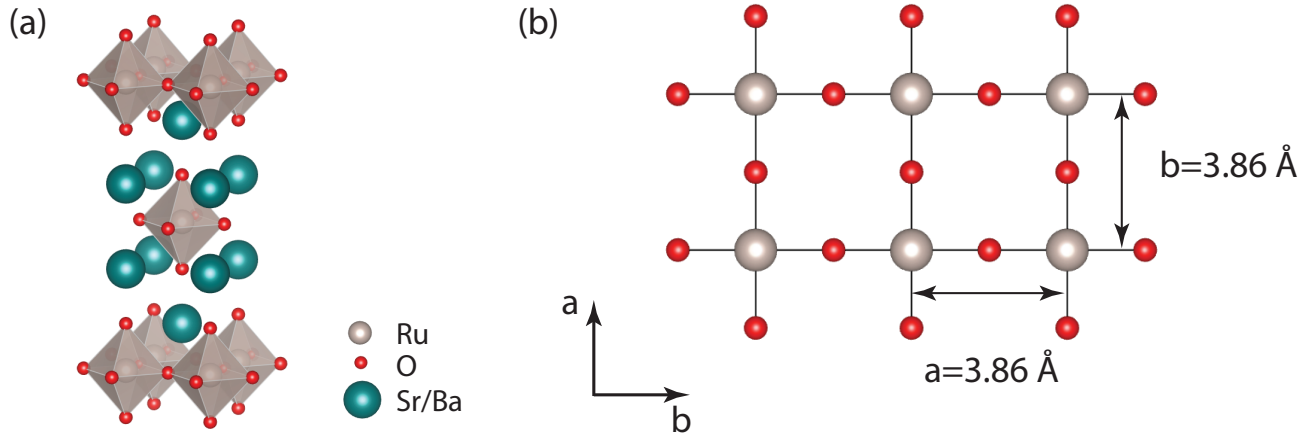

Figure 5.1: (a) Crystal structure of $Sr(Ba)_2RuO_4$. (b) RuO_2 network.

that magnetism and superconductivity are in competition. Most of the known candidates for spin-triplet superconductivity are heavy-fermion systems [88; 89], in which the evidence for spin-triplet state was obtained from nuclear magnetic resonance (NMR) or polarized neutron scattering experiments. In heavy fermion systems, due the strong spin-orbit interactions of heavy elements, spin is not a good quantum number, so the superconducting state is some superposition of singlet and triplet states. The only fully established triplet superfluid state is the one in liquid ^{3}He. Soon after discovery of superconductivity in Sr_2RuO_4 it was theoretically proposed that its ground state is analogous to the A-phase of superfluid ^{3}He [51]. That strongly motivated the experimental efforts to determine the symmetry of unconventional superconductivity in Sr_2RuO_4. A host of studies provided evidence for the triplet state, such as electron spin susceptibility measurements by NMR [52; 90–92], polarized neutron scattering [55]. Evidence of highly anisotropic gap structure was obtained by NMR spin-relaxation rate measurements [93], magnetic field dependent specific heat [94] and phase-sensitive measurements [95; 96]. Experiments reveling broken time-reversal symmetry in the orbital part of the pair wave function were muon spin-resonance [56] and magneto-optic Kerr effect [57; 97]. The possibly chiral nature of the superconducting state

has given rise to proposals utilizing Sr_2RuO_4 as a platform for realizing Majorana fermions, exotic Josephson junctions, and non-Abelian topological quantum computation [98; 99].

The normal state properties of Sr_2RuO_4 have been extensively studied in parallel to the work on superconductivity and are known with high accuracy. Remarkably, the unconventional superconducting state condenses from a conventional low-temperature normal state: Sr_2RuO_4 is a Fermi liquid between $T_c = 1.5$ K and $T_{FL} \approx 25$ K with very low value of residual resistivity of less than 1 $\mu\Omega$ cm. This is very different from, for example, cuprates, in which a number of phases exist above T_c at different carrier concentration levels, e.g. pseudogap, charge- and spin-density wave, non-Fermi liquid, etc. Electron transport in Sr_2RuO_4 is highly anisotropic and predominantly confined within the RuO_2 planes separated by rock salt layers (Figure 5.1). The low-temperature resistivity anisotropy given by the ratio ρ_{ab}/ρ_c is on the order of 10^3 [69; 125]. Sr_2RuO_4 is not expected to have large correlation, as the large overlap of Ru-4d orbitals contributes to both larger bandwidth and smaller on-site Coloumb repulsion, compared to the transition metal oxides from the 3rd row that are traditionally considered strongly correlated. Nevertheless, the quasiparticle mass enhancement is in the range 3-6 for different bands [69; 100], characteristic of moderate correlations. Specific heat measurements reveal large quasiparticle mass, and high electron contribution to specific heat $C_p = \gamma_{el}T + \beta_{ph}T^3$ with Sommerfeld coefficient $\gamma_{el} = 38 \pm 2$ mJ/mol K^2 [101], comparable to some heavy fermion systems [102], and much higher than transition metals. Resistivity at low temperature follows Fermi liquid power law: $\rho = \rho_0 + AT^2$, where electron scattering contribution $A \approx 6$nΩcm/K^2 in-plane and ≈ 5.5 $\mu\Omega$cm/K^2 out-of-plane [103].

Here we demonstrate epitaxial strain engineering as a disorder-free means to dramatically manipulate the electronic structure of Sr_2RuO_4 and its sister compound, Ba_2RuO_4, through a combination of reactive oxide molecular beam epitaxy (MBE) growth and *in situ* ARPES. We are able to observe a topological transition in the γ Fermi surface (FS) sheet (i.e., a Lifshitz

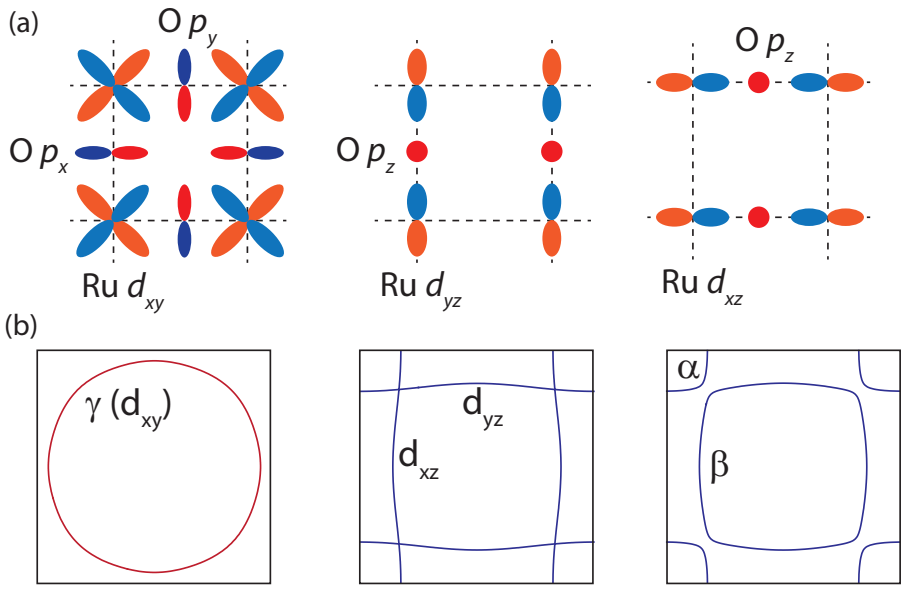

Figure 5.2: (a) Anti-bonding states in $Sr(Ba)_2RuO_4$. (b) Three Fermi surface sheets α, β and γ resulting from hybridization of Ru4d – t_{2g} and O 2p orbitals.

transition) through the selection of appropriate substrates. In addition, we observe signatures of quantum criticality in both ARPES and electrical transport near the Lifshitz transition, as well as a surprisingly large enhancement of the quantum many-body interactions with increasing in-plane lattice constant.

5.2 Electronic structure $Sr(Ba)_2RuO_4$

The low-energy electronic structure of bulk Sr_2RuO_4 is comprised of four electrons occupying Ru 4d-t_{2g} orbitals hybridized with O 2p orbitals in anti-bonding states (Figure 5.2 (a)). The resulting bands cross the Fermi energy and form three sheets of the Fermi surface (Figure 5.2 (b)): the quasi-one dimensional α and β FS sheets (primarily of d_{xz} and d_{yz} character), and the quasi-two-dimensional circular γ sheet (primarily d_{xy} character). The hallmark of Sr_2RuO_4 band structure is a saddle-point van Hove singularity (vHs) in the γ-band located at 14 meV

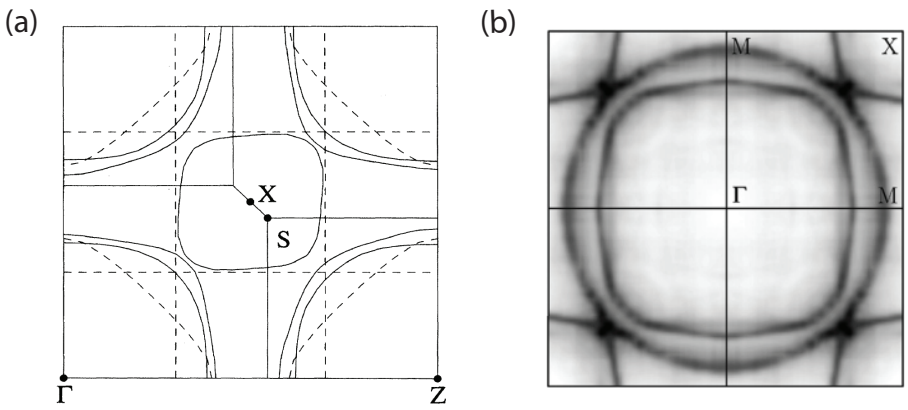

Figure 5.3: (a) Fermi surface of $Sr(Ba)_2RuO_4$. (b) ARPES Fermi surface (reprinted from [104]).

above the Fermi level at the Brillouin zone boundary. It is responsible for the large mass enhancement in the γ-band [105] and has played a defining role in various theories of the superconducting state (see [87] for a review).

The extremely high quality of single crystals have enabled very detailed characterization of Fermi surfaces by ARPES and quantum oscillations, i.e. Shubnikov-de Haas effect [49; 106] and de Haas-van Alphen (dHvA) effect [107–109]. The density-functional theory calculations predict the band structure that agrees with experimental data reasonably well [50; 110; 111] (Figure 5.3(a)). It should be noted, however, that, since the correlation effects are not treated accurately enough in such calculations, the predicted band velocities are 3-4 times higher than experimental, and, due to the correlation-induced inter-band charge transfer, the calculated energy of the vHs point varies, depending on the specific exchange-correlation functional used, and may be very different from the observed one. Due to these correlation effects it is essential to get a direct measurement of the effects of pressure and strain on the quasiparticle band structure. It is also notable that the ground state energies for antiferromagnetic, ferromagnetic and paramagnetic ground states in Sr_2RuO_4 are close, and some early DFT calculations predicted a ferromagnetic ground state [112; 113]. This is not surprising, considering that the closely related $SrRuO_3$ is a ferromagnet with fairly

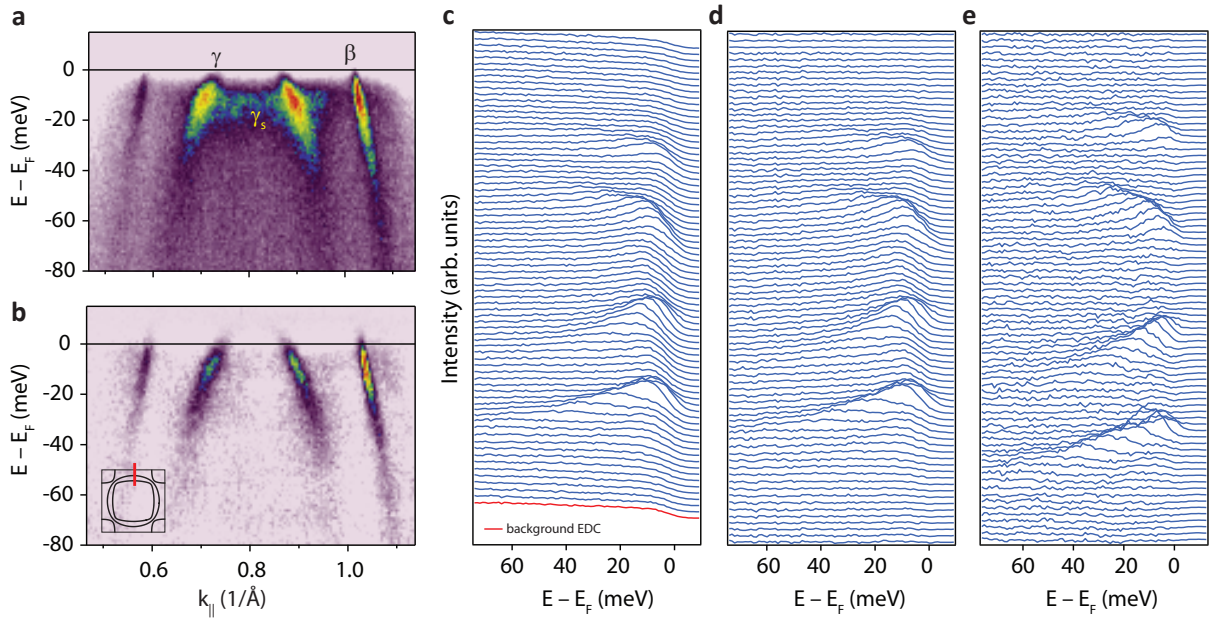

Figure 5.4: (a) Representative raw ARPES spectrum along $(0, k_y)$ from the bulk single crystal Sr_2RuO_4 sample, showing the quasiparticle spectral weight from γ and β bands on a non-dispersive background (red EDC in (c)), and a surface-reconstructed band γ_s. (b) ARPES spectrum after background subtraction. Energy distribution curves (EDC) are shown from the raw ARPES spectrum (c), after non-dispersive background subtraction (d) and after subtraction of the γ_s contribution.

high transition temperature, and $Sr_3Ru_2O_7$ becomes ferromagnetic under pressure along *c*-axis [114; 115], and ferromagnetic order can be stabilized in Sr_2RuO_4 by $< 2\%$ of Co-doping on Ru site; while antiferromagnetic order can be stabilized in Sr_2RuO_4 by small amounts of Ti- or Mn-doping [194; 211]. Given the proximity of various magnetic ground states, this opens up opportunities for studying the strain-induced magnetic orderings and their underlying electronic structure by means of combined MBE-ARPES approach.

5.3 ARPES of Sr_2RuO_4 and Ba_2RuO_4 thin films

The measured ARPES spectra of the Sr_2RuO_4 and Ba_2RuO_4 samples contain the spectral weight from the bulk quasiparticle bands, the surface-reconstructed bands and a non-dispersive background. The non-dispersive background was estimated by averaging energy distribution curves (EDC) at points of Brillouin zone, where no bands near E_F were observed, and subtracted from the measured raw spectra. For example, figure 5.4(a) and 5.4(c) show raw momentum-dependent spectrum and EDC's along $(0, k_y)$ from the bulk single crystal Sr_2RuO_4 sample, containing quasiparticle spectral weight from γ and β bands on a non-dispersive background. The band structure in the surface and subsurface layers is strongly affected by the structural reconstructions on the surface of the Sr_2RuO_4, e.g., there is doubling and folding of all bands [82; 83; 116]. Non-dispersive background was subtracted in figure 5.4(d), and surface band contribution was subtracted in 5.4(e), respectively.

The surface-related spectral features were partially suppressed by cleaving single-crystal Sr_2RuO_4 in the load lock at elevated pressure of 5×10^{-9} torr. Ba_2RuO_4 is found to be free from such reconstructions.

The ARPES spectra measured near the valence band of Sr_2RuO_4 and Ba_2RuO_4 thin films are presented in Figure 5.5. The spectral features in the $2-6$ eV range, corresponding to O-2p levels are similar in both compounds as expected. The bands near the E_F from Ru-4d are much weaker due to lower photoemission cross section of these smaller orbitals, and will be discussed below. Non-dispersing core levels from Sr and Ba atoms are clearly observed at higher binding energy.

In Figure 5.6, we show a series of ARPES FS maps as a function of increasing in-plane lattice constant on a bulk single crystal of Sr_2RuO_4 cleaved at elevated temperature (a = 3.869 Å), Sr_2RuO_4 grown on $SrTiO_3$ (STO; a = 3.905 Å), Ba_2RuO_4 grown on $SrTiO_3$ (a = 3.905 Å), and Ba_2RuO_4 grown on $GdScO_3$ (GSO; a = 3.968 Å). The data from the single crystal

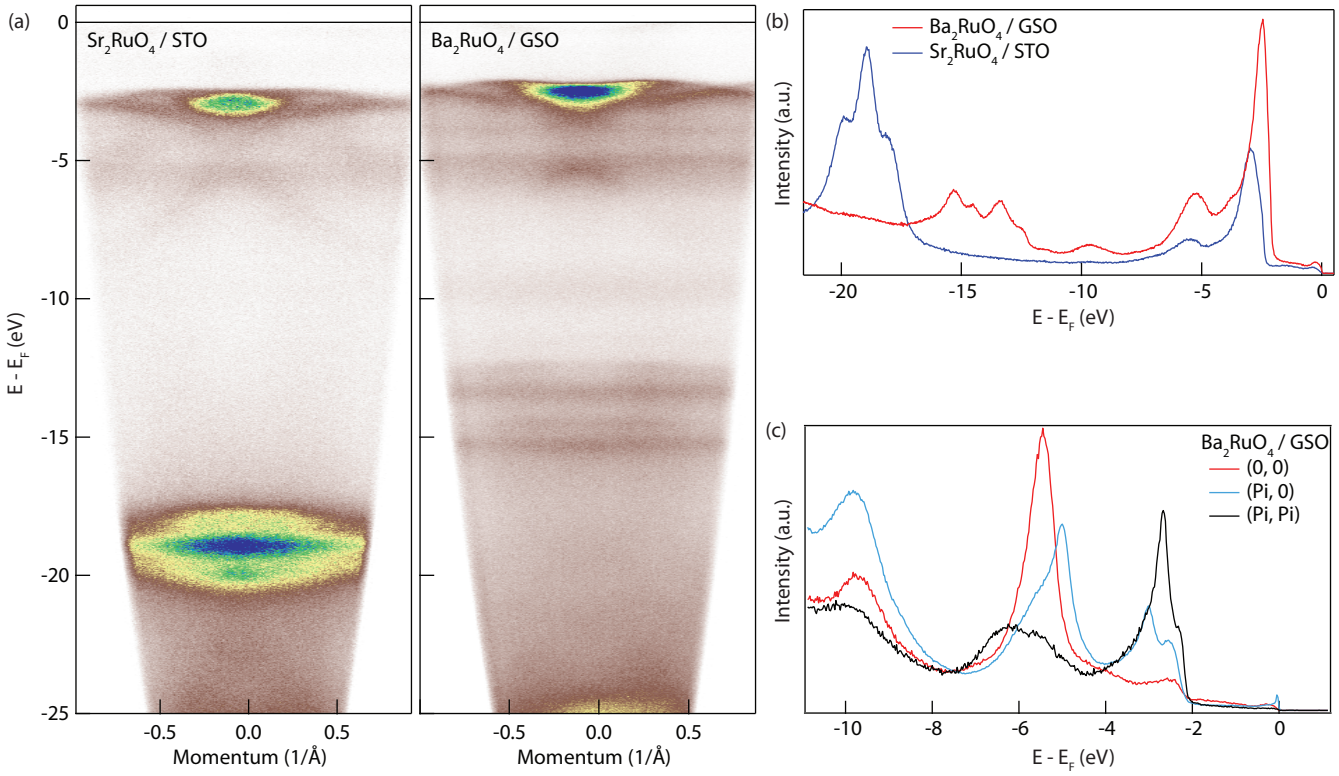

Figure 5.5: (a) Valence band spectra of Ba_2RuO_4 and Sr_2RuO_4 films. (b) Line cuts measured with photon energy $E_{ph} = 40.8$ eV at $k = (0, 0)$. (c) Line cuts at high symmetry points measured with $E_{ph} = 21.2$ eV.

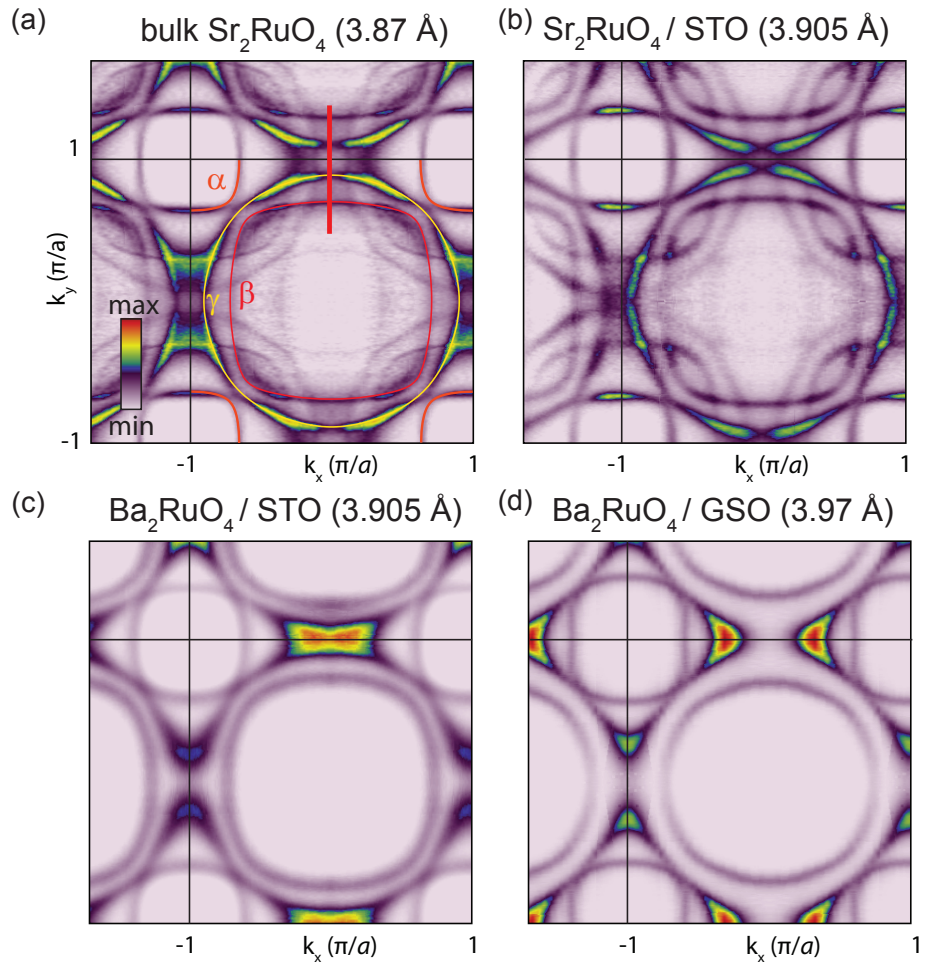

Figure 5.6: Fermi surface maps for select strain states of Sr_2RuO_4 and Ba_2RuO_4.

of Sr_2RuO_4 (Fig. 5.6(a)) shows all three bulk FS sheets, as well as a $\sqrt{2} \times \sqrt{2}$ surface reconstruction, which generates additional sets of folded surface-derived bands[82; 117]. The $\sqrt{2} \times \sqrt{2}$ surface reconstruction is still apparent in Figure 5.6(b), indicating that the reconstruction is also present on the natively grown surface. One of the unique hallmarks of Sr_2RuO_4 is the presence of a saddle point at $(\pi, 0)$ and $(0, \pi)$, which gives rise to a van Hove singularity (vHs) only 14 meV above the Fermi energy (E_F, Figure 5.7(a)). When this vHs passes through E_F, the γ sheet undergoes a topological transition from electron-like to hole-like. For the thin film of Sr_2RuO_4 / STO (Figure 5.6(b)), the γ FS sheet is noticeably enlarged versus bulk and the vHs is pushed down to 9 meV above E_F (Figure 5.7(b)). The

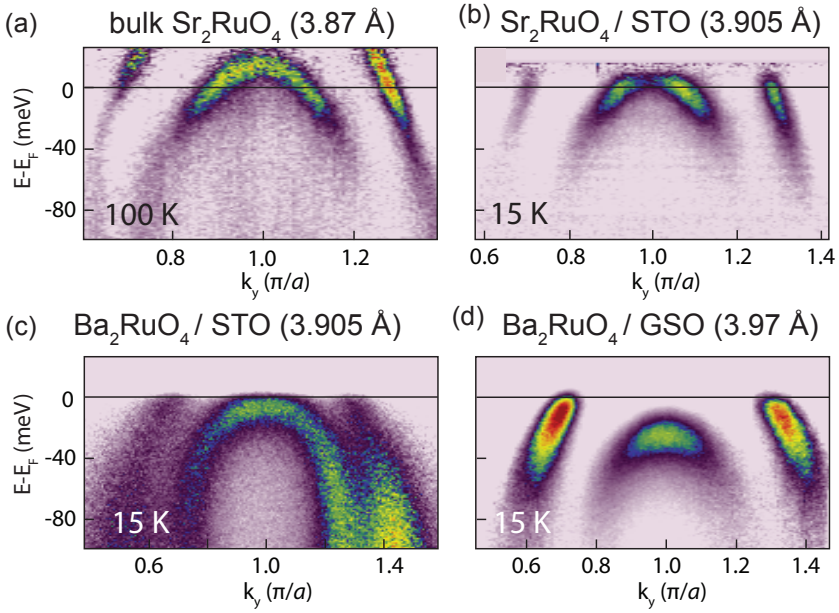

Figure 5.7: Spectral weight along the $(0, k_y)$ direction (thick red line in 5.6(a)) for Sr_2RuO_4 and Ba_2RuO_4 films.

data in panel (a) was measured at an elevated temperature (T = 100 K) to thermally populate the states above the Fermi level; the rest of the data in this chapter was taken at 15 K. Additionally, to show the dispersion near the vHs above E_F, the spectral weight was divided by the Fermi function in 5.7(a) and (b).

For Ba_2RuO_4 on $SrTiO_3$ (Fig. 5.6(c)), the γ FS is almost precisely at the topological transition between electron and hole-like, and the vHs is nearly at E_F (4 meV below, Fig. 5.7(c)). Although the samples shown in Fig. 5.6(b) and (c) are both grown on $SrTiO_3$, Ba_2RuO_4 / $SrTiO_3$ is much closer to the topological transition primarily due to the reduced second nearest neighbor hopping (t_4/t_1) which changes the shape of the γ FS and lowers the vHs. For Ba_2RuO_4 grown on $GdScO_3$, the vHs is now well below E_F (25 meV below, Fig. 5.7(d)), and the γ FS clearly forms a hole-like sheet centered around (π, π). The surface reconstruction is absent in Ba_2RuO_4 films, likely due to the larger Ba cation radius (Ba^{2+} : 1.47 Å vs. Sr^{2+} : 1.31 Å [118]) which should impede the freezing of the Σ_3 phonon mode on the

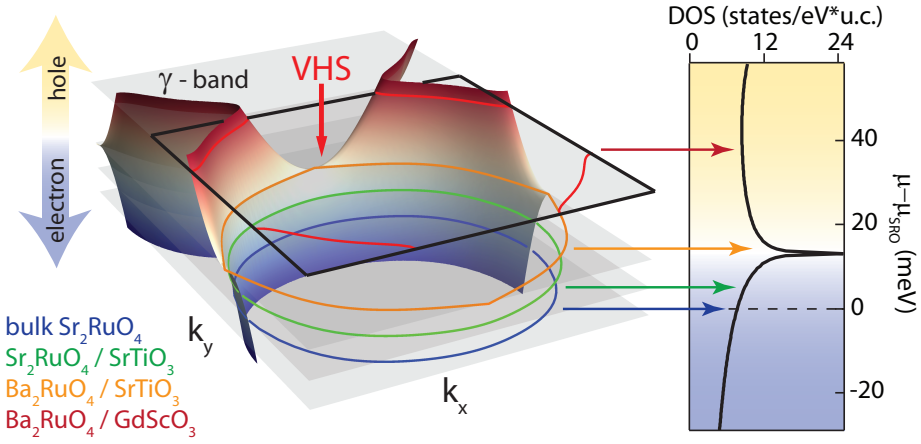

Figure 5.8: Schematic showing the evolution of the γ Fermi surface and density of states at E_F as a result of strain and negative chemical pressure by A-site substitution.

surface. It is also notable that the β FS sheet becomes noticeably less 1D, due to the increased transverse hopping between $d_{xz/yz}$ orbitals (t_3/t_2).

5.4 Lifshitz transition in the γ-band

A schematic of the strain evolution of the γ FS is shown in Fig. 5.8, where the vertical axis is the effective change in the chemical potential of the γ-band relative to bulk Sr_2RuO_4. The change in FS topology cannot be described simply as a rigid shift of the bulk bands; the Fermi surfaces and density of states shown in Fig. 5.8 are generated from a generalized tight binding model whose parameters are varied to fit the different strained samples. The filling of the γ band arises from inter-orbital electron transfer from the d_{xz} and d_{yz} orbitals into the d_{xy} orbital; the total number of electrons in all three bands remains constant at 4.00 ± 0.05 (Fig. 5.9(b)). Although density functional calculations indicate that the spin-orbit interaction is non-negligible [119], we could not directly resolve any spin-orbit split bands, possibly due to impurity scattering and/or experimental resolution.

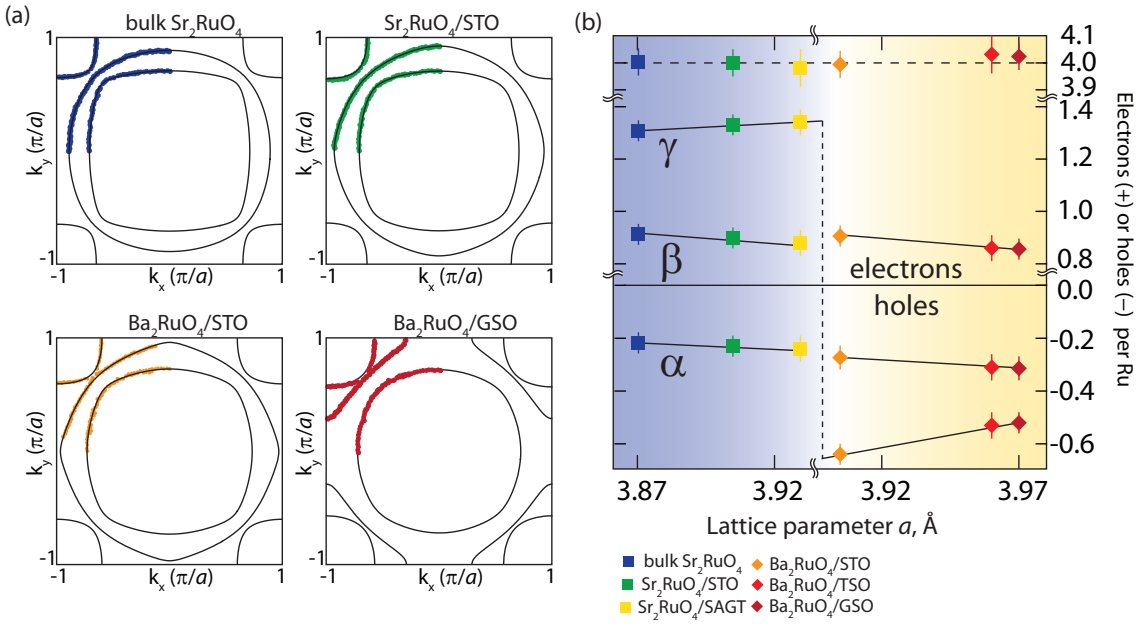

Figure 5.9: (a) Tight-binding parametrization of ARPES Fermi surfaces and LDA Fermi surfaces. (b) Luttinger volume of experimental Fermi pockets as a function of the in-plane lattice parameter. The total number of electrons adds up to n=4.00±0.05 showing negligible overall doping.

Change in the the FS topology of the γ-band manifests in the change of the carrier sign, as can be observed from the Hall effect measurements (Figure 5.10).The Hall coefficient R_H at T = 15 K in $Ba_2RuO_4/GdScO_3$ is nearly equal in magnitude and opposite in sign to the measured in single crystals of Sr_2RuO_4, suggesting the dominating role of the γ-sheet in conductivity.

5.5 Tight-binding parametrization of experimental band structure

To quantitatively characterize the evolution of the quasiparticle dispersion as a function of strain and A-site cation, we parametrized the low energy band structure by fitting a three-band tight-binding model to the ARPES Fermi surfaces and dispersions. As the spin-orbit split bands could not be resolved in the experiment, SO coupling was not included

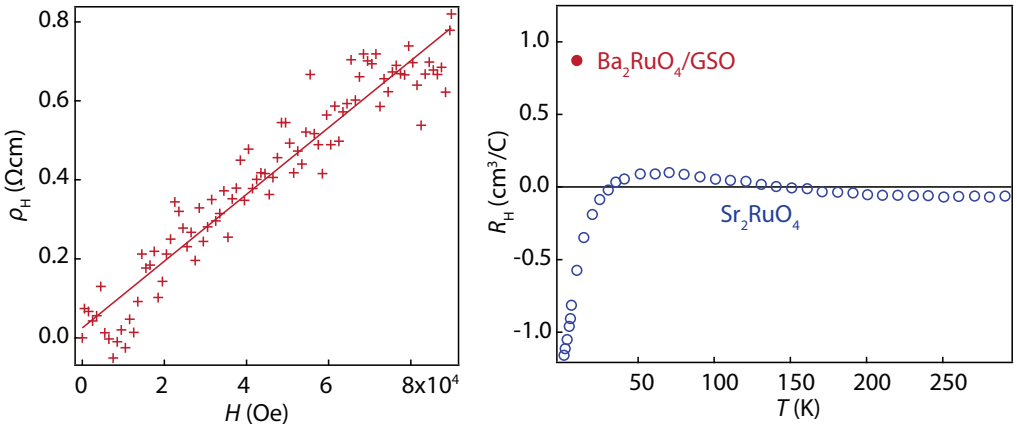

Figure 5.10: Hall effect in sample with hole-like γ-FS sheet. The temperature-dependence of R_H for single-crystal Sr_2RuO_4 from [120] is shown for comparison.

in the model. The energy bands are found as the eigenvalues of the Hamiltonian matrix:

$$H = \begin{pmatrix} \epsilon_{xy} & 0 & 0 \\ 0 & \epsilon_{xz} & V \\ 0 & V & \epsilon_{yz} \end{pmatrix}$$

where $\epsilon_{xy} = -\mu_1 - 2t_1(\cos(k_x a) + \cos(k_y a)) - 4t_4 \cos(k_x a)\cos(k_y a)$, $\epsilon_{xz/yz} = -\mu_2 - 2t_2 \cos(k_{x/y} a) - 2t_3 \cos(k_{y/x} a)$, and $V = 4t_5 \sin(k_x a)\sin(k_y a)$. The fitting procedure is carried out in two steps. First, the dimensionless parameters t_4/t_1, t_3/t_2, t_5/t_2, μ_1/t_1, μ_2/t_2 are computed by fitting the model to the Fermi momenta extracted from APRES FS maps. Then, t_2 was determined from fitting the α and β band dispersions along the high symmetry directions of the Brillouin zone; t_1 was found from fitting the energy-momentum points $(\epsilon_{\mathbf{k}}, \mathbf{k})$ for the γ band in the energy range 0 – 30 meV in the full Brillouin zone. The fitted parameters are given in Table 5.1. The FS parametrization of the single crystal Sr_2RuO_4 agrees well with the reported previously in the literature [121].

	lat. const	t_1 (eV)	t_2 (eV)	t_3/t_2	t_4/t_1	t_5/t_2	μ_1/t_1	μ_2/t_2
Sr_2RuO_4 (bulk crystal)	3.869 Å	0.119	0.165	0.08	0.41	0.13	1.48	1.08
$Sr_2RuO_4/SrTiO_3$	3.905 Å	0.114	0.140	0.09	0.40	0.16	1.50	1.06
$Ba_2RuO_4/SrTiO_3$	3.905 Å	0.095	0.115	0.19	0.385	0.14	1.54	0.97
$Ba_2RuO_4/GdScO_3$	3.968 Å	0.070	0.085	0.19	0.35	0.16	1.57	0.87

Table 5.1: Tight-binding parameters of the measured band structure.

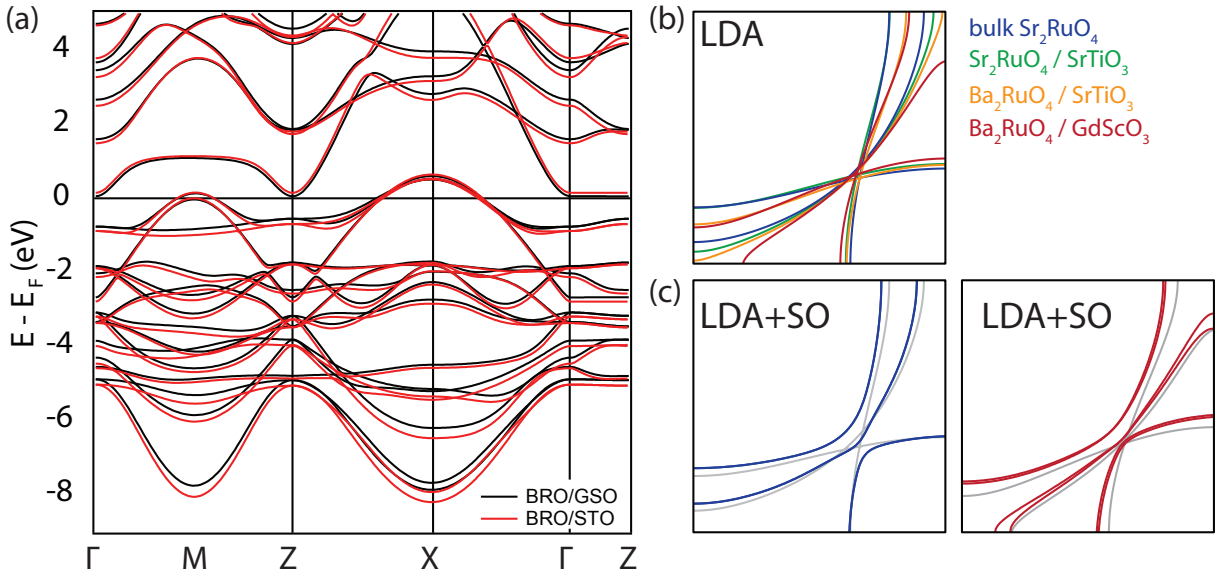

Figure 5.11: (a) LDA band structure near E_F for the Ba_2RuO_4 / GSO and Ba_2RuO_4 / STO showing the effect of strain. Calculated Fermi surfaces in LDA (b) and LDA+SO (c) for various samples.

5.6 Discussion

In the remainder of this chapter we consider some points that are relevant to the current study of strain-induced topological change in the Fermi surface of $Sr(Ba)_2RuO_4$ but could not be addressed directly in the experiment. We attempt to address the question of different γ-band character in the Sr- vs Ba_2RuO_4 grown on the same substrate, $SrTiO_3$ and discuss the different effect of the spin-orbit coupling at the E_F in the two compounds.

5.6.1 Effect of strain and A-site atom on the size of the γ-pocket

The trend of the charge transfer between the in-plane and out-of-plane Ru-4d orbitals that occurs with the tensile in-plane strain in the same compound can be explained by crystal field arguments: the compression of octahedra along z raises the relative energy of the $d_{xz/yz}$ orbitals.

To understand the difference between Sr_2RuO_4 and Ba_2RuO_4 grown on the same substrate, $SrTiO_3$, i.e. having the same in-plane Ru-O distance, a more detailed investigation of the structural parameters needed. To this end we performed optimization of the out-of plane lattice constant and internal structural parameters in Sr_2RuO_4 and Ba_2RuO_4 at different strain states. The calculated bands structure and Fermi surfaces are shown in Figure 5.11. Table A.1 in Appendix A lists all calculated structural parameters of biaxially strained compounds using LDA and GGA exchange-correlation functional. In addition, relaxation of internal coordinates was performed for Sr_2RuO_4 under hydrostatic pressure, for which a and c lattice parameters were fixed to experimental values.

Clearly, considering just the ratio of the Ru-O_z/Ru-O_x bond lengths is not sufficient to explain the difference in the γ-pocket size: from table A.1, Ru-O_z distance in Ba_2RuO_4/STO is larger than in Sr_2RuO_4/STO, which should naively suggest $n(\gamma_{\mathrm{BRO}}) < n(\gamma_{\mathrm{SRO}})$, but the opposite is observed both in experiment and DFT. Since the DFT prediction agrees with experiment, we can find the factors affecting the relative occupations using DFT.

Compound	Structure	n_{xy}	ΔE_γ (meV)	$\Delta E_{\alpha/\beta}$ (meV)	$E_{\mathrm{vHs}} - E_\gamma$ (meV)
Sr_2RuO_4/STO	SRO	0.635	0	0	30
Ba_2RuO_4/STO	SRO	0.647	-75	-55	-22
Sr_2RuO_4/STO	BRO	0.610	60	10	52
Ba_2RuO_4/STO	BRO	0.631	3	-6	13

Table 5.2: Effects of structure and cation substitution on band energies.

To understand the effects of structure and cation substitution on band filling of the γ-band

we use two distinct sets of structural parameters, namely SRO and BRO, corresponding to PBE equilibrium structures of Sr_2RuO_4 and Ba_2RuO_4 on $SrTiO_3$ substrate: out-of-plane lattice constant $c = 12.735$ and $c = 13.544$, respectively, and other parameters given in table A.1. For both structures, we calculate band energies for Ba and Sr on the A-site. The band energy is defined as the energy at 2/3 filling - this choice is due to occupation by $\approx 2/3$ electrons in all three t_{2g} orbitals - relative to the core Ru$-3s$ state energy. Since the absolute band energies calculated by LDA are not reliable to the meV scale, we list the difference of the band energy of a given compound and Sr_2RuO_4/STO in table 5.2.

We conclude that several factors affect the relative energies of d_{xy} vs $d_{xz/yz}$ bands. First, the differences in structure between SRO and BRO. The relative energy of d_{xy} orbital is higher in BRO structure by 50 meV and 30 meV, respectively, for Sr_2RuO_4 and Ba_2RuO_4. This is purely crystal field effect due to difference in c lattice parameter. Second, substituting Ba for Sr for the same structure decreases band energies for both d_{xy} and d_{xz}, but the relative d_{xy} energy is lower by $20 - 40$ meV depending on structural parameters. Also, increasing $z_{\mathrm{Ba/Sr}}$ (i.e. making the A-site atom closer to the Ru-O plane) also reduces the band energies, and again, the effect on d_{xy} is stronger. The combined effect of these two factors almost cancels, i.e. the calculated relative energies of d_{xy} vs $d_{xz/yz}$ are close to within a few meV in both Sr_2RuO_4/STO and Ba_2RuO_4/STO (first and last rows of Table 5.2). So why is Ba_2RuO_4/STO closer to the topological transition? We find that the shape of the gamma band changes when on Ba for Sr substitution. The next-nearest neighbor hopping to direct hopping ratio (t_4/t_1) decreases from 0.40 eV for Sr to 0.36 eV for Ba, which causes the vHs energy to be lowered within the band. This can also be seen from the γ-band occupancy at vHs energy, which is 0.71 and 0.68 calculated from tight-binding parameter of Sr_2RuO_4 and Ba_2RuO_4, respectively.

5.6.2 Spin-orbital splitting at the Fermi level

We observed that ARPES line width of the quasiparticles in Ba_2RuO_4 is consistently larger than in Sr_2RuO_4, irrespective of the particular band. This could not be explained by the broadening from impurity scattering, or low sample quality, since this relation holds even for the lowest quality Sr_2RuO_4 grown on SAGT compared to the highest quality Ba_2RuO_4 grown on $GdScO_3$. We performed fully relativistic density functional calculations to estimate the effect of spin-orbit (SO) splitting on the Fermi surface. The SO interaction is known to have dramatic effect on the orbital and spin character of the low-energy electronic states and the shape of the Fermi surface in Sr_2RuO_4, and in mixing the band characters between the α/β and γ bands along the Brillouin zone diagonal [119]. But the SO splitting on the Fermi surface has low value of $\approx$ 2 meV, and can't be resolved in the current ARPES measurements. Figure 5.12(a) shows the calculated LDA+SO band structure along high-symmetry lines of the BZ for Sr_2RuO_4 and Ba_2RuO_4 (see A for the details of calculations). Strikingly, the calculated spin-orbit splitting at E_F for Ba_2RuO_4/GSO is around 25 meV (5.12(b)), and after accounting for band renormalization, its contribution to the larger line width is very likely.

Furthermore, we find that the average energy splitting around the Fermi surface grows as a function of strain. Although the calculated spin-orbit splitting grows rapidly with strain, from $\approx$ 1 meV in bulk Sr_2RuO_4 to over 20 meV in Ba_2RuO_4 / GSO, it could not be observed in the current experiment most likely due to experimental resolution and finite lifetime broadening from impurity scattering, which can be seen from the simulated ARPES Fermi surface for Ba_2RuO_4 / GSO with realistic value of lifetime broadening Γ_0=15 meV and experimental resolution shown in Figure 5.12(c). The strain dependence deserves a more detailed investigation and could have interesting implications for the spin and orbital character of the low-energy electronic states.

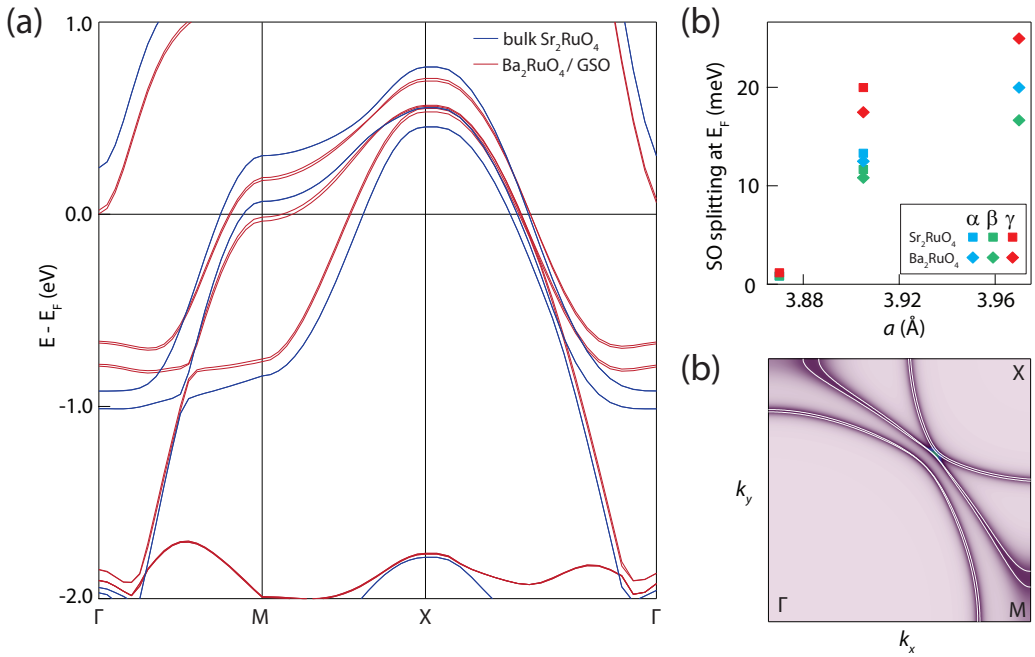

Figure 5.12: (a) LDA+SO band structure in $k_z = 0$ plane for bulk Sr_2RuO_4 and Ba_2RuO_4 / GSO. (b) SO splitting as a function of strain. (c) Simulated ARPES Fermi surface for Ba_2RuO_4 / GSO.

5.7 Conclusions

Our work demonstrates strong inter-orbital electron transfer between the different t_{2g} orbitals with increasing strain, and a topological transition in the γ FS sheet. Previously, such Lifshitz transition was achieved in single crystals by La-doping with La concentrations between 0 and 0.27 [122; 123]. The Fermi surface engineering by strain and chemical pressure presented here has two advantages: it covers a wider range of strain states and is effectively disorder-free, which is instrumental for enhancing superconductivity in Sr_2RuO_4 that is highly sensitive to doping-induced disorder [124]. The detailed parameterization of the evolution of the Fermiology and band masses should allow for testable theoretical predictions for changes in the superconducting state with epitaxial strain.

CHAPTER 6

Effect of strain on quasiparticle dynamics in $(Sr/Ba)_2RuO_4$

In this chapter we study the impact of strain and topological transition in the γ-band on quasiparticle dynamics revealed by transport and ARPES measurements. The proximity of the van Hove singularity (vHs) to the Fermi level has been theoretically shown to enhance the fluctuations of various order parameters and, in some cases, produce the corresponding electronic instabilities, leading to new macroscopic phases such as ferromagnetism, superconductivity, nematic order, etc. We clearly observe the impact of the topological transition in the electrical resistivity and in spectroscopic signatures, when the vHs energy is tuned to within 4 meV of the E_F by synthesizing Ba_2RuO_4 film on $SrTiO_3$. The biaxial strain in the *ab* plane is found to enhance the quasiparticle renormalizations, which are not peaked at the Lifshitz transition but rather increase monotonically as a function of strain.

6.1 Critical fluctuations near Lifshitz transition

We focus on the details of the low-energy electron dynamics in our samples. Between T_c and 25 K, bulk Sr_2RuO_4 behaves as an ideal Fermi liquid with a T^2 resistivity and moderate correlations [121; 125]. The low residual resistivity $\rho_0 < 1\mu\Omega$cm was shown to be essential for superconductivity in bulk samples [126] as well as thin films [84]. The T^2 resistivity is observed for Sr_2RuO_4 and Ba_2RuO_4 films on either side of the Lifshitz transition (Figure 6.1(a)), suggesting the similar coherence scale of the Fermi liquid in this strain states. Close to

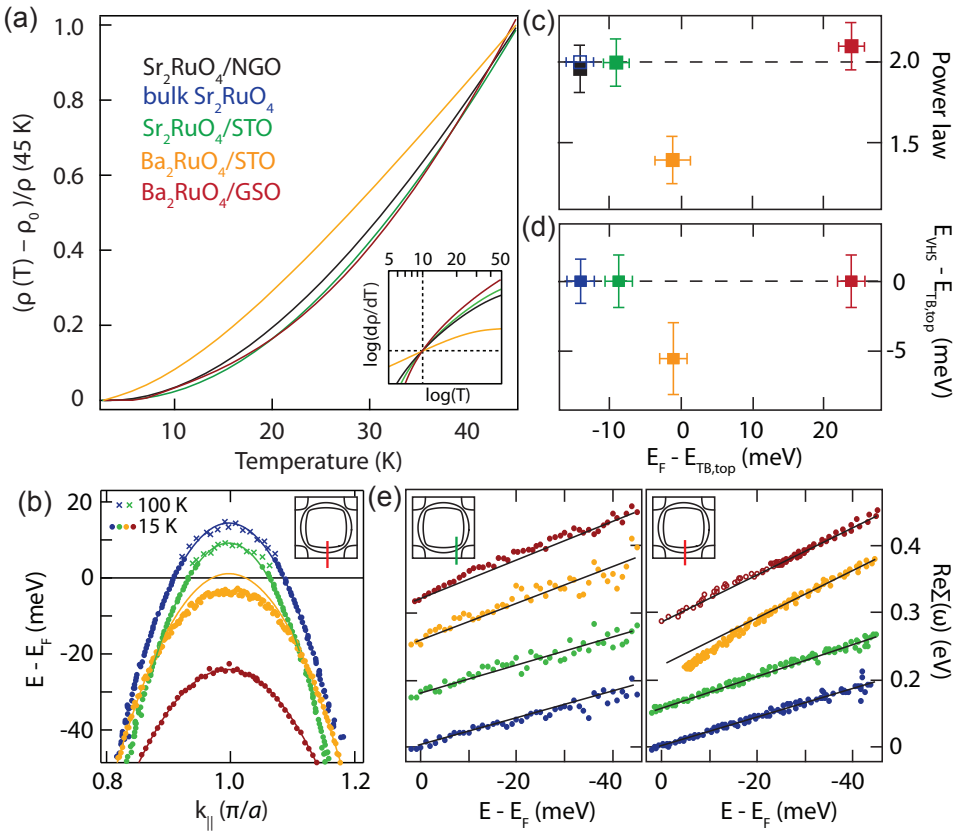

Figure 6.1: Normalized resistivity fitted to $\rho \propto T^n$ (values of n shown in (c) with the open symbol from [125]). The inset shows $\log(d\rho/dT) \approx (n-1)\log(T)$ with an offset. (b) Dispersion of the γ-band along $(0,0) - (0,\pi)$, and (d) the deviation of E_{vHs} from the tight-binding model. (e) $\mathrm{Re}\Sigma(\omega)$ (offset at $E = E_{\mathrm{F}}$ is included for clarity). $\mathrm{Re}\Sigma(\omega) \propto \omega$ implies quadratic energy dependence of the quasiparticle scattering rate $\Gamma(\omega) \propto \mathrm{Im}\Sigma(\omega) \propto \omega^2$ expected for a Fermi liquid. Ba_2RuO_4/STO acquires additional kink-like feature in the real part at the energy scale of 15 ± 10 meV near $\mathbf{k} = (0,\pi)$ (red line cut). This flattens the γ band and pushes the vHs slightly below the Fermi level.

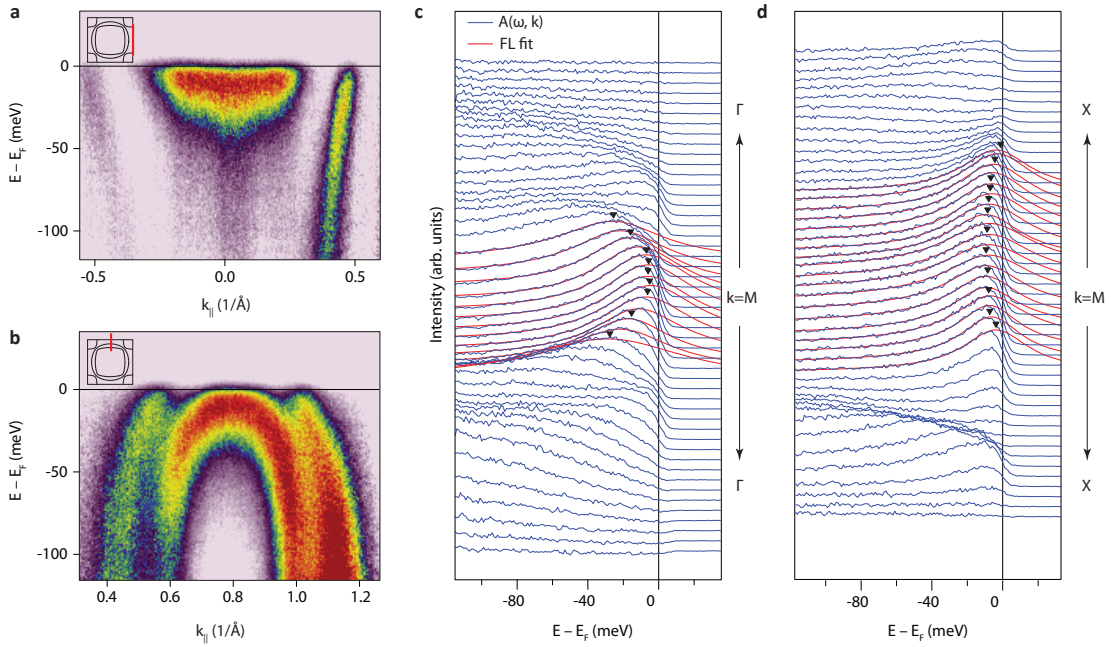

Figure 6.2: ARPES near the van Hove point in Ba_2RuO_4 / STO. Background-subtracted ARPES spectra along (a) (π, k_y) and (b) $(0, k_y)$ across the M point. The EDC's along the two directions shown in (c) and (d) were fitted by the model Fermi-liquid peaks $A_{FL}(\omega)$ multiplied by the Fermi function and broadened by the experimental resolution. The fitted parameters were used to plot the resolution-broadened Fermi-liquid peaks (red lines). The saddle-point vHs energy is 4 meV below the E_F. The dispersion exhibits flattening along both directions.

the Lifshitz transition, however, we observe $\rho(T) \propto T^{1.4\pm0.1}$ up to approximately 25 K in Ba_2RuO_4 / STO as shown in Figure 6.1(a) and 6.1(c).

The quasiparticle dispersion at $(\pi, 0)$ also exhibits a deviation from the calculated band structure precisely at the vHs for Ba_2RuO_4 / STO, as shown in Fig. 6.2. At other strain states, the experimental dispersion at $(\pi, 0)$ can be well described by a tight binding fit. At the critical strain state, however, the dispersion exhibits an anomalous flattening which deviates strongly from both the LDA calculations and the tight binding parameterization, and cannot be ascribed to the finite experimental resolution. This can be represented by a deviation of $\Sigma'(w)$ at $\mathbf{k} = (\pi, 0)$ from a linear dependence at low energy expected for a conventional Fermi liquid and observed at other locations in momentum space for Ba_2RuO_4 / STO (Fig. 6.1). Since the low-energy electronic structure is highly two-dimensional, the measured quasiparticle properties in Ba_2RuO_4 / STO appear to be unaffected by any finite thickness effects.

6.2 Evolution of the quasiparticle renormalizatons in A_2RuO_4

Given the deviations from canonical Fermi liquid behavior, it is natural to investigate whether the strength of quantum many-body interactions is likewise peaked at the Lifshitz transition. To do this, we estimate the change of the overall band masses in the three FS sheets with the energy of vHs. Previous high-pressure studies of quasiparticle mass renormalization suggested that correlation strength is dampened in all bands when moving away from the critical point. This fact was correlated to the observation of decreasing superconducting T_C in the samples under hydrostatic pressure and used to suggest the importance of vHs for the correlations in all bands. This is shown in Fig. 6.3, where the measured quasiparticle dispersions $E(k)$ for the α and β bands are shown as a function of in-plane lattice constant. Fig. 6.3(g-i) summarize the quasiparticle mass renormalization for

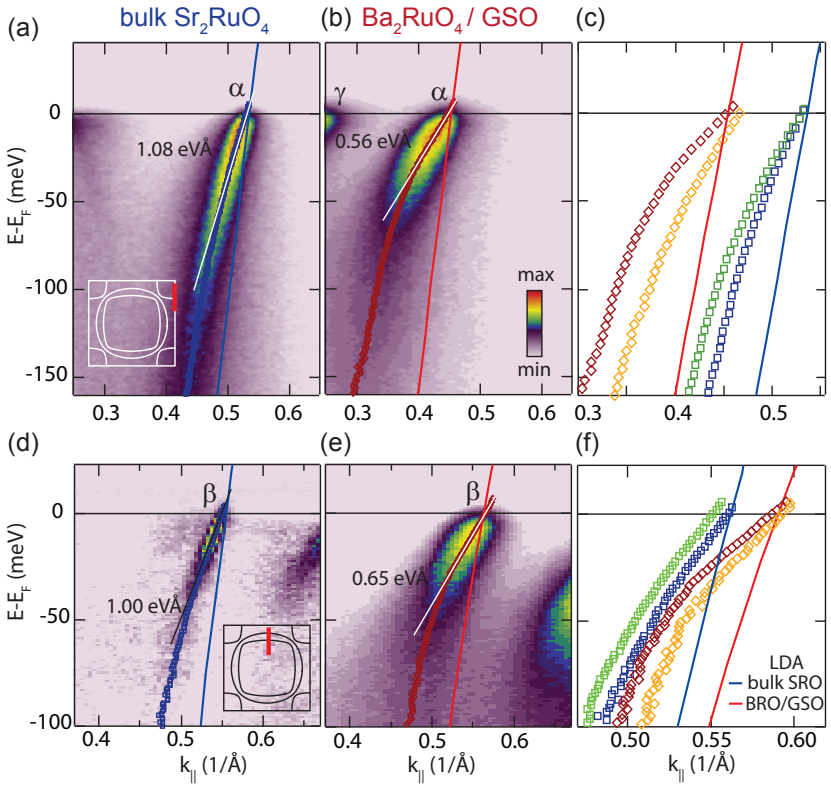

Figure 6.3: Dispersion $E(\mathbf{k})$ of the α band along the BZ boundary (a-c) and β band along (0,0)-(0,π) (d-f). Spectral weight is shown for the single crystal Sr_2RuO_4 (a,d) and Ba_2RuO_4/GSO (b,e). The colors of the open symbols in (c) and (f) are consistent with the colors in Figure 6.4.

all three bands crossing E_F. The mass enhancements were calculated using the dispersion along the line cuts for the α and β bands and averaged over the full BZ for the γ band. The band renormalization presented in Fig. 6.3(i) of the main text was calculated for the total TB band width $W_\gamma = 4t_1 + 8t_4$. It has been established from both quantum oscillations and prior ARPES measurements that the mass renormalization of α and β bands in bulk Sr_2RuO_4 is approximately 2.5–3 [122; 127], consistent with our measurements on single crystals of Sr_2RuO_4. The strength of this renormalization is, however, dramatically enhanced when increasing the Ru-O bond length and substituting the larger A-site cation. Increasing the bond distance by 2.6 % when going from bulk Sr_2RuO_4 to Ba_2RuO_4 on GSO, increases the effective mass of the α band by nearly a factor of 2, far larger than expected than from LDA, which predict less than a 10% change in v_F between these two materials (Figure 6.3(g)), yet a noticeable jump in the renormalization occurs when changing from the Sr to Ba cation at the same lattice constant ($SrTiO_3$). In the α and β bands, a significant component of the mass enhancement arises from a kink in the dispersion (presumably due to electron-boson coupling) around 80 ± 40 meV. Nevertheless, even the dispersion at higher binding energies (greater than 100 meV) is substantially renormalized in going from bulk Sr_2RuO_4 to Ba_2RuO_4 / GSO (a factor of 1.9±0.2 and 1.8±0.4 for the α and β bands, respectively). It is important to note that the mass enhancement is not peaked at the Lifshitz transition, but rather increases monotonically with Ru-O bond distance, consistent with the increase of correlations from the local repulsion U/t and the Hund's coupling [143; 199].

The many-body interactions experienced by electrons, e.g. scattering from bosons and other electrons, is manifested as kinks in the dispersion at the energies of particular modes and as renormalization of the band masses. These many-body effects are encoded in the self-energy correction to the quasiparticle dispersion, which is momentum-independent under the assumption of local interactions. We assume the bare dispersion from the LDA calculations, and extract the real parts of self-energy from the poles of spectral function

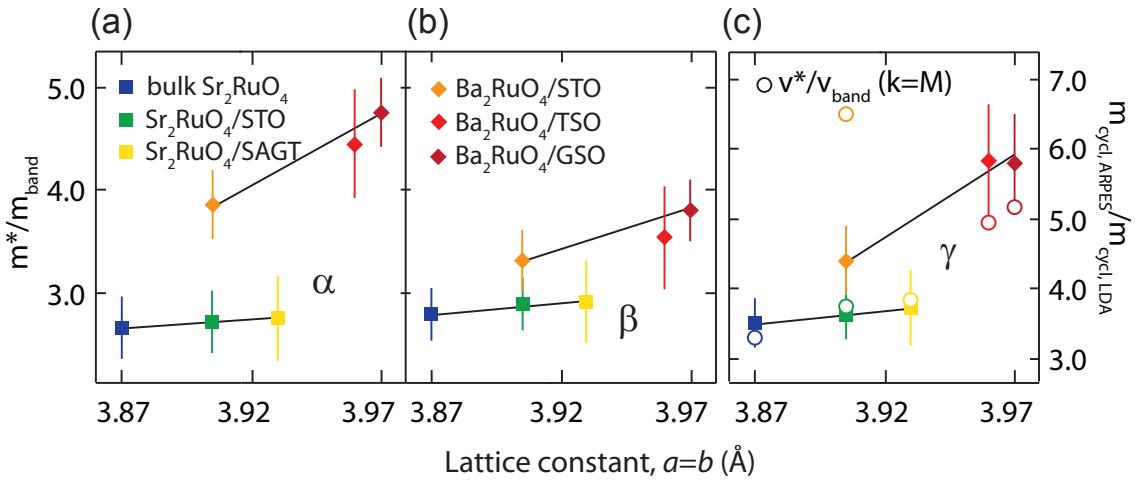

Figure 6.4: Quasiparticle renormalizations for the α-band (a) and β-band (b) have strong monotonic dependence on the strain value. QP renormalization for the γ band (c), calculated as a ratio of the LDA bandwidth to ARPES bandwidth from the corresponding tight-binding fits, shows a similar monotonic increase as a function of tensile strain. The open circles in (c) show the band renormalization from the slope of the real part of self-energy $1 - \partial \mathrm{Re}\Sigma(\omega)/\partial\omega$ near E_F calculated at $\mathbf{k} = (\pi, 0)$. The deviation for Ba_2RuO_4/STO is due to the band flattening shown in Figure 6.2.

measured by ARPES:

$$A(\omega, \mathbf{q}) = -\frac{1}{\pi}\mathrm{Im}\frac{1}{\omega - \epsilon_{\mathbf{q}} - \Sigma(\omega, \mathbf{q})}$$

The well known kink at 40 meV and the broader one at 90 meV are observed in all samples and have the same energy across all strain states. This fact emphasizes essentially the same energy range of the "coherent" Fermi liquid regime in all samples in the quasi-one-dimensional bands. In contrast, the effective bandwidth at low energy drops dramatically with increasing strain. The trivial decrease in the band velocity due to smaller orbital overlap is captured by LDA, and the predicted difference between unstrained Sr_2RuO_4 and $Ba_2RuO_4/GdScO_3$ for the α-band is around -8%. The observed velocities for the two samples are 1.09 eVÅ and 0.58 eVÅ, respectively, a drop by almost a half. The velocity renormalization values for the quasi-one-dimensional α- and β-pockets are shown in fig. 6.3 (e) and (f). Fig. 6.3 (b) and (d) show the dispersion and the real part of self-energy for the γ-band. Due to slight deviation of the dispersion from parabolic in $Ba_2RuO_4/SrTiO_3$ along $\Gamma-M$ linecut (considered in the next

section), we calculate the renormalization of the effective bandwidth $W = 4t_1 + 8t_4$ from the tight-binding parametrization of the equal energy surfaces. This value is plotted in fig. 6.3 (g) and is a measure of overall band renormalization due to local effects. The change in the enhancement values with strain is monotonic with a jump between Sr_2RuO_4 and Ba_2RuO_4. This jump between the two compounds requires further investigation, but the overall trend is qualitatively consistent with the increased correlation effect from the local repulsion U/t. However, just the local U acting in a single orbital may not be enough to explain the magnitude of the effect, particularly in Ba_2RuO_4. DMFT studies [210] shows that the sharp drop in the quasiparticle residue due to a small change in U/t ratio is only possible when the effects of Hund's rule coupling J_H are accounted for. The effect of J_H was shown to be essential to explain the surprisingly low quasiparticle weight and, at the same time, persistent Fermi-liquid regime at elevated temperatures in Sr_2RuO_4. The presented observation is in qualitative agreement with SdH and transport studies under pressure that showed the suppression both of quasiparticle masses and electron-electron scattering rates as measured by the coefficient A in $\rho = AT^2$). We showed that this effect is monotonic in strain and is thus unrelated to the change in the vHs energy relative to the Fermi level.

In Figure 6.5 we show the ARPES spectra and extracted dispersions for the α and β bands in single crystal Sr_2RuO_4 and Ba_2RuO_4 / $GdScO_3$ film over a wider energy range than in Fig. 6.3. The α band velocities dE/dk at binding energy 0.25 eV are 2.56 eVÅ and 1.34 eVÅ respectively for the Sr_2RuO_4 and Ba_2RuO_4 / $GdScO_3$. Similarly, the β band velocities at $E = 0.15$ eV are 1.6 eVÅ and 0.9 eVÅ, respectively for the two samples. These large differences extending to the energy scale exceeding the typical energies of the bosonic modes indicate that the renormalization difference between the samples is unlikely merely due to the change in electron-phonon couplings caused by the alteration of the phonon spectra.

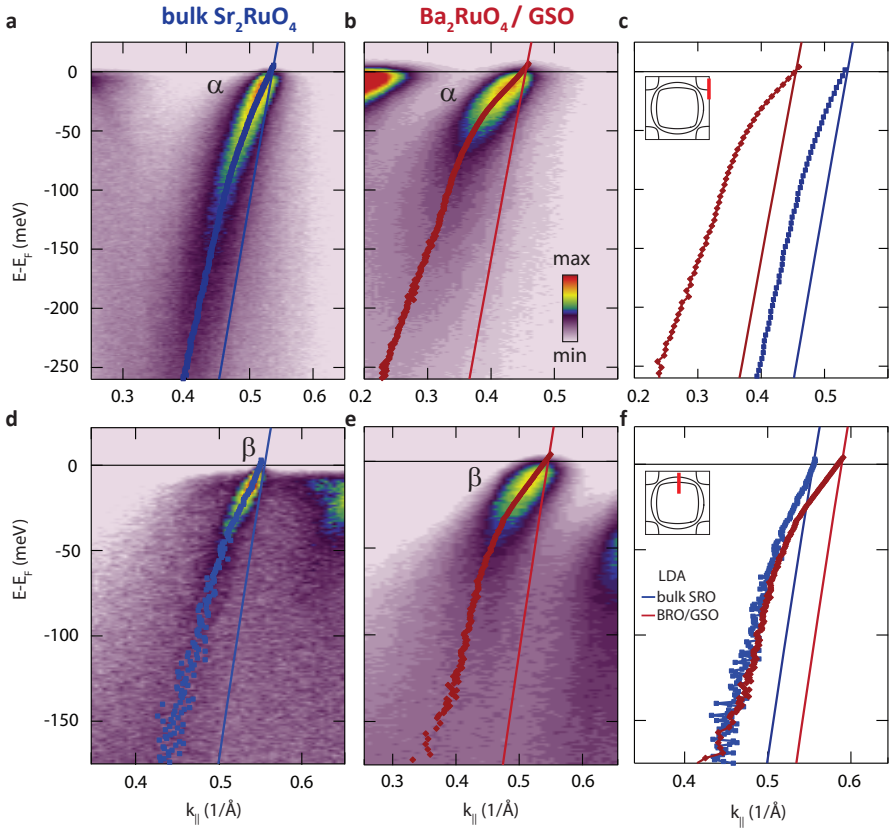

Figure 6.5: ARPES spectra from the bulk Sr_2RuO_4 single crystal and the Ba_2RuO_4 / GSO film showing the α and β band dispersions extending to 0.26 eV and 0.18 eV, respectively.

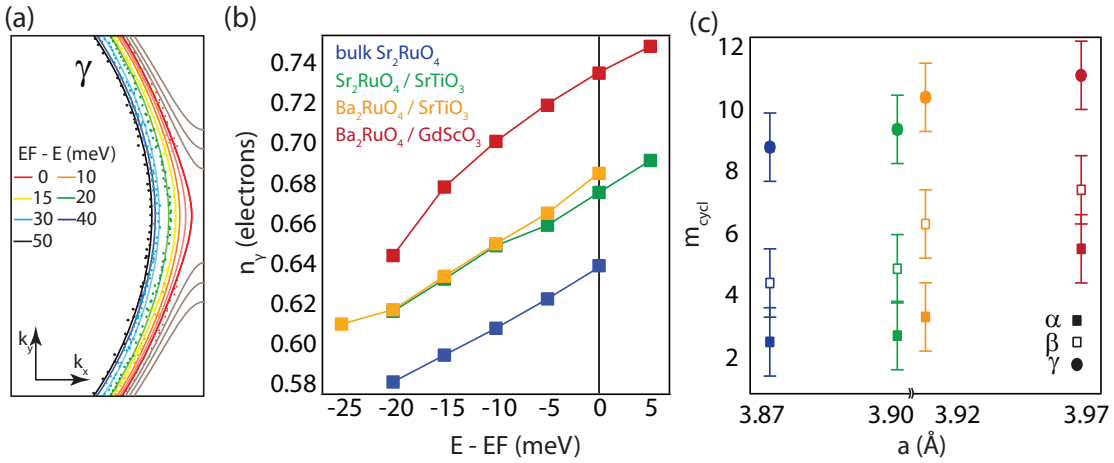

Figure 6.6: Cyclotron mass extraction from ARPES spectra (see text for the details).

6.3 Cyclotron mass

To get the mass renormalization from total bands mass averaged around the Fermi surface we followed the procedure used, for example, in [128]. The ARPES spectral weight is measured on a significant portion of the Brillouin zone, and then sliced into energy-momentum spectra. Then the QP pole positions are extracted within $\sim 10^2$ meV of the Fermi energy for a given band at different (k_x, k_y) momenta. By symmetrizing these energy momentum points, one can calculate the momenta of poles located at a constant energy E (Figure 6.6(a)). The area bounded by these momenta A is proportional to the band occupation $n_\gamma(E)$ between the band bottom and energy E (Figure 6.6(b)). The cyclotron mass is then determined by the slope of $n_\gamma(E)$ at E_F: $m_{cycl} \propto \partial n_\gamma(E)/\partial E|_{E=E_F}$. The cyclotron masses of the bulk Sr_2RuO_4 found this way agree with the thermodynamic masses reported in de Haas van Alphen measurements [129; 130].

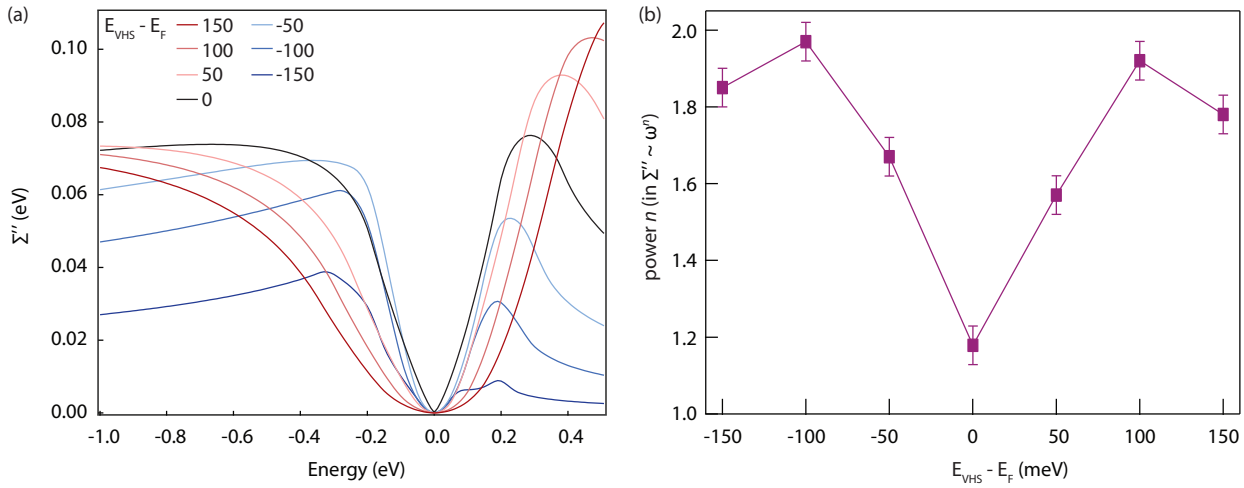

Figure 6.7: (a) The imaginary part of the self-energy for different vHs energies relative to the E_{F}. (b) Power-law exponent of the energy dependence of the imaginary part. As the vHs energy is varied near the E_{F} the quasiparticle scattering phase space can change dramatically, giving rise to non-Fermi-liquid-like scattering rates.

6.4 Discussion

In this subsection we investigate the possible changes in imaginary part of self energy due to the changed phase space for electron-electron scattering rates. In any Fermi system, the Pauli principle limits the mutual scattering of fermions. A qualitative argument is that two fermions can interact effectively if their energies happen to be within the interval T around the Fermi energy, where T is temperature. The probability that one of the energies is within this interval is of order T/E_F and, since the particles are independent, the scattering probability is proportional to $(T/E_F)^2$. In the above qualitative argument, it was implicitly assumed that the density of states is a smooth and nearly constant function near the Fermi energy. But what happens if there is peak in the density of states, such as a van Hove singularity? We follow [131] in their calculation of the scattering rates measured by ARPES in Sr_2RuO_4. The imaginary part of self energy due to Coloumb interaction within the γ-band in the second order is

$$\Sigma''_{xy}(\omega) = U^2 R_{111}(\omega) + 2J^2 R_{122}(\omega) + 4(U'^2 + J^2 - U'J)R_{212}(\omega),$$

where

$$R_{jkl}(\omega) = \left(\int_0^\infty \int_{-\infty}^0 \int_{-\infty}^0 + \int_{-\infty}^0 \int_0^\infty \int_0^\infty\right) d\omega_1 d\omega_2 d\omega_3 \times \rho_j(\omega_1)\rho_k(\omega_2)\rho_l(\omega_3)\delta(\omega + \omega_1 - \omega_2 - \omega_3).$$

To get quantitatively accurate results the scattering rates are calculated using self-consistent quantum Monte Carlo scheme in [131]. Here, we assume very weak interactions and limit ourselves to the lowest order perturbation term. Figure 6.7 shows the imaginary part of self-energy calculated for the density of states from tight-binding model. The varied parameter is the difference $E_{vHs} - E_F$. When vHs is sufficiently far from the Fermi level the Fermi-liquid-like dependence $\Sigma''(\omega) \propto \omega^n$ with $n \approx 2$ is observed. On the contrary, when $E_{\mathrm{vHs}} \approx E_F$, values of n are lower, and the minimum is about $n \approx 1.2$ for $E_{\mathrm{vHs}} \approx E_F$. This agrees with our experimental observation of Fermi-liquid-like power laws for all samples except for Ba_2RuO_4 / STO.

6.5 Possibilities for enhancement of the superconducting T_C in $(Sr/Ba)_2RuO_4$ by strain engineering

Superconducting ground state in Sr_2RuO_4 is extremely sensitive to disorder, caused by random impurities or crystal defects [126]. This is because the anisotropic gap function of any unconventional superconductor can be averaged to zero by elastic scattering around the Fermi surface if the mean free path is comparable to the coherence length. This is not an issue for most of unconventional superconductor families, like cuprates and iron-based superconductors with typical coherence length values of $\xi \approx 2$ nm and $\xi \approx 3$ nm, respectively [132]. The in-plane coherence length in Sr_2RuO_4 is $\xi_{ab} = 66$ nm, and this precludes the enhancement of T_c in Sr_2RuO_4 through chemical substitution and had hindered for a long time growth of superconducting thin films [84].

This makes Sr_2RuO_4 an ideal candidate to explore the effects of biaxial strain and

chemical pressure on the electronic structure and superconducting state. A number of experiments have already demonstrated the response of superconducting T_c in Sr_2RuO_4 to pressure and strain: hydrostatic pressure was shown to suppress both the T_c [133] and quasiparticle enhancements in the normal state [134], recent experiments applying a uniaxial strain of 0.2% demonstrated a strong nonlinear enhancement of T_c [147; 200], in-plane uniaxial pressure was found to induce a higher-T_c superconducting phase [215], and local strains near dislocation were shown to enhance the T_c by a factor of two relative to bulk [197]. Obtaining uniaxial strains of greater than 0.5% is a challenge in rather brittle metal oxides, but biaxial strains of 2-3% are readily achievable in epitaxial thin films grown on deliberately lattice mismatched substrates.

Below, we give some consideration to the interplay between the van Hove singularity energy and superconductivity and possible implications of the current work to the study of triplet superconductivity in ruthenates. The vHs near E_F has been discussed in the context of producing various Fermi liquid instabilities, e.g. van Hove scenario of superconductivity in cuprates [135–137], possible superconductivity in heavily doped graphene [138–140], itinerant ferromagnetism[141; 142]. It was shown to lead to heavier bands and anisotropic mass renormalization in Sr_2RuO_4 [143]. In the earlier theories of SC in Sr_2RuO_4 the FM fluctuations due to proximity of vHs to E_F were considered as the main candidate for the bosonic glue in analogy to superfluid phase in He-3. The topology of the Fermi surface plays a crucial role in the low-energy electron dynamics. Together with short-range screened Coloumb repulsion it defines the effective quasiparticle interaction with a complex long-range structure that in general has both attractive and repulsive regions.

The Lifshitz transition has a profound impact on the electron-hole susceptibility, as shown by the Lindhard susceptibility for the 2D γ band and the 1D α and β bands calculated using a tight binding parameterization of the experimental FS wavevectors and dispersion. Lindhard

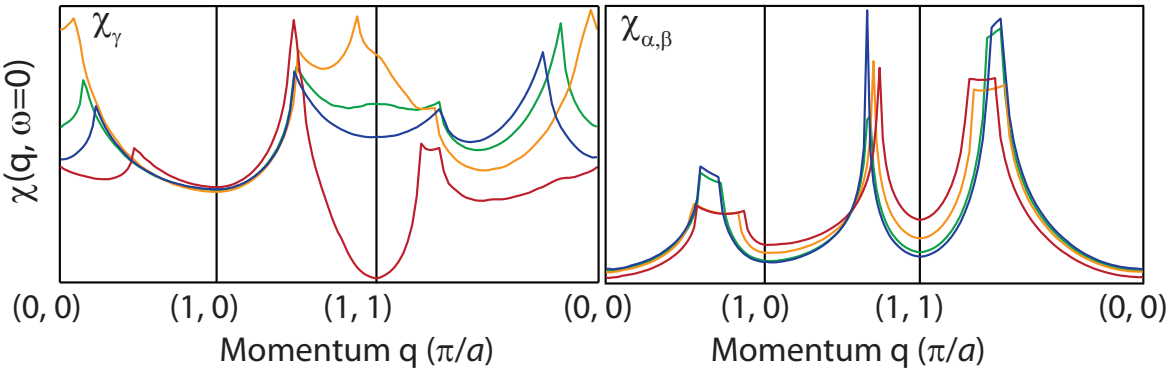

Figure 6.8: Particle-hole susceptibility for the two-dimensional (left) and one-dimensional (right) bands.

function, or magnetic response function of the non-interacting electron system written as

$$\chi_0(\mathbf{q},\omega) = \frac{1}{N}\sum_{\mathbf{k}} \frac{f_{\mathbf{k}+\mathbf{q}} - f_{\mathbf{k}}}{\omega + i0^+ - \epsilon_{\mathbf{k}+\mathbf{q}} + \epsilon_{\mathbf{k}}}$$

is the building block of the effective quasiparticle interaction [144]. In the above equation, $\epsilon_{\mathbf{k}}$ is the single-particle dispersion relation for momentum $\mathbf{k}$, $f_{\mathbf{k}}$ is the Fermi distribution function, N is the number of momenta in the Brillouin zone. Only intraband scattering for γ is considered, while both intra- and inter-band scattering between the 1D α and β bands is allowed. For the 1D bands, $\chi_{\alpha,\beta}(\mathbf{q},\omega=0)$ is relatively independent of strain, except for the reduced nesting in Ba_2RuO_4 due to its stronger two-dimensionality. For the γ band, however, $\chi_\gamma(\mathbf{q},\omega=0)$ exhibits dramatic changes with strain, where $\chi_\gamma(\mathbf{q}=(0,0))$ is strongly enhanced approaching the Lifshitz transition. There is also a corresponding increase of $\chi_\gamma(\mathbf{q}=(\pm\pi,\pm\pi))$, since that wavevector connects the vHs at $(0,\pi)$ and $(\pi,0)$ to symmetry-equivalent pairs.

To estimate the main effect of vHs energy on the pairing strength, we follow [144] in building a simple mean-field theory of superconductivity assuming the effective interaction between quasiparticles to be of magnetic origin and built out of the Lindhard function. Since the dominant quasiparticle interaction is assumed to be magnetic, then effectively the system

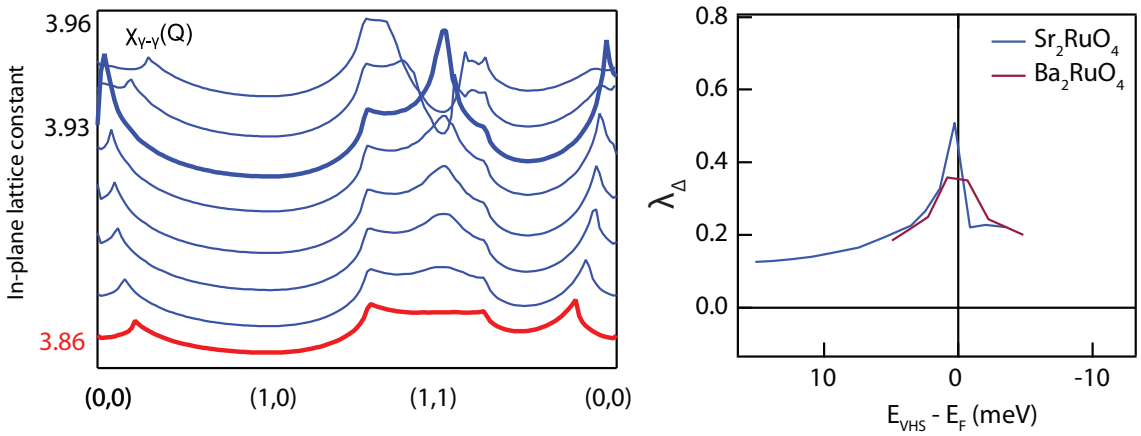

Figure 6.9: Tuning χ_γ by varying the in-plane lattice parameter (left) and the corresponding variations of the SC interaction parameter in the p-wave channel (right).

is on the border of long-range magnetic order and magnetic response is strongly enhanced relative to the noninteracting system. The enhanced susceptibility is then

$$\chi(\mathbf{q},\omega) = \frac{\chi_0(\mathbf{q},\omega)}{1 - I_{eff}\chi_0(\mathbf{q},\omega)},$$

where I_{eff} is the appropriate molecular field constant. To estimate the strength of superconducting pairing in different strain states, we calculate the interaction parameter [144]:

$$\lambda_\Delta = -\frac{\langle V_\Delta(\mathbf{k}-\mathbf{k}',\omega=0)\eta_\Delta(\mathbf{k})\eta_\Delta(\mathbf{k}')\rangle_{FS(\mathbf{k},\mathbf{k}')}}{\langle \eta_\Delta^2(\mathbf{k}')\rangle_{FS(\mathbf{k},\mathbf{k}')}},$$

where interaction $V_p(\mathbf{q},\omega) = -\frac{1}{2}I^2\chi_(\mathbf{q},\omega)$ and $\eta_p(\mathbf{k}) = \sin(k_x)$ or $\eta_p(\mathbf{k}) = \sin(k_y)$ in the p-wave channel. The interaction parameter is shown in Figure 6.9 as a function of $E_{\mathrm{vHs}} - E_{\mathrm{F}}$ calculated for tight-binding parametrization of Sr_2RuO_4 and Ba_2RuO_4. The superconductivity is enhanced near the Lifshitz transition in this naive model.

To gain a better understanding of the effects of strain engineering on superconductivity, we provided the tight-binding parametrization of the ARPES band structure to Prof. Eun-Ah Kim and student Yi-Ting Hsu at Cornell University, who used the weak-coupling renormalization-group approach [145] to investigate superconducting instability in different

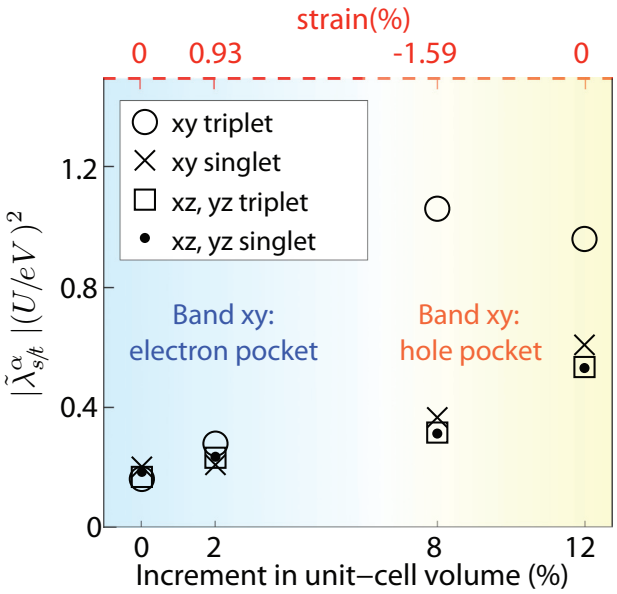

Figure 6.10: The magnitudes of the most negative eigenvalues (vertical axis, see Hsu et al. [146]) of different channels for the four representative samples. In the order of increasing volume of one unit cell, the ticks on the horizontal axis mark the four representative samples: the bulk Sr_2RuO_4 (0%), and the films Sr_2RuO_4/STO (2%), Ba_2RuO_4/STO (8%), and Ba_2RuO_4/GSO (12%). The percentage refers to the increase in the volume of one unit cell compared to that of the unstrained bulk Sr2RuO4. The upper horizontal axis shows the in-plane strain of each Sr_2RuO_4 and Ba_2RuO_4 sample defined with respect to the bulk Sr_2RuO_4 and Ba_2RuO_4/GSO, respectively. Reproduced from [146].

channels (i.e. singlet vs. triplet) and different Fermi surfaces. The results, reproduced from [146], are presented in figure 6.10.

6.6 Conclusions

In conclusion, we compare strain-induced modifications to prior carrier doping studies [122]. One advantage of strain is the potential to investigate its impact on superconductivity and T_c, whereas chemical disorder destroys superconductivity. Like in doped $Sr_{2-y}La_yRuO_4$, we observe signatures of criticality (e.g. $\rho \propto T^{1.4}$ behavior) at low temperatures near the Lifshitz transition [123]. Some effects of criticality might be partially masked by disorder which can be improved in future generations of thin films. The impact of electron doping on

the electronic structure of $Sr_{2-y}La_yRuO_4$ could be well described by a simple rigid band shift model, and there was no change in the mass renormalization, even past the Lifshitz transition. In contrast, epitaxial strain impacts the electronic structure in more profound ways, including inducing large increases in the mass renormalization, and an unexpected band flattening near the Lifshitz transition. The strength of the low-energy kink around 80 meV in the α and β bands are also greatly enhanced in Ba_2RuO_4 versus Sr_2RuO_4, suggesting an increased electron-phonon interaction, which was not reported in $Sr_{2-y}La_yRuO_4$. In comparison to the prior work on uniaxial strain [147], our calculations indicate that the impact on the electronic structure along the strained direction is comparable to the effects of biaxial strain. However, under uniaxial strain the C_4 symmetry is broken, and therefore one pair of van Hove singularities is lowered, while the orthogonal pair is raised in energy. Nevertheless, the uniaxial strain experiments suggest that superconductivity may be strongly intertwined with lowering the vHs, and therefore we speculate that biaxial strain could likewise be a promising route towards enhancing T_c.

Our work is the first demonstration of controlling Fermi surface topology and quantum many-body interactions in ruthenates via epitaxial strain engineering and negative chemical pressure, opening the door to future possibilities for engineering quantum many-body ground states in a disorder-free manner to explore enhanced superconductivity, quantum criticality, or electronic nematic states. Tuning the γ FS sheet precisely to the Lifshitz transition allows us to place the system at the onset of quantum criticality and observe deviations from canonical Fermi liquid behavior.

CHAPTER 7

Observation of the quantum well states in ultrathin $BaRuO_3$ films

Quantum confinement is a powerful tool for manipulating the electronic and magnetic properties of electronic materials, for instance, in the formation of two-dimensional electron gases in AlGaAs-GaAs based heterostructures, or at the interface between $LaAlO_3$ and $SrTiO_3$. In this chapter we demonstrate the effects of quantum confinement on the electronic structure and transport in atomically thin films of the cubic ruthenate $BaRuO_3$, a close analogue of $SrRuO_3$ and $CaRuO_3$.

7.1 Introduction

When strongly correlated electrons are confined, broken symmetry, strain and reduction of dimensionality often lead to exotic new phenomena distinct from bulk, for example, magnetism and superconductivity in two-dimensional electron gas at $LaAlO_3/SrTiO_3$ heterostructure, massive enhancement of superconductivity in monolayer FeSe grown on $SrTiO_3$ (100 K vs 8 K in bulk), transition from indirect to direct band gap in monolayer transition metal dichalcogenides MoS_2 and WSe_2, new topological phases (topological insulator CdTe/HgTe, valley Hall effect in graphene, Rashba effect, FFLO). Persistent FM fluctuations in the 2D limit have been suggested to be important for spin-triplet Cooper pairing and led to proposals to artificially design a spin-triplet superconductor (TSC) by introducing magnetic correlations from a frustrated system (quantum spin liquid) into

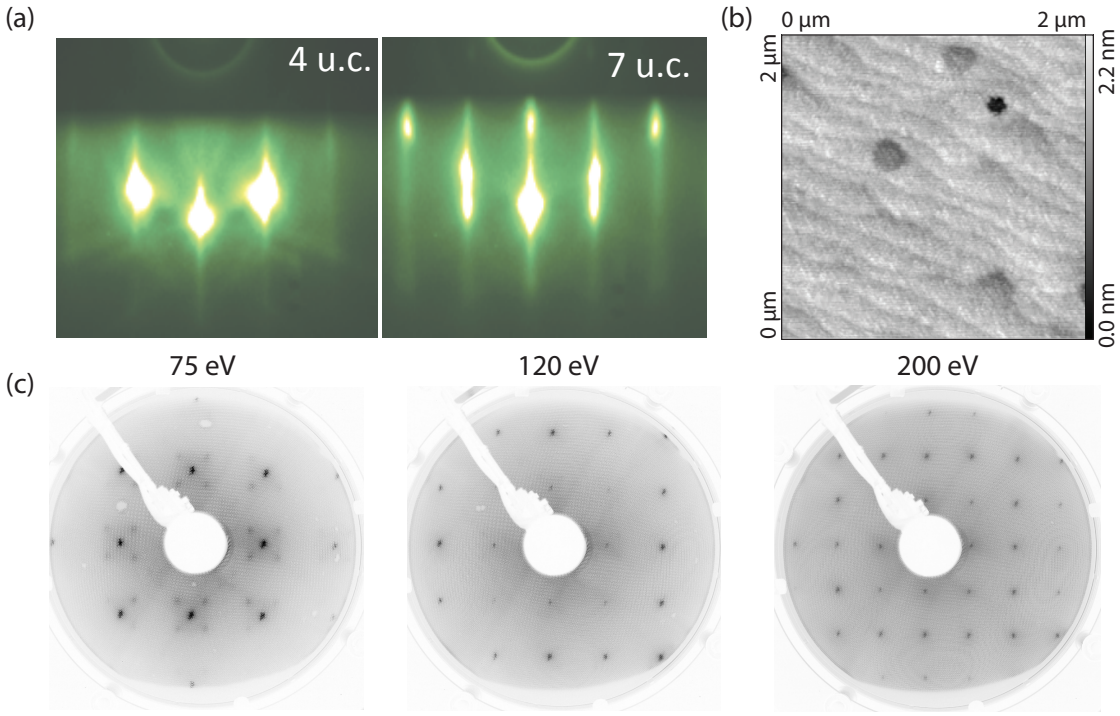

Figure 7.1: (a) RHEED image of $BaRuO_3$ film grown on $SrTiO_3$. After depositing five atomic monolayers, additional peaks appear indicating formation of a secondary phase. (b) Atomic force micrograph of the 3 monolayer sample HP1459. (c) Low-energy electron diffraction pattern of the same sample HP1459. Reconstructions peaks are observed at electron kinetic energies below 120 eV.

metals at their interface [148]. Thanks to ferromagnetic correlations, perovskite ruthenates are a promising system for engineering two-dimensional electronic states. Attempts to engineering TSC in ultrathin films by dimensionally suppressing the FM order in $SrRuO_3$ can be hindered by metal-insulator transition at critical thickness [149; 150], similarly observed in other transition metal oxides ($LaNiO_3$, $La_{2/3}Sr_{1/3}MnO_3$, $SrVO_3$). Understanding the nature of low-dimensional transport and its relation to the underlying electronic structure is essential to engineer new functionality, but it is often hard to separate the role of intrinsic (electronic reconstruction) vs. extrinsic (disorder) effects due to the complex interactions and reconstructions at interfaces and surfaces. A combination of transport and spectroscopic studies may offer unique insights for this problem [151; 152].

$BaRuO_3$ provides an ideal platform to investigate the effect of quantum confinement on

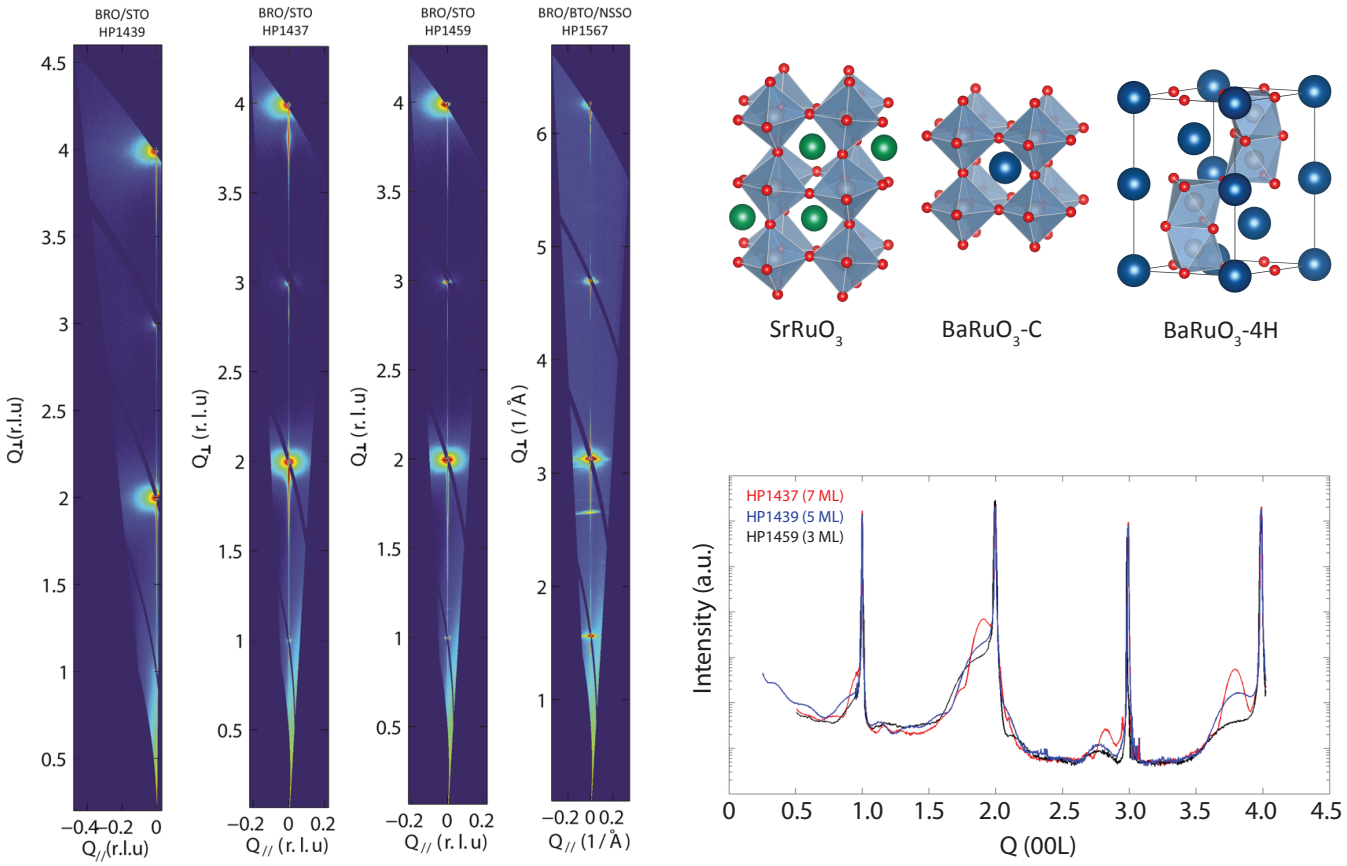

Figure 7.2: Reciprocal space mapping near specular reflection of select $BaRuO_3$ samples (left) and crystal structure of $BaRuO_3$ and $SrRuO_3$ (top right).

the emergent properties of ruthenates. The large Ba cation should prevent structural reconstructions (octahedral rotations) near the interfaces, and, thanks to the cubic symmetry, the low-dimensional electronic structure of $BaRuO_3$ should be relatively simple, in contrast to $SrRuO_3$ and $CaRuO_3$, where $GdFeO_3$-type distortions (Figure 7.2) result in a larger unit cell (4 Ru atoms / unit cell) and a much more complex band structure [153; 154]. Additionally, $BaRuO_3$ may offer a unique insight into ferromagnetism of perovskite ruthenates as a case where, despite a stronger van Hove peak in the density of states at the Fermi level (E_F) compared to $SrRuO_3$, the FM order is weaker, as manifested by a lower bulk T_C and proximity to the pressure-controlled quantum phase transition [155].

7.2 Growth and characterization of $BaRuO_3$ films

$BaRuO_3$ can be crystallized in a number of structures, including the 9R, 4H, and 6H polytypes, depending on pressure during growth and differing by the number of layer boundaries with corner/edge sharing octahedra. Cubic perovskite 3C phase requires highest growth pressure and has been synthesized only recently in polycrystalline form under 18 GPa of pressure [156]. Until this work, there have been no experimental reports on single crystalline cubic $BaRuO_3$, either in bulk or thin film form. Thin films of $BaRuO_3$ studied here were grown by reactive oxide molecular beam epitaxy (MBE) at 600°C and 2 $\times 10^{-7}$ torr of 10% distilled O_3 on $SrTiO_3$ substrates. The lattice mismatch between $SrTiO_3$ (3.905 Å) and $BaRuO_3$ (4.0059 Å) indicate that the films are under 2.5% compressive strain at room temperature. Above a critical thickness of 5 u.c., the films converted to a secondary phase, likely either the 4H or 6H hexagonal polytypes, which revealed itself as additional diffraction peaks in RHEED, as shown in Figure 7.1(a). Therefore, all the thin films that we report in this study range from 2-4 u.c. thickness.

In addition to the films on $SrTiO_3$ substrate, we have attempted to grow films on (Nd,Sm)ScO_3 and $KTaO_3$ substrates. Both substrates are lattice matched to bulk $BaRuO_3$. In case of (Nd,Sm)ScO_3, due to octahedral rotations in the substrate, a 10 nm thick buffer layer of $BaTiO_3$ was used. The sample grown on these substrates all showed semiconducting behavior by resistivity measurements, however, in the best samples we could observe weak dispersive spectral features crossing the Fermi level. For example, the ARPES Fermi surface for the film on (Nd,Sm)ScO_3 is shown in Figure 7.9(c). The fact that the highest quality films could be grown on $SrTiO_3$ substrate could probably be expected. As an order of magnitude estimate, by employing the LSDA value for bulk modulus of $BaRuO_3$ of 206 GPa [158], the pressure of 18 GPa translates to compression along each axis by 2.9%, which is very close to the strain value of 2.5% provided by the $SrTiO_3$ substrate.

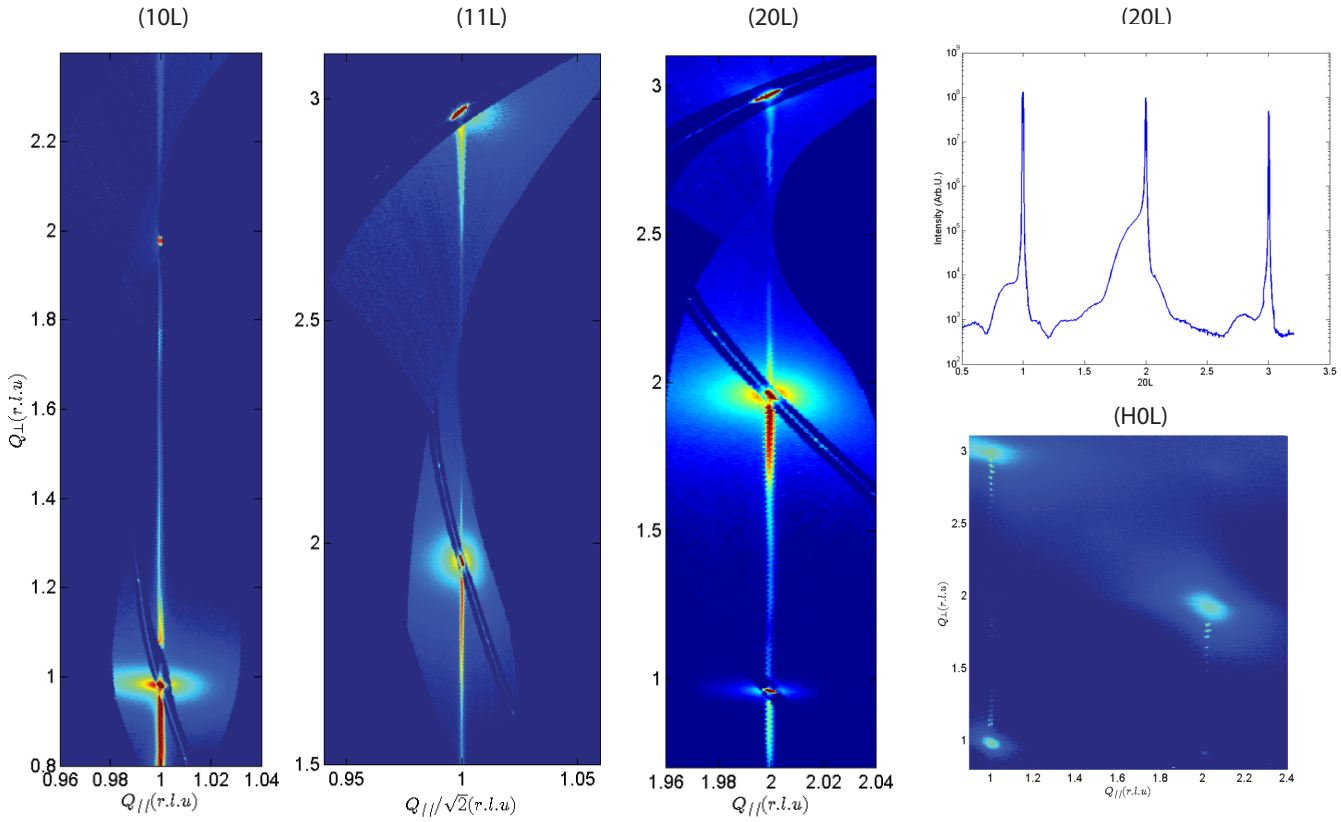

Figure 7.3: Reciprocal space mapping for the off-specular reflection for sample HP1439 (5 ML / STO). No extra peaks are observed that would be expected for hexagonal and rhombohedral polytypes of $BaRuO_3$ [157].

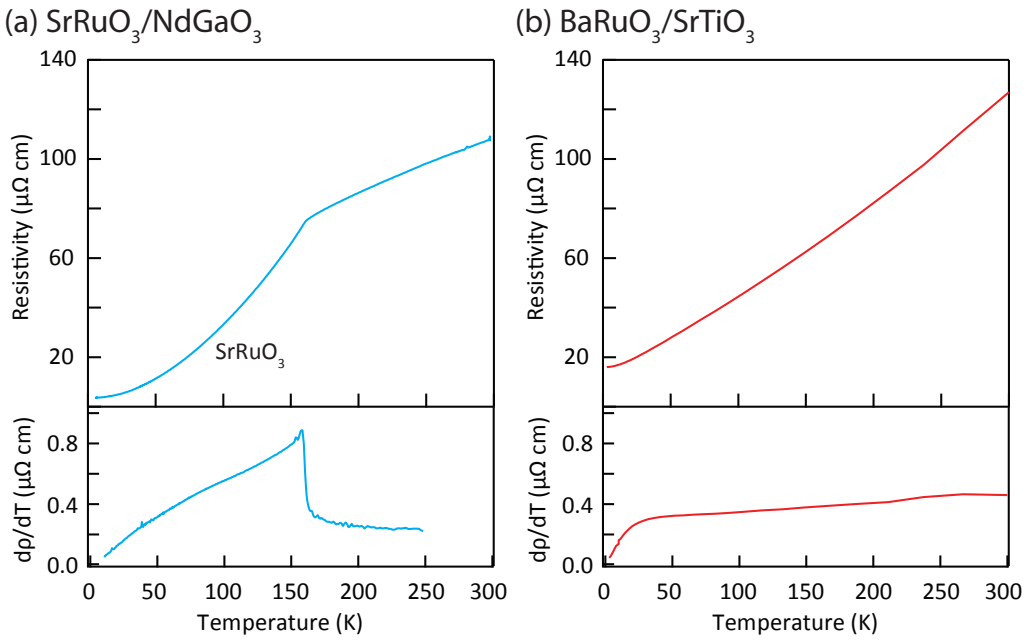

Figure 7.4: Temperature dependence of resistivity of $SrRuO_3$ and $BaRuO_3$ thin films. The data for $SrRuO_3$ is reproduced from [153].

In Figure 7.1(b,c) we show atomic force micrograph and LEED patterns of a 3 u.c. thick sample. The reconstruction peaks are observed in LEED images recorded for incident energy below 120 eV. Their explanation requires a further investigation, however, we believe these diffraction peaks are surface-related. First, we did not observe any corresponding peaks in synchrotron x-ray diffraction measurements, and second, we did not observe corresponding reconstructions in the ARPES spectra.

In Figures 7.2 and 7.3 we show structural characterizations of our $BaRuO_3$ thin films by synchrotron x-ray diffraction at the Cornell High-Energy Synchrotron Source. The absence of extra peaks expected for hexagonal and rhombohedral phases [157] confirms the cubic Pm-3m space group of the thin films.

In Figure 7.4, we also show electrical resistivity measurements of $BaRuO_3$ which reveal a number of crucial features about these samples. First, the residual resistivity ratio, RRR $= \rho_{300K}/\rho_{4K}$ is as large as 7, indicating the extremely high quality of these atomically thin

films. To our knowledge, this represents the highest RRR reported on a metallic oxide thin films of 4 u.c. thickness. The RRR for the film of 3 u.c. thickness synthesized at the same conditions is 4, which may suggest electronically inactive atomic layer at the interface or surface. Second, the electrical resistivity is smooth and featureless, without any sign of a kink in the resistivity that typically signals the transition into the ferromagnetic state seen in $SrRuO_3$ and bulk $BaRuO_3$, indicating that these $BaRuO_3$ films are paramagnetic.

In Figure 7.5, we also show valence band spectra from $BaRuO_3$ which clearly show both the O 2*p* and Ru 4*d* states, in close similarity to $SrRuO_3$, and in qualitatively good agreement to the paramagnetic DOS calculated using the generalized gradient approximation (GGA) in the Wien2K package. Near E_F we observe clear coherent quasiparticles (Figure 7.6). The low-energy band structure is discussed below.

7.3 Basic electronic structure of cubic $BaRuO_3$

As mentioned earlier, one advantage to studying cubic 3C $BaRuO_3$ over its isovalent cousins $SrRuO_3$ and $CaRuO_3$ is that its electronic structure should be much simpler. Due to the octahedral rotations and tilts in $SrRuO_3$ and $CaRuO_3$, the orthorhombic unit cell contains 2 unique individual Ru atoms, resulting in a complicated near-E_F electronic structure due to the reduced Brillouin zone. For example, density functional theory calculations for ferromagnetic $SrRuO_3$ predict 12 individual bands within 0.5 eV of E_F and 6 individual bands within 0.5 eV of E_F for paramagnetic $CaRuO_3$, coming from Ru 4d-t_{2g} orbitals. That is 3 t_{2g} orbitals in each of the 2 atoms with 2 non-degenerate spin states in the ferromagnetic case. In contrast, cubic $BaRuO_3$ has only a single Ru atom per unit cell, which leads to a much simpler electronic structure with only three bands at the E_F for nonmagnetic calculation. In Figure 7.7, we show density functional calculations for the bulk Fermi surface topology of nonmagnetic cubic $BaRuO_3$, together with the FS topology in the $k_z = 0$ plane (Figure 7.7).

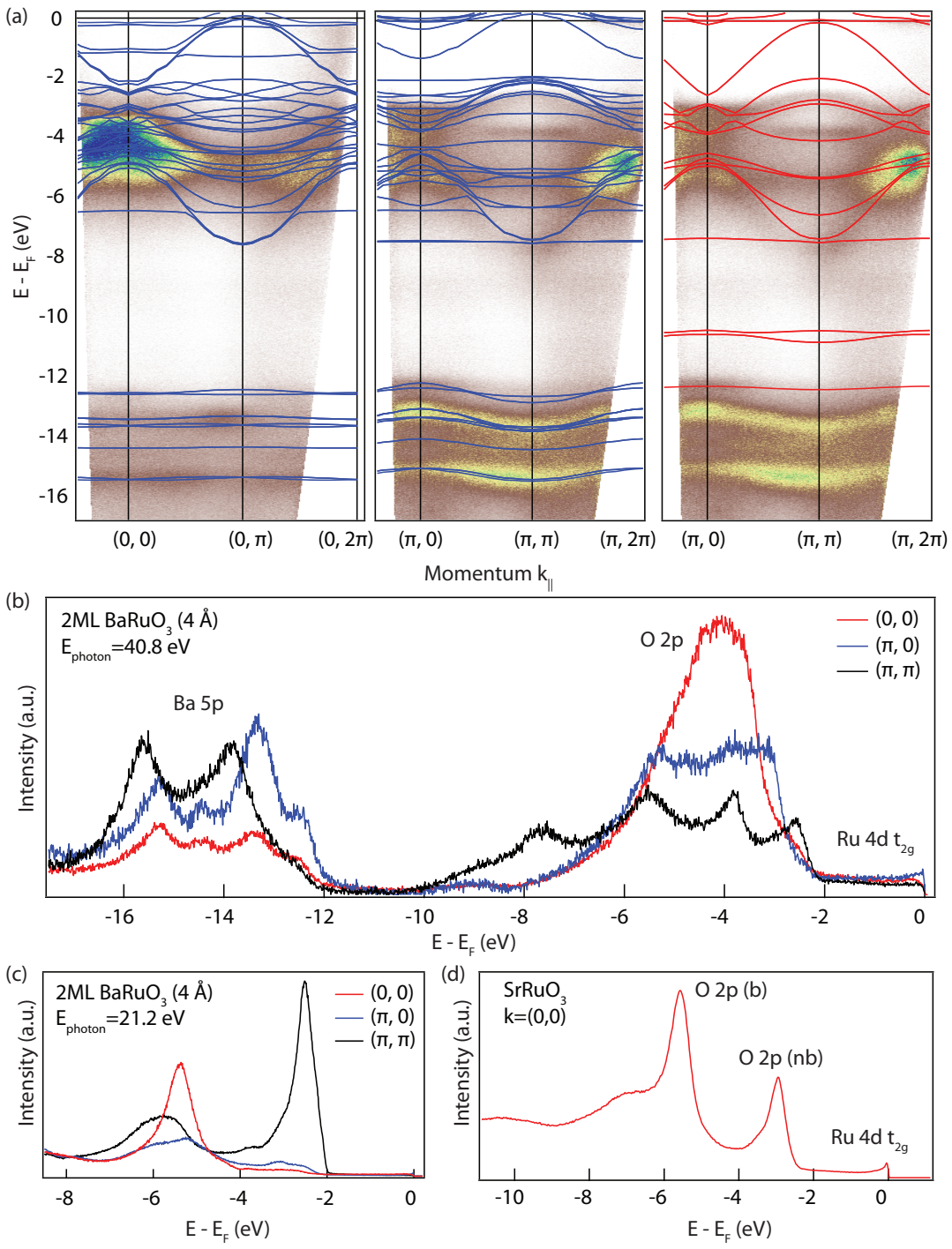

Figure 7.5: (a) Photoemission spectra of 2 u.c. thick $BaRuO_3$ film grown on (Nd/Sm)ScO_3 with in-plane lattice parameter a_p = 4.00 Å along high-symmetry lines measured with E_{photon} = 40.8 eV. Solid lines show bands from density-functional theory calculations for 2 monolayer slab (dark blue) and bulk (red) for comparison. (b) Energy distribution curves (EDC) for spectra in (a) at high-symmetry points of the BZ measured with E_{photon} = 40.8 eV. (c) and (d) EDC's measured with E_{photon} = 21.2 eV for $BaRuO_3$ and $SrRuO_3$, respectively.

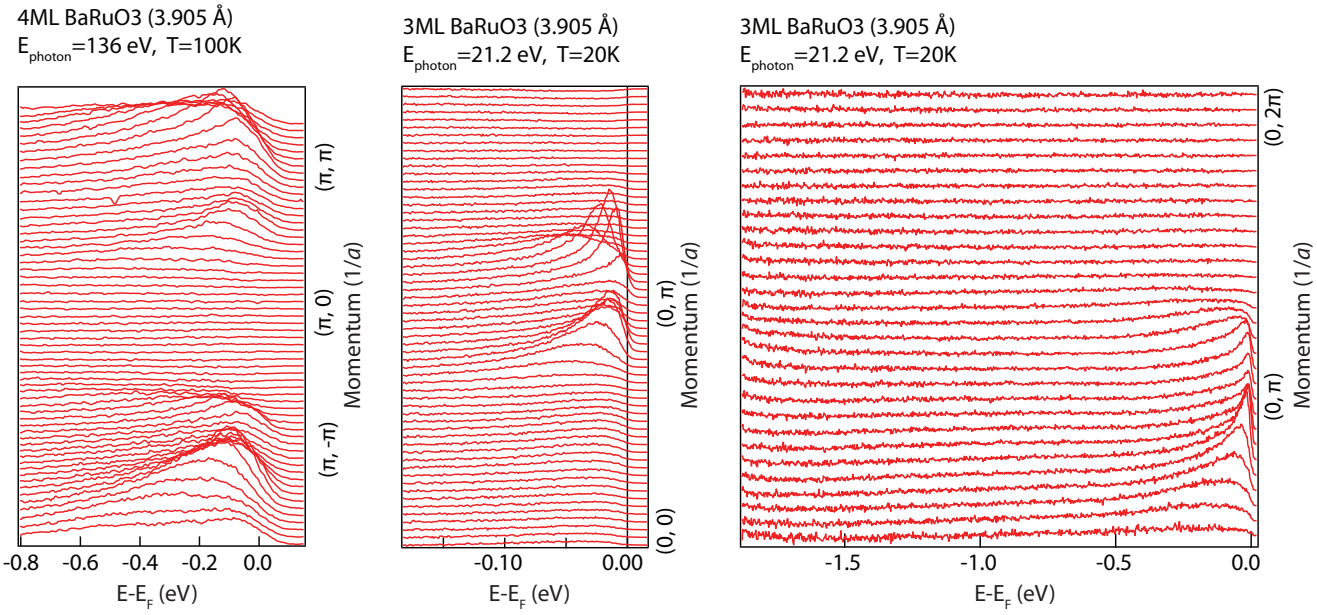

Figure 7.6: Quasiparticle spectra in $BaRuO_3$ films measured by ARPES.

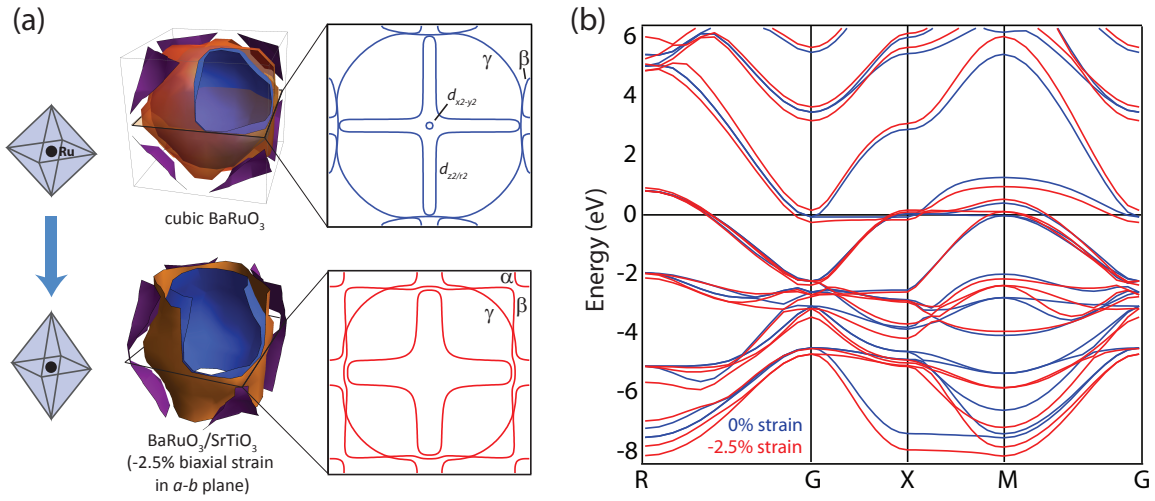

Figure 7.7: Theoretical Fermi surfaces (a) and band structure (b) calculated in GGA approximation to DFT for cubic and strained bulk $BaRuO_3$.

The calculated Fermi surface of nonmagnetic cubic $BaRuO_3$ consists two large sheets centered at $(k_x = 0, k_y = 0, k_z = 0)$ and smaller hole pockets centered at $(k_x = \pi, k_y = \pi, k_z = \pi)$. In addition to these FS sheets, DFT predicts additional Fermi surfaces arising from the $d_{x^2-y^2}$ and d_{z^2/r^2} e_g orbitals (Figure 7.7(a)). The thin films studied here are synthesized on $SrTiO_3$ substrates (a = 3.905 Å), and hence under a compressive strain of 2.5%, which increases the c-axis to 4.067 Å, as estimated by synchrotron x-ray diffraction measurements of the c-axis truncation rods. This in-plane compression elongates the apical Ru-O bond, thereby lifting the $d_{x^2-y^2}$ orbital entirely above E_F in the DFT calculations, due to the increased crystal field splitting. We should note that the change of the crystal symmetry from cubic to tetragonal does not increase the number of bands, since in both instances there remains only a single unique Ru atom per unit cell. Strain also drives the Lifshitz transition in the FS topology of the two electron-like pockets (Figure 7.7). The Fermi surface topology of the strained flims in the $k_z = 0$ plane bears strong resemblance to the electronic structure of the spin-triplet superconductor Sr_2RuO_4, hence we denote the two sheets centered at zone center as β and γ and the hole pocket we denote as α. We did not observe any e_g-derived FS pockets in experiment. The $d_{x^2-y^2}$ orbital is lifted above E_F due to changes in the crystal field, as mentioned above, and d_{z^2/r^2} is lifted due to quantization effects in the out-of-plane direction. Strain also has dramatic effect on the density of states at E_F, which will be discussed in the next chapter.

7.4 Electronic structure of the ultrathin films

In Figure 7.8(a-c) we show ARPES Fermi surfaces of $BaRuO_3$ films of varying thicknesses taken at 15 K with photon energy E_{ph} = 21.2 eV and 8 meV energy resolution. Qualitatively, the electronic structure is indeed simpler than that of $SrRuO_3$ ([153], Figure 8.2). Despite the greater simplicity of the electronic structure compared to $SrRuO_3$, we do observe additional

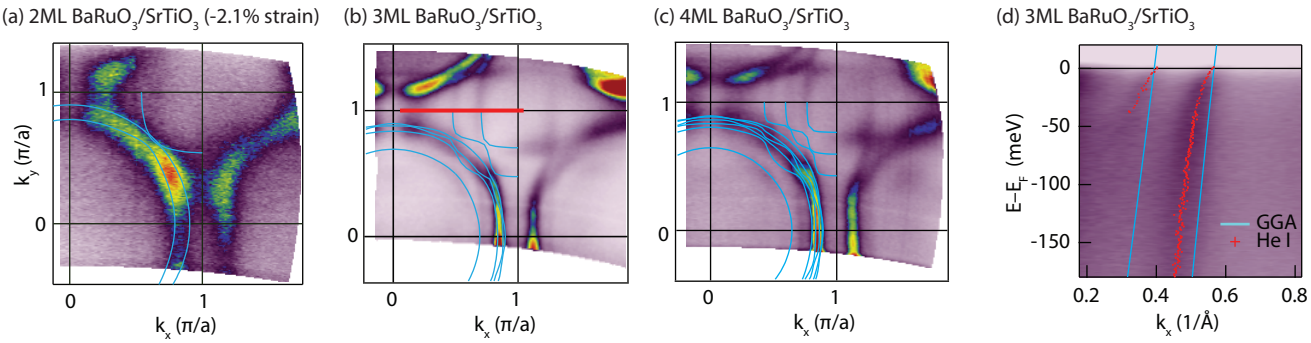

Figure 7.8: (a-c) ARPES Fermi surfaces of $BaRuO_3$ films of varying thicknesses. The calculated Fermi surfaces are shown as blue lines. The thicknesses of the 3 ML and 4 ML were derived from synchrotron XRD measurement. The 2 ML film thickness was estimated from the RHEED oscillations during growth. (d) Spectral line cut along red line in (b) shows two dispersive bands.

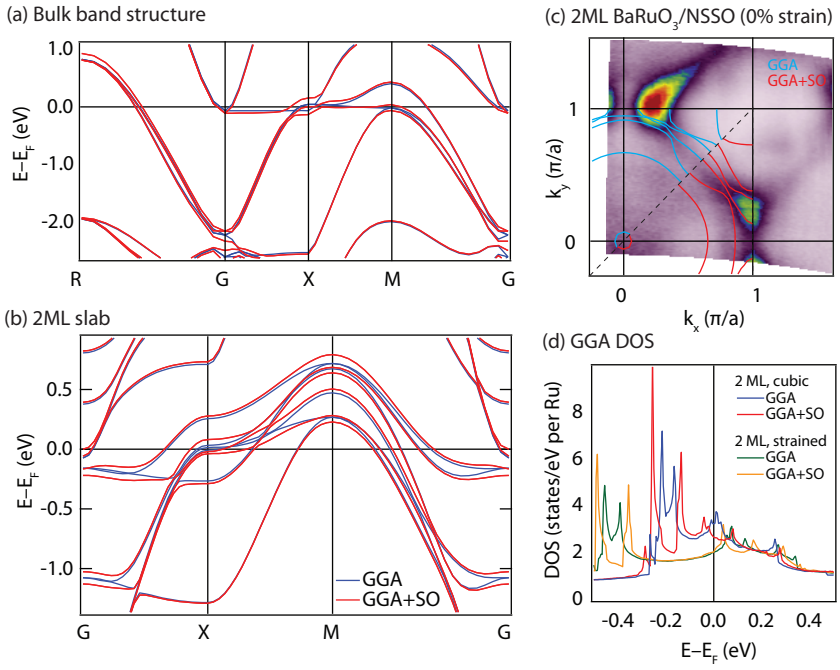

Figure 7.9: Effects of SOC on the band structure.

bands to what would be expected from the bulk calculation. These features are most evident around (π, π), in what appear to be additional replicas of the α-pocket; in the 3 u.c. sample, we see one additional band, in the 4 u.c. sample, we see two additional bands, and in the 2 u.c. sample we see no additional bands. There are a number of possible origins for such additional bands : 1) band doubling due to exchange splitting in a ferromagnetic sample, 2) band doublings due to a larger structural unit cell due to either surface reconstruction or octahedral tilting, and 3) sub-band formation due to quantum confinement in the out-of-plane direction, due to the atomically thin nature of the film. We can rule out the possibility of ferromagnetic exchange splitting, since the number of bands appears to scale with the film thickness, and furthermore, no signs of ferromagnetism can be observed in the bulk. On the same grounds, band doubling due to structural distortions can also be ruled out, due to the dependence on film thickness. We note that no signs of octahedral tilts (i.e. (0.5,0.5,0.5) Bragg peaks) can be observed in synchrotron diffraction, and while a surface reconstruction can be observed at some incident electron energies by LEED, the periodicity of the surface reconstruction does not depend on film thickness. This leaves quantum confinement in the out-of-plane direction forming quantum well states as the only possible origin for the extra observed bands.

Notably, the number of quantum well states observed experimentally for our films is always less by 1 than the number of atomic layers in contrast to the DFT prediction that dictates that these numbers should be equal (Figure 7.9(b)). A possible explanation for the discrepancy is that one monolayer in the film, either adjacent to the surface or the interface, is electronically inactive.

Finally, in Figure 7.9 we show the effect of the spin-orbit coupling (SOC) on the calculated band structure. SOC plays an important role for the band structure of superconducting Sr_2RuO_4 [119]. In bulk $BaRuO_3$ the apparent effect is much weaker and mainly removes the band crossing at BZ boundary near X points (Figure 7.9(a)). The effect is much more

pronounced in thin films: in addition to removing the band crossings, it causes a Lifshitz transition in one of the bands and a peak splitting in the density of states leading to reduction of the DOS at E_F (Figure 7.9(b, d)). The ARPES FS of the nominally unstrained film agrees well with the GGA+SO calculation.

7.5 Periodic spectral weight modulation of the quantum well states

To confirm that these extra bands arise from quantum confinement, we also performed photon energy dependent measurements of a 4 u.c. thick film protectively capped with a single unit cell of $SrTiO_3$ over a range of photon energies spanning from $\hbar\omega$ = 40 to 150 eV at the I4 beamline at the MAXLab synchrotron facility. These measurements were performed by Jason Kawasaki. Since these were ex-situ measurements, the following procedure was employed to prepare the samples. Immediately preceding the measurements, the capped sample was annealed at 425 C° under 2×10^{-5} torr of O_2 for 30 minutes in order to clean the surface. After the anneal the cleanliness of the sample was confirmed by the observation of a sharp 1x1 LEED pattern and no obvious contaminants in shallow cover levels. The sample was then transferred into analysis chamber (base pressure 1e-10 Torr). Measurements were performed at 100 K using a SPECS Phoibos analyzer.

In Figure 7.10, we show the intensity at E_F as a function of in-plane momentum k_y, and the out-of-plane momentum k_z by varying the photon energy. We see that the quantum well (QW) states do not exhibit a smooth k_z dispersion expected for a bulk sample, but rather, the individual QW sub-bands show no explicit k_z dependence, consistent with their two-dimensional nature. Despite their non-dispersive character, we nonetheless observe a periodic modulation of the sub-band intensity, shown in Figure 7.10(a), as a function of incident photon energy. The photon energy dependence has also been reported in ultrathin $SrVO_3$ [159]. We ascribe this intensity modulation as arising from the projection of the

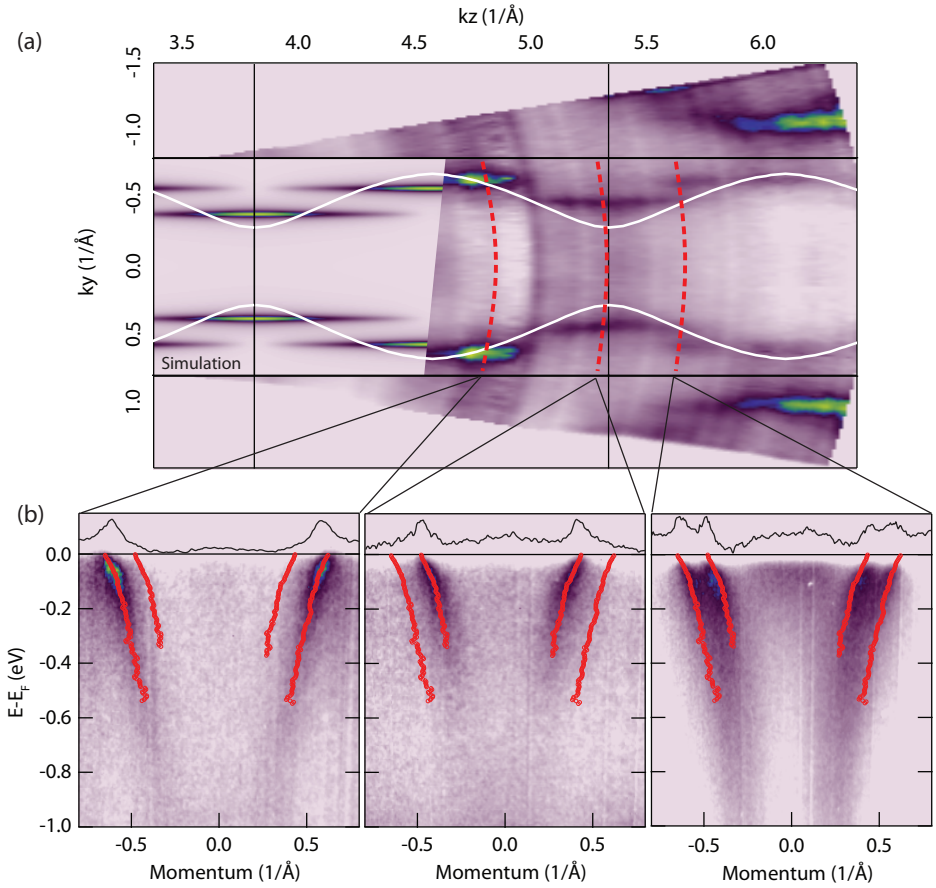

Figure 7.10: (a) ARPES Fermi surface map in $k_x = \pi/a$ plane, measured at the I4 beamline at the MAXLab synchrotron facility. The incident photon energy was varied to access different out-of-plane k_z momenta. The bands do not disperse along k_z, however, the spectral intensity has periodic modulations as a function of k_z. The intensity of the spectral weight follows the bulk band dispersion, show as solid white line. The simulated spectral weight map is overlaid on the experimental data. (b) ARPES spectra along k_y at $k_x = \pi/a$ at three different photon energies. The sub-band spectral weight depends on k_z whereas the dispersions $E(\mathbf{k})$ are identical at all k_z.

discrete QW states onto the bulk k_z quantum numbers. In Figure 7.10(a) we show the bulk k_z dispersion of the d_{yz}-derived band of the compressively strained $BaRuO_3$, obtained from GGA, together with the calculated QW sub-band spectral weights, overlaid on the experimental data.

This periodicity also allows us to more accurately ascertain the number of QW states. We discover that the number of QW states measured is consistently 1 unit cells less than the nominal thickness synthesized by MBE and measured by synchrotron x-ray diffraction. This suggests that there exists an electronically inactive or "dead" layer of 1 unit cells in the film. At this point, we can only speculate as to the origin or location of this electronically inactive layer, but the fact that we do not observe Fermi surface replicas at the periodicity of the reconstruction measured by LEED potentially indicates that the topmost unit cell may be electronically inactive (or at the very least, does not possess states at the Fermi level). At this point, it bears mentioning that both the substrate, $SrTiO_3$ and $BaRuO_3$ are nominally non-polar, and in principle should not suffer from the same issues regarding polar reconstruction of the surface or interface as many other perovskite oxides.

7.6 Transport in ultrathin limit

We now consider the effect of film thickness on transport properties. The resistivity as a function of temperature is shown in Figure 7.11(a) for the ultrathin films and the superlattices. All samples are metallic with the exception of 2 u.c. film and superlattices with 2.u.c. $BaRuO_3$ separated by 4 u.c. $BaTiO_3$. For comparison, thin films of $SrRuO_3$ reported in literature undergo a metal-insulator transition below 5 u.c. [149; 150]. The insulating behavior of our films could be driven either intrinsically by electronic ordering at low dimensions, or could be an effect if disorder due to low film quality. We look at the ARPES spectrum of the 2 u.c. sample to elucidate the most likely scenario. A spectral weight can clearly be observed at the

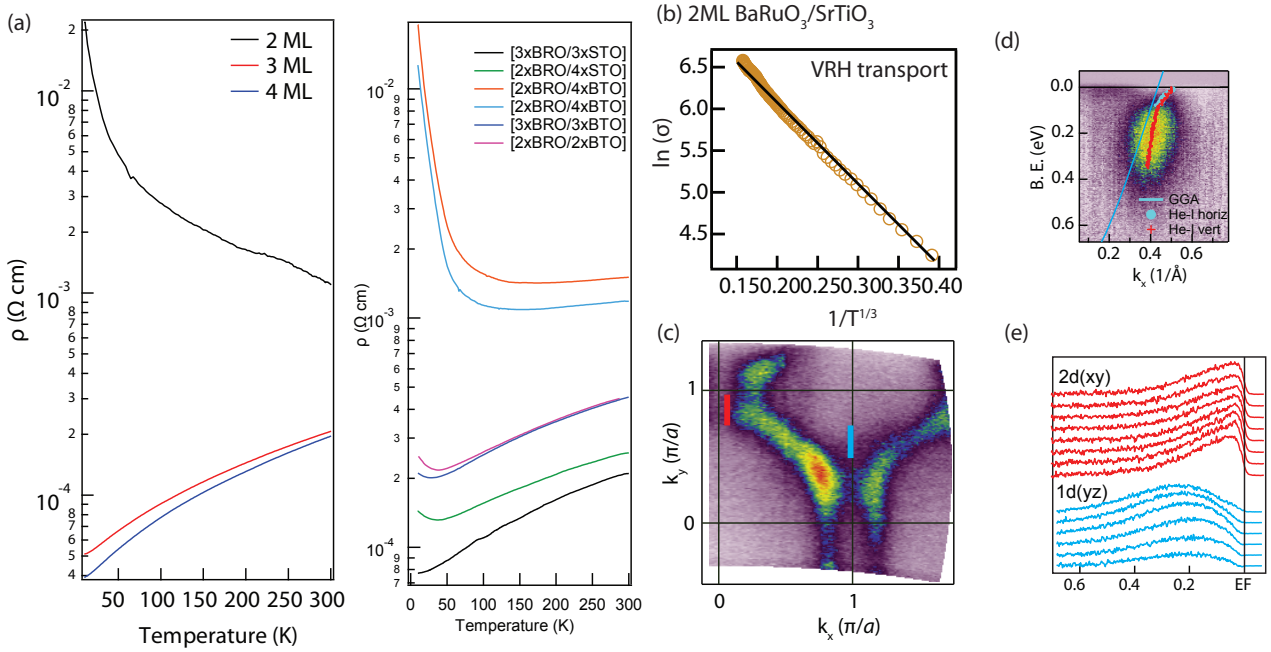

Figure 7.11: (a) Temperature dependence of resistivity in ultrathin films and superlattices of $BaRuO_3$. (b) Variable-range hopping transport behavior in the insulating 2 ML film. (c) ARPES Fermi surface of the 2 ML film. (d) ARPES line cut along the blue line in (c). (e) Energy distribution curves for 1D and 2D bands taken, respectively, along blue and red lines in (c).

Fermi level for this sample, moreover it is dispersing with a clear Fermi surface (Figure 7.11(c)). Notably, the energy distribution curves differ qualitatively for the 2D d_{xy}-derived and 1D d_{xz}-derived bands: the former shows a more sharp peak corresponding to coherent quasiparticles, whereas for the latter the weight is more suppressed at the Fermi level and transferred to higher binding energy (Figure 7.11(e)). In fact, the Fermi surface could not be observed for the 1D bands in Figure 7.11(c). This orbital selectivity of suppression of quasiparticle weight is most likely related to the dimensionality of the bands: for a given degree of disorder the carriers in the 1D band have stronger tendency to become localized than the ones in the 2D band, as the 1D hopping chains can be more easily disrupted by the same amount of disorder. The $R(T)$ dependence of the 2 u.c. film follows variable-range hopping behavior [160]. Observations by ARPES and transport measurements can be reconciled if we consider the disorder strong enough to suppresses any percolating path through the sample, but not strong enough to allow small conducting islands with barriers of different height between them. The insulating behavior at low temperature of the metallic superlattices follows weak localization form very well.

7.7 Conclusion

In conclusion, we employed epitaxial stabilization to synthesize ultrathin films of cubic perovskite $BaRuO_3$ and investigated their electronic and magnetic properties through a combination of x-ray and electron diffraction, electrical transport, and angle-resolved photoemission spectroscopy. We found that the atomically thin nature of these films (2-4 unit cells) gives rise to quantum confinement of the electronic structure into well-defined sub-bands. We observed that, consistently in all samples, out of N monolayers (ML) only $N-1$ contribute to the conduction band, which may indicate that one monolayer is intrinsically electronically inactive. The number of active electronic bands is further borne

out by observation of periodic modulation of ARPES spectral weight of the quantum well states as a function of out-of plane momentum. We further observed the orbital-dependent localization in the thinnest 2 ML film: ARPES spectral weight is suppressed at E_F and momentum-space line width is broadened for the 1D quantized bands, whereas the 2D band retains coherent quasiparticle weight at E_F. Our work demonstrates the possibility of utilizing quantum confinement in the atomically thin limit to engineer the density of states and control emergent ground states such as ferromagnetism in complex oxide thin films. The unprecedentedly high quality of these thin films (as evidenced by RRR) suggests $BaRuO_3$ as an ideal testbed for investigating the physics of the ruthenates as well as exploring the effects of quantum confinement on engineering emergent states in quantum materials.

CHAPTER 8

Suppression of ferromagnetism in ultrathin $BaRuO_3$

8.1 Magnetic state in ultrathin $BaRuO_3$

The transition to ferromagnetic state in $SrRuO_3$ on cooling manifests in the transport properties as a prominent kink at T_C = 160 K. Figure 7.4(a) shows the $R(T)$ dependence in thin films of $SrRuO_3$ grown on $NdGaO_3$ substrate [153]. The resistivity curve is also characterized by the change in the second derivative d^2R/dT^2, separating the two transport regimes of conduction electrons interacting with ordered and disordered moments. This coherence-incoherence crossover has been observed in many heavy-fermion systems at the Kondo energy scale, where conduction electrons form transition metal d-band scatter off local f-shell moments. Observation of the crossover in $CaRuO_3$ (but without a well-defined kink) is in agreement with the presence of local moments in this compound.

In stark contrast to $SrRuO_3$ flims, the resistivity curve of the ultra-thin $BaRuO_3$ films does not have a kink, nor the change in the transport regime (figure 7.4(b)). As discussed in the previous chapter, the measured Fermi surface matches well with the non-magnetic calculation, in which the occupations of spin-up and spin-down bands are equal, and thus the net spin moment in the conduction band is zero. These two observations suggest that the ferromagnetism is suppressed in the ultra-thin $BaRuO_3$ thin films in favor of paramagnetic metallic state with zero spin moment, in contrast to the paramagnetic states in $CaRuO_3$ or $SrRuO_3$ at $T > T_C$ with disordered local moments. In the low-temperature limit, the

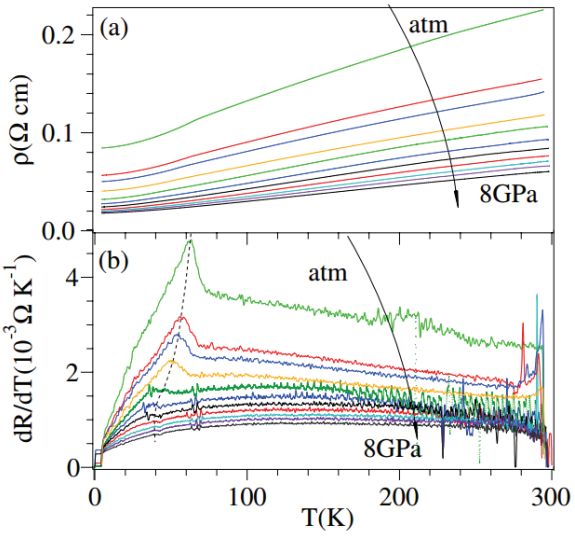

Figure 8.1: Temperature dependence of resistivity of bulk $BaRuO_3$ under different pressures from ambient pressure to 8 GPa. Reproduced from [155].

resistivity in $BaRuO_3$ quantum wells follows the power-law $\rho \sim T^{1.4}$ rather than $\rho \sim T^{2.0}$ expected for the Fermi liquid and observed in $SrRuO_3$ (figure 8.2(b)). This likely suggests the presence of critical fluctuations in $BaRuO_3$ near the ferromagnetic quantum phase transition. The low-temperature power law and the overall $R(T)$ behavior in the ultra-thin films of $BaRuO_3$ are the same as in bulk $BaRuO_3$ under hydrostatic pressure (figure 8.1) [155]. The hydrostatic pressure was found to suppress the T_C and enhance the critical fluctuations as measured in the low-temperature resistivity power-law and critical exponents of magnetic isotherms near transition. Thus, cubic $BaRuO_3$ might be intrinsically close to the FM phase boundary and the quantum phase transition can be driven by dimensionality or pressure.

The dimensionality-driven suppression of ferromagnetism is not unique to $BaRuO_3$, it has been previously observed in $SrRuO_3$ films by varying film thickness in two works [149; 150]. The mechanism of suppression is, however, inconclusive as in both reports the reduction of T_C with decreasing film thickness was accompanied by the metal-insulator transition, which may be due to, for example, increased crystal defect density near the film-substrate interface. On the contrary, the $BaRuO_3$ films discussed here remain metallic

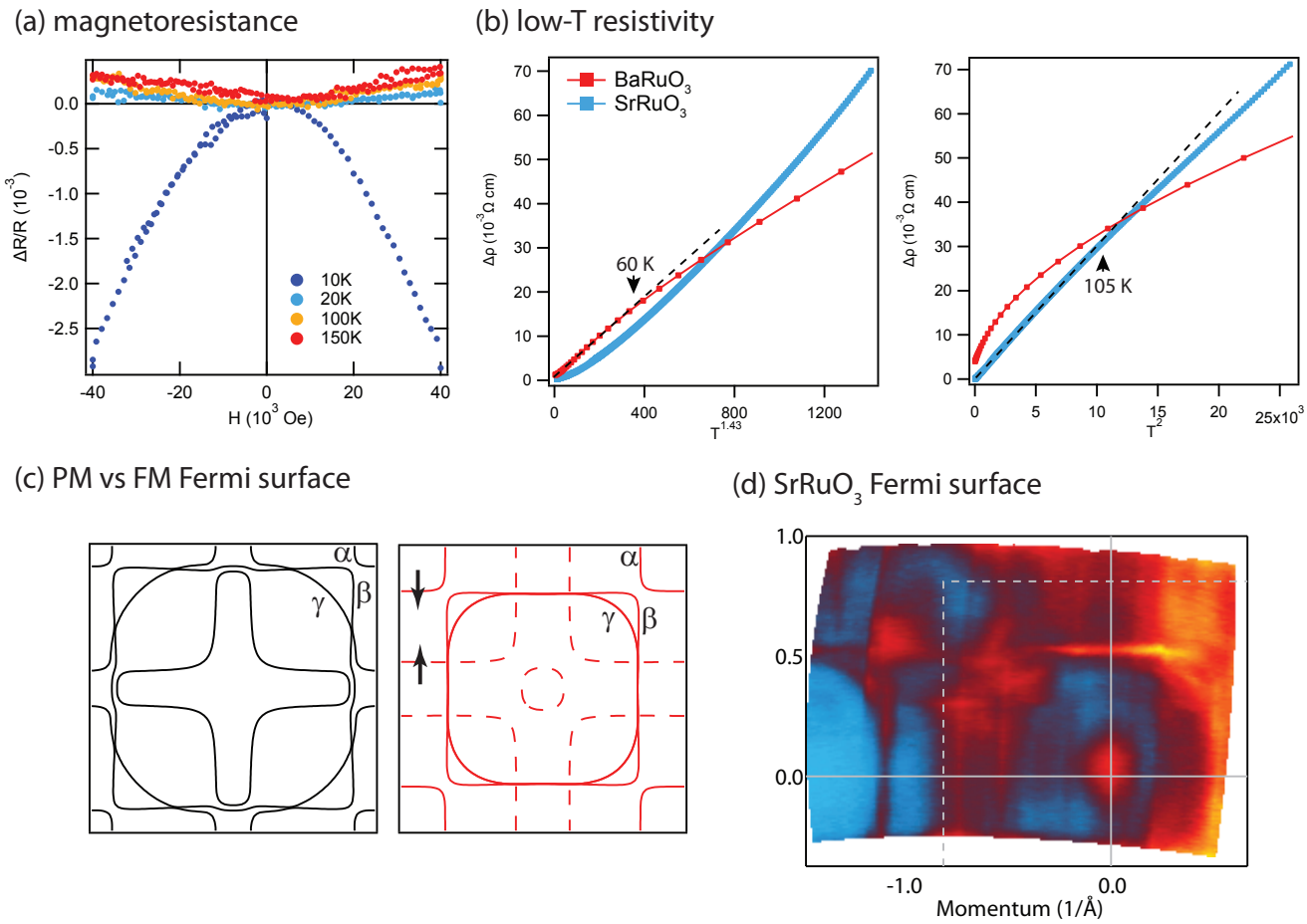

Figure 8.2: (a) Magnetoresistance of the 3 u.c. $BaRuO_3$ film. The sign of MR changes to negative on cooling below 20 K. (b) Low-temperature resistivity exponents in $SrRuO_3$ and $BaRuO_3$ thin films. (c) Ferromagnetic and paramagnetic Fermi surfaces of a model cubic perovskite ruthenate from DFT. (d) ARPES Fermi surface of $SrRuO_3$, reproduced from [153].

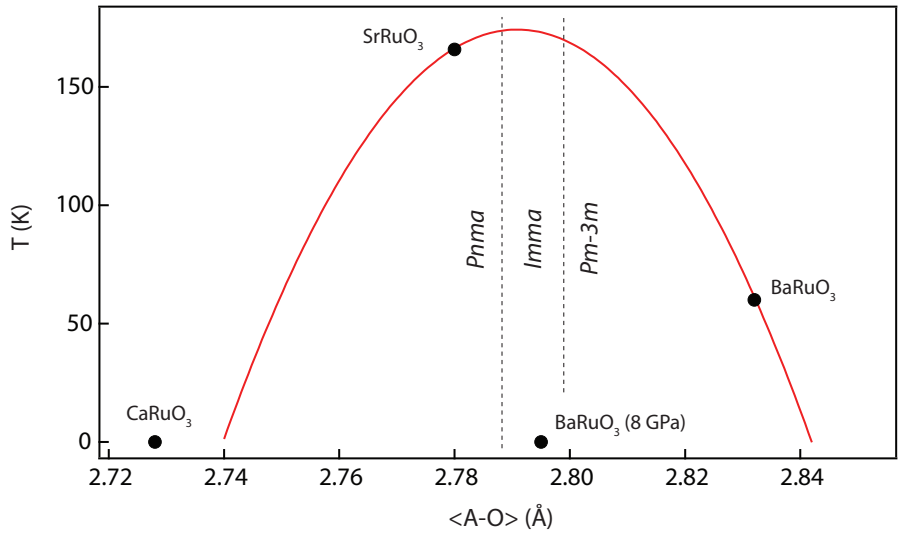

Figure 8.3: The phase diagram of T_C versus the mean A-O bond length, adapted from [166].

down to 3 u.c. thickness with residual resistivity ratios in the $4-7$ range. Thus, sample quality degradation can be ruled out as the primary driver of the transition. The suppression of an ordered state in the limit of two-dimensional thin films could also be understood from the Mermin-Wagner-Hohenberg theorem stating that continuous symmetries cannot be spontaneously broken at finite temperature in the systems with finite-range interactions in dimensions $d \leq 2$ [161; 162]. In the real systems, however, the assumptions of continuous symmetry and dimensionality $d = 2$ do not always hold, e.g. in cases of interfacial 2D ferromagnetism [163–165]. Finally, the suppression of T_C in thin films of metallic ferromagnets has been observed and attributed to the reduced density of states at the Fermi level and decrease in the average exchange energy.

8.2 Trends in ferromagnetic T_C in perovskite ruthenates

Since bulk ferromagnetic $BaRuO_3$ was synthesized only relatively recently [155; 156], it will be helpful to compare its magnetic properties to those of the much more explored Sr and Ca

counterparts. $SrRuO_3$ is ferromagnetic with Curie temperature T_C = 160 K in bulk [42; 167] and unstrained films [168]. It is a moderately correlated metal [153; 169; 170], and its magnetism, that originates from Ru-d orbitals, exhibits both itinerant and local-moment signatures. The measured moment above T_C is $2\mu_B$, implying low-spin state of the four electrons in the ruthenium d-shell in the local orbital picture. The low-temperature saturation moment is $1.4\mu_B$. Density functional theory (DFT) calculations predict a similar moment and show strong O $2p$ - Ru $4d$ hybridization [169; 171]. The ratio of the high-temperature to low-temperature moment of ≈ 1.3, is indicative of strong-itinerant ferromagnetism, i.e. with local moments, similar to elemental magnets like nickel and cobalt [172]. On the other hand, the linear magnetic isotherms (M^2 versus H/M, i.e. Arrott plots [173; 174]) in the vicinity of T_C are characteristic of mean-field universality class [175], similar to weak-itinerant ferromagnet $ZrZn_2$ and in contrast to most known metallic ferromagnets that show significant critical fluctuations near T_C. Epitaxial strain in films can have reduces the T_C to 150 K [47] and has dramatic effect on the critical fluctuations near T_C [176]. Ca doping on the A-site lowers the T_C of the compound and the end-member $CaRuO_3$ shows no magnetic ordering. According to DFT calculations, $CaRuO_3$ has lower Fermi-level density of states due to enhanced octahedral rotations and larger splitting of the van Hove singularities [177], leading to suppressed ferromagnetism in agreement with observations. This picture of band magnetism driven by density of states at E_F breaks down for $BaRuO_3$: van Hove singularity in the cubic $BaRuO_3$ is located almost exactly at the Fermi level, thus the higher DOS at E_F is expected to favor higher T_C than in Sr compound [177; 178]. On the contrary, the T_C of 60 K in bulk $BaRuO_3$ is not only lower, but this compound is close to the the ferromagnetic phase boundary, and can be driven e.g. by application of pressure [155], as discussed above.

Figure 8.3, adapted from [166], shows dependence of the ferromagnetic transition temperature on the average <A-O> bond length, measured for series of $Ca_xSr_yBa_{1-x-y}RuO_3$ compounds. The three compounds are placed on the graph. T_C versus <A-O> bond length

follows a parabolic curve, with maximum occurring in the orthorhombic *Imma* phase for tolerance factor t = <A-O>/($\sqrt{2}$<Ru-O>) ~ 1, i.e. near equilibrium Ru-O bond length. On the left side, stronger covalent competition between the A-O bond and the B-O bond for O-2p electron in the distorted structure lowers the T_C, while on the right side, increased bandwidth of the undistorted cubic structure lowers T_C in an itinerant ferromagnet. This lattice strain effect, however, still fails to explain the pressure dependence of T_C in $BaRuO_3$, as the trivial effect of increased bandwidth on the density of states is too small to completely suppress the ferromagnetism (DOS in $BaRuO_3$ under pressure is still larger than in $SrRuO_3$).

These trends in the T_C in the Ba-, Sr- and $CaRuO_3$ were analyzed in recent density functional plus dynamic mean-field theory (DFT+DMFT) studies [179; 180]. The correct phases were reproduced when considering only t_{2g}-derived bands with some particular values of Coloumb and Hund's rule interactions. Three major factors were found to control ferromagnetic T_C: DOS at E_F, skew in the DOS shape (position of the band edge w.r.t the peak), and the bandwidth. The e_g bands are removed from the Fermi level in $SrRuO_3$ (figure 8.4(c)), but their inclusion was necessary in [179] to get a realistic value of magnetic moment of $1.65\mu_B$, instead of the low-spin state value of $2\mu_B$ obtained when only t_{2g} states were included. The reduced T_C in $BaRuO_3$ compared to $SrRuO_3$ was attributed to the skew in the DOS. Quite remarkably, the many-body physics in the t_{2g} bands with two interaction parameters U and J_H capture the essential differences of magnetism between the three compounds.

However, the strong suppression of T_C in $BaRuO_3$ under pressure does not seem to follow the same trends. From table 8.1, that lists some details of crystal and electronic structure, and figure 8.4 it is apparent that application of hydrostatic pressure to $BaRuO_3$ causes negligible change in the DOS skew and only a small change in the DOS at E_F; the e_g states are removed from the E_F, which is expected to favor a higher saturation moment. To calculate the electronic structure of $BaRuO_3$ under 8 GPa hydrostatic pressure a theoretical value of bulk

	space gr.	<A-O>	<Ru-O>	W	$N(E_F)$	n	$M_{T=0}$	T_C (K)
$CaRuO_3$	*Pbnm*	2.728 [181]	1.992 [181]	2.6 [180]	–	1.5	0	–
$SrRuO_3$	*Pbnm*	2.780 [182]	1.984 [182]	2.8*	6.1*	2.0	1.4	160
$BaRuO_3$	*Pm-3m*	2.832 [156]	2.003 [156]	3.1*	7.6*	1.85	0.9	60
$BaRuO_3$(8 GPa)	*Pm-3m*	2.795*	1.976*	3.3*	7.1*	1.4	0 [155]	– [155]
$BaRuO_3/SrTiO_3$	*P4/mmm*	–	–	2.6*	6.7*	1.4	–	–

Table 8.1: Average bond lengths <A-O> and <Ru-O> (Å), bandwidth W (eV), density of states at Fermi level $N(E_F)$ (eV^{-1}), low-temperature power-law of resistivity n, zero temperature magnetization $M_{T=0}$ (μ_B), and transition temperature T_C (K) in perovskite ruthenates.

modulus K = 206.4 GPa [158] was used. The lattice parameter corresponding to P = 8 GPa is then $a_{8\ \mathrm{GPa}}$ = 3.9535 Å, i.e. decrease by 1.3% from the bulk value.

The quantity that correlates most strongly with the reduction of T_C and increase in critical fluctuations when going from $SrRuO_3$ to $BaRuO_3$ to $BaRuO_3$ at 8 GPa, is the bandwidth W. In the following discussion we will discuss a simple model that shows how the increase in the bandwidth can lead to reduced ferromagnetism and increase in quantum fluctuations, by considering how Hund's rule interaction affects the hopping dynamics of electrons on the short-range scale. Specifically, we will argue that electrons can reduce their energy via kinetic energy term more effectively by occupying the singlet state on Ru sites compared to the triplet state.

8.3 Bandwidth-driven suppression of ferromagnetism

Ferromagnetism in transition metals has traditionally been approached from two opposite perspectives: the local moment magnetism and itinerant model. This stems from the dual character of transition metal *d*-electrons: they form the conduction band described by the band theory in their ground state, and at the same time show properties of local moments, for example, obey the Curie-Weiss law of magnetic susceptibility [183]. In the local moment

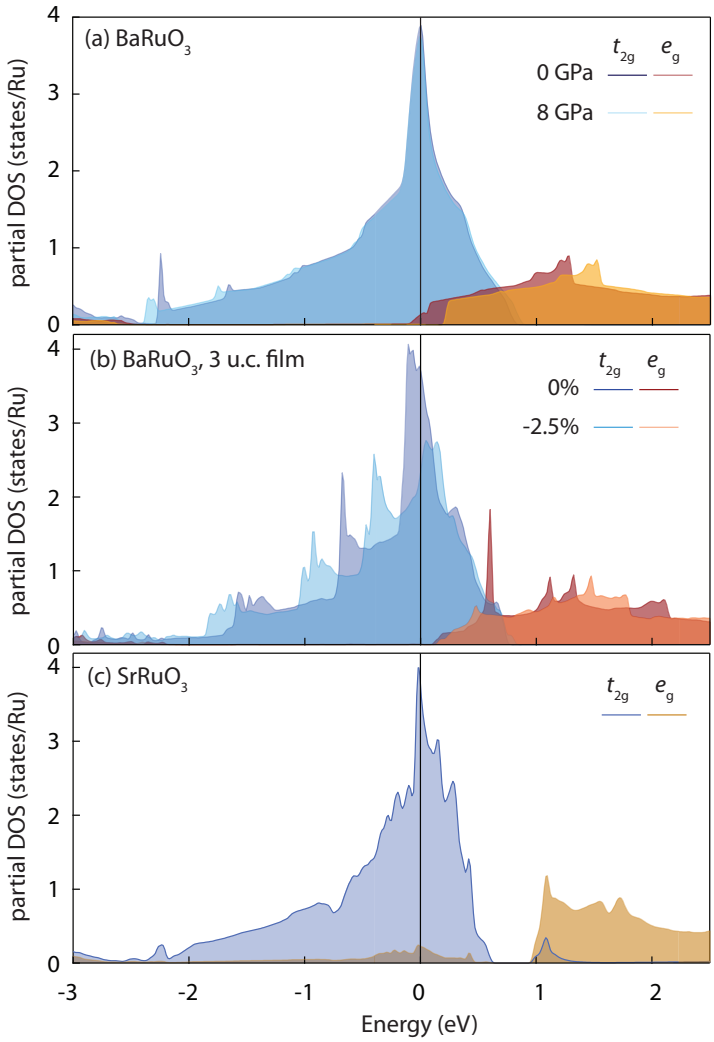

Figure 8.4: The partial density of states calculated in DFT for $BaRuO_3$ cubic bulk and under 8 GPa hydrostatic pressure (top), ultrathin films under 0% and 2.5% compressive strain (middle), and (c) bulk $SrRuO_3$ (bottom).

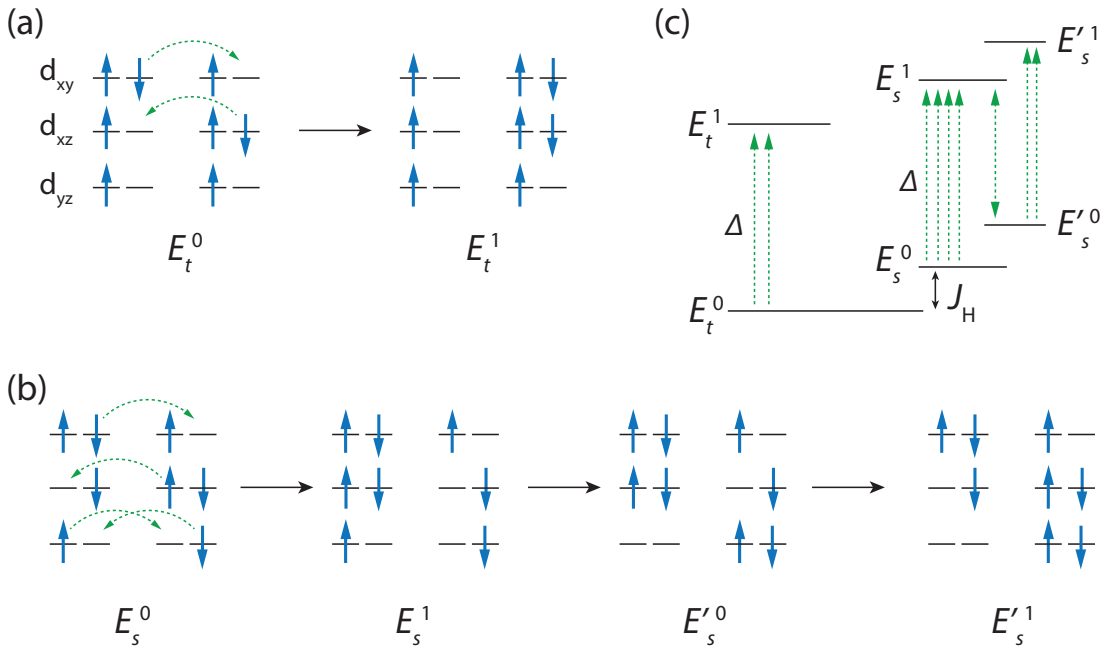

Figure 8.5: Energy levels in two-site system in triplet and singlet configurations.

picture, the fixed-sized atomic magnetic moments are placed in external magnetic field H directed along z-axis. The natural thermal excitations of this system are rotations of the local magnetic moments. Langevin was first to calculate the average magnetization at temperature T [184] in the lowest order in H: $\langle m_z \rangle \propto H/k_B T$, from which the Curie law $\chi \propto C/T$ follows. When the interaction between the moments is included, the magnetic susceptibility follows the Curie-Weiss (CW) law: $\chi = C/(T - T_C)$, where transition temperature T_C depends on the interaction strength [185]. The success of the local moment picture was based on the fact that almost all known ferromagnets obey the CW law.

In the itinerant electron theory of ferromagnetism, the electron in transition-metal d-bands interact via wave-vector-independent molecular field, quantified by intra-atomic exchange energy constant I. Magnetic moment in units of $2\mu_B$ is $M = \frac{1}{2}(N_\downarrow - N_\uparrow)$, where N_σ is the number of electrons with spin σ. The exchange energy is given by

$$E_{exch} = \frac{1}{4} I N^2 - I M^2.$$

Exchange energy favors ferromagnetism, $M \neq 0$, or $N_\downarrow \neq N_\uparrow$, but it is opposed by increase in kinetic energy. The total energy is given by $E = (1 - I\rho)M^2/\rho + ...$, where ρ is the density of states at the Fermi level. Thus ferromagnetic state is energetically favorable for

$$I\rho(\epsilon_F) > 1,$$

which is known as the Stoner criterion. The itinerant magnetism predicts exchange-split bands near the Fermi level and non-integer values of magnetization per atom (in μ_B units), both of which were observed in transition metals (see e.g. [186]). The extension of the Stoner theory to finite temperature was less successful, since the CW susceptibility could not be explained, and the calculated T_C values are too small [183]. The thermal excitations in the Stoner theory are spin flip excitations across the Fermi surface (or excitations of electron-hole pairs with opposite spins) that produce spatial modulation of spin-density in the crystal. After the development of the self-consistent renormalization theory of spin-fluctuations [187] the CW susceptibility was finally explained within the itinerant picture. In the Stoner theory only one band is considered. Recent works on the multiorbital systems on two- and three-dimensional cubic lattices [188; 189] showed the importance of Hund's rule coupling J_H in forcing the ferromagnetic ground state in limiting case of infinite U. We consider how the inter-orbital interaction affects the hopping dynamics of the electrons in the singlet and triplet states respectively. Starting with the spin-triplet state in in $SrRuO_3$, that agrees with observed local moments as well as DMFT calculations, we show that increase in hopping parameter leads to the singlet state becoming energetically more favorable.

We first consider a two-site system, shown on Figure 8.5, with three t_{2g} orbitals and four electrons per site. According to Hund's rule coupling, triplet configuration at each site has the lowest energy E_0^t (Figure 8.5(a)). The energy of a singlet configuration E_0^s shown in Figure 8.5(b) is higher by J_H per site: $E_s^0 = E_t^0 + 2J_H$. The excited states E_1^t and E_1^s are available via hopping. Assuming that hopping is allowed when the orbital state and spin are conserved, there are four non-zero matrix elements between the ground state and excited states for

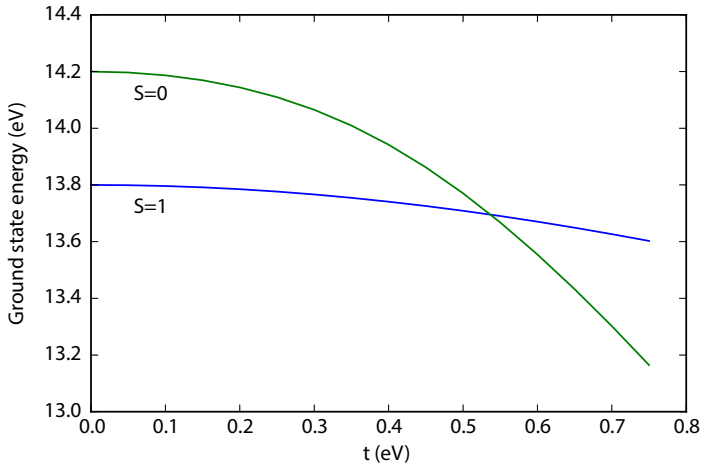

Figure 8.6: Energy levels in two-site system in triplet and singlet configurations.

the singlet configuration and two non-zero matrix elements for the triplet state shown schematically in Figure 8.5. In the limit of strong local interactions and small hopping, the second-order perturbation theory gives the following corrections to the ground-state energy:

$$E_n^{(2)} = E_n^{(0)} + \sum_{m \neq n} \frac{| < \psi_m^0 | H' | \psi_n^0 > |^2}{E_n^0 - E_m^0}$$

The corrections for the triplet and singlet state energies are given by:

$$E_t^{(2)} = E_t^0 - \frac{2t^2}{\Delta}$$

$$E_s^{(2)} = E_s^0 - \frac{4t^2}{\Delta} = E_t^0 + 2J_H - \frac{4t^2}{\Delta}$$

Hence, the singlet state becomes favorable at $t > \sqrt{J_H \Delta}$.

To put this on more formal grounds, and verify the solution for large values of t, we solve the problem exactly on a small cluster by diagonalizing the effective Hamiltonian

$$H = H_{\text{kin}} + H_{\text{onsite}}$$

In the following we limit the hopping to be nearest neighbor:

$$H_{\text{kin}} = -\sum_{i\sigma\alpha, j\sigma'\beta} t_{i\sigma\alpha, j\sigma'\beta} c^\dagger_{j\sigma'\beta} c_{i\sigma\alpha} = -t \sum_i \sum_{<i,j>} c^\dagger_j c_i \delta_{\sigma,\sigma'} \delta_{\alpha,\beta}$$

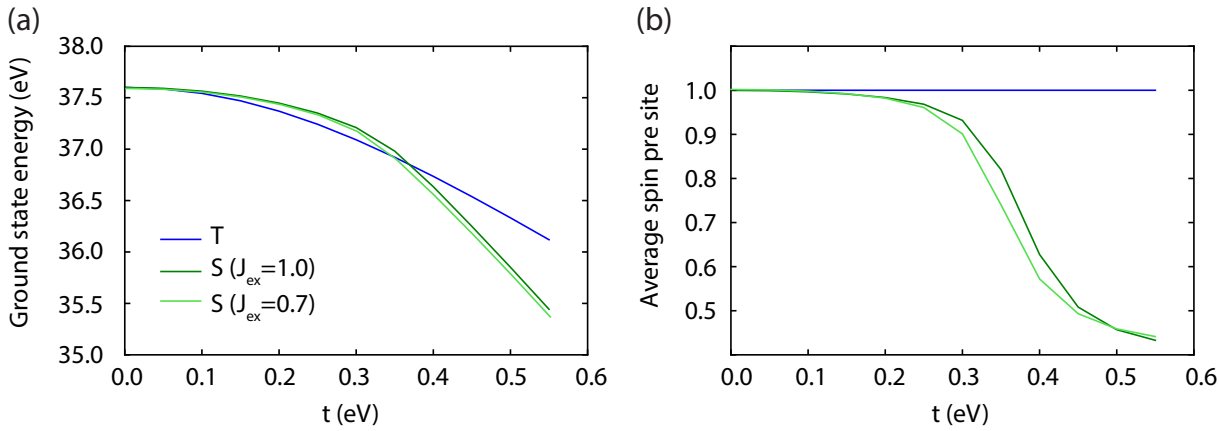

Figure 8.7: Energy levels in four-site system and transition between triplet and singlet states.

The onsite interaction is taken to have rotationally invariant Slater-Kanamori form[40; 190], as is usual in studies of transition metal oxides:

$$H_{\text{onsite}} = U \sum_{\alpha} n_{\alpha\uparrow} n_{\alpha\downarrow} + (U - 2J) \sum_{\alpha \neq \beta} n_{\alpha\uparrow} n_{\beta\downarrow} +$$

$$+(U - 3J) \sum_{\alpha > \beta, \sigma} n_{\alpha\sigma} n_{\beta\sigma} + J \sum_{\alpha \neq \beta} (c^{\dagger}_{\alpha\uparrow} c^{\dagger}_{\beta\downarrow} c_{\alpha\downarrow} c_{\beta\uparrow} + c^{\dagger}_{\alpha\uparrow} c^{\dagger}_{\alpha\downarrow} c_{\beta\downarrow} c_{\beta\uparrow}),$$

Figure 8.6 shows the ground state energies for triplet and singlet configurations shown in Figure 8.5 (see Appendix for the details of the calculation). There is no transition between the two configurations in this system due to number of electrons in each orbital. The triplet state is favored for small t and singlet state becomes more favorable at $t \approx 0.55$ eV.

We next consider a four-site cluster, shown schematically in figure 8.7(a). Here, transition between the singlet and triplet states (both FM and AFM) are allowed for the same spin and orbital occupation configurations. In an infinite crystal, the high density of states at the Fermi level can lead to the ferromagnetic state via Stoner instability, i.e. the Stoner mechanism provides effective ferromagnetic coupling. Since these band-structure effects are completely ignored in a small cluster we add the ferromagnetic coupling via Heisenberg term $-J_{ex} \sum_{<ij>} S_i S_j$, where the interaction is allowed between the nearest neighbors and

$J_{ex} > 0$ corresponds to the FM coupling. Figure 8.7(b-d) shows the average spin per site, the ground-state energy and average spin correlation between the nearest neighbors. As can be seen from Figure 8.7, at low t the average spin per site is $S = 1$, and the system spends all time in the triplet state with ferromagnetic alignment between the sites. The double-exchange-like mechanism favors FM, in agreement with previous study [191]. However, at higher values of t there is more contribution from the singlet states to the ground state, and local sites fluctuate between singlet and triplet states. At high values of t PM state with strong fluctuations arises as there not enough neighbors in the triplet state to make an ordered state. The crossover in the case of the four-site model occurs at $t \approx 0.3 - 0.4$ eV. When the coupling between the sites is reduced, the crossover occurs at a lower value of t. This might give an intuitive explanation to the thickness-driven suppression of ferromagnetic state at a constant value of t in the ultra thin films, in which the average number of nearest neighbors and the correspondingly the average exchange energy per site are reduced, when film thickness is reduced.

8.4 Conclusion

Finally, we estimate the effect of the Hund rule coupling on the average number of available nearest-neighbor hopping matrix elements per site in the bulk crystal for the triplet-FM and singlet configurations. Again, we consider the hopping part of Hamiltonian with only nearest-neighbor hopping to keep the analysis simple:

$$H_{\text{kin}} = -\sum_{i\sigma\alpha,j\sigma'\beta} t_{i\sigma\alpha,j\sigma'\beta} c^{\dagger}_{j\sigma'\beta} c_{i\sigma\alpha} = -t \sum_{i} \sum_{<i,j>} c^{\dagger}_{j} c_{i} \delta_{\sigma,\sigma'} \delta_{\alpha,\beta}$$

The average number of nearest-neighbor hopping matrix elements per site in the triplet state is given by

$$N_{nn,t} = \frac{1}{N_t^2} \sum_{\sigma\alpha\in C_t} \sum_{\sigma'\beta\in C_t} \sum_{<i,j>} \delta_{\alpha,\beta} \delta_{\sigma,\sigma'} n_{i\alpha\sigma} (1 - n_{j,\beta,\sigma'})$$

where the summation is done over all triplet configurations C_t for the given majority spin, $N_t = 3$ is number of such configurations per site. The result in three dimensional case is $N_{nn,t}^{(3D)} = 8/3$ for the triplet state. For the singlet state, there are $N_s = 9$ possible configurations per site, and a similar calculation of number of hopping matrix elements gives $N_{nn,s}^{(3D)} = 16/3$. For the case of two dimensions we get $N_{nn,t}^{(2D)} = 16/9$ and $N_{nn,s}^{(2D)} = 32/9$, respectively. Thus in both $d = 2$ and $d = 3$, the number of available hopping matrix elements is doubled in the singlet state relative to the triplet state.

CHAPTER 9

Conclusions and Outlook

In this dissertation we presented the original research on electronic properties of perosvskite-based ruthenates. We discussed the first *k*-resolved electronic structure of Ba_2RuO_4 and $BaRuO_3$ and explored their detailed response to the effects of structural engineering.

Our measurements clearly established the strong response of the quasiparticle properties to the structural tuning parameters. We reveal a topological transition in the γ-band of A_2RuO_4 when the Ru-O bond distance is increased and the van Hove singularity traverses the Fermi level. By deliberately choosing the substrates we were able to synthesize samples with the vHs tuned closely to the Fermi energy. In this sample, we clearly observe signatures of critical fluctuations in transport measurements and a characteristic band flattening in ARPES spectra. We find that the quasiparticle mass enhancements increase as a function of strain and A-site cation monotonically and are not peaked at the Lifshitz transition as suggested by previous studies. We have fully parametrized the low-energy quasiparticle dispersion as a function of biaxial strain in Ba_2RuO_4 and Sr_2RuO_4 which could provide input for the theoretical predictions for enhancing the superconductivity.

Additionally, we have synthesized the first thin films of cubic polymorph of $BaRuO_3$ and mapped its electronic structure. Cubic $BaRuO_3$ is a model system that is free of octahedral rotations, which complicate the interpretation of the experimental band structure and the origin of magnetism in $SrRuO_3$. We presented the detailed mapping and interpretation of its spectral function. By synthesizing films with thicknesses of 3, 4, and 5 monolayers, we reveal

quantum well states with modulated spectral weight as a function of effective out-of-plane momentum. We propose the origin of such modulations. We find that the $BaRuO_3$ in ultra thin limit is a paramagnet displaying signatures of critical fluctuations in transport. Its Fermi surface is unpolarized in stark contrast to the ferromagnetic $SrRuO_3$ films. We observe a "clean" suppression of ferromagnetism by dimensional confinement that is not accompanied by the metal-insulator transition in contrast to the reports on $SrRuO_3$. The resistivity as a function of temperature has metallic character and residual resistivity ratio of ~ 7 even for the thinnest measured films. There is a single transport regime between 4 K and the room temperature, in contrast to all bulk pseudo-cubic perovskite ruthenates, which exhibit either kinks or inflection points.

There are a number of research projects that could be motivated by the current study. Given the success in synthesizing ultra thin metallic $BaRuO_3$, the next step could be to perform similar measurements on ultra thin $SrRuO_3$. The feasible explanations of the previously reported thickness-driven metal insulator transition accompanying the suppression of ferromagnetism include 1) localization driven by dimensionality, 2) MIT driven by stronger octahedral rotations in the few atomic layers, 3) disorder-driven localization due to the lower crystalline quality in the atomic layers adjacent to the substrate. Growth of high quality samples in the present chamber could help unveil this problem.

An experiment that could further elucidate the evolution of ferromagnetism in $BaRuO_3$ under pressure is studying the films in tensile strain. It has been demonstrated in two reports that $Sr_3Ru_2O_7$ undergoes paramagnetic to ferromagnetic transition under uniaxial pressure along the out-of-plane direction. This is particularly interesting, since this shows that ferromagnetism can, in principle, exist in electronic system consisting of only two ruthenate layers. Again, the possible mechanism here could be reduction of octahedral rotation angle about the *c*-axis due to increase in the in-plane lattice parameter. Another possibility could be the change of the in-plane hopping integrals, i.e. the effect opposite to the one

hypothesized in this thesis for the bulk $BaRuO_3$ under hydrostatic pressure (where seemingly the major change is the increase of hopping values). Studying $BaRuO_3$ under tensile strain could also help elucidate the role of the e_g-derived bands, since the bottom of the $d_{x^2-y^2}$-derived band is expected to become occupied.

Appendices

APPENDIX A

Structural parameters of strained Sr_2RuO_4 and Ba_2RuO_4

In the table below we provide the calculated structural parameters for the biaxially strained Sr_2RuO_4 and Ba_2RuO_4, and Sr_2RuO_4 under hydrostatic pressure. Electronic structure calculations were performed using density functional theory in the local density approximation (LDA) and generalized gradient approximation (GGA - PBESol), as implemented in Wien2k and VASP [192; 193]. In the calculations for a given substrate, the in-plane lattice constant was fixed and the out-of-plane lattice constant and the internal degrees of freedom were relaxed. Our calculations were performed with a 17x17x17 k-point sampling of the Brillouin zone.

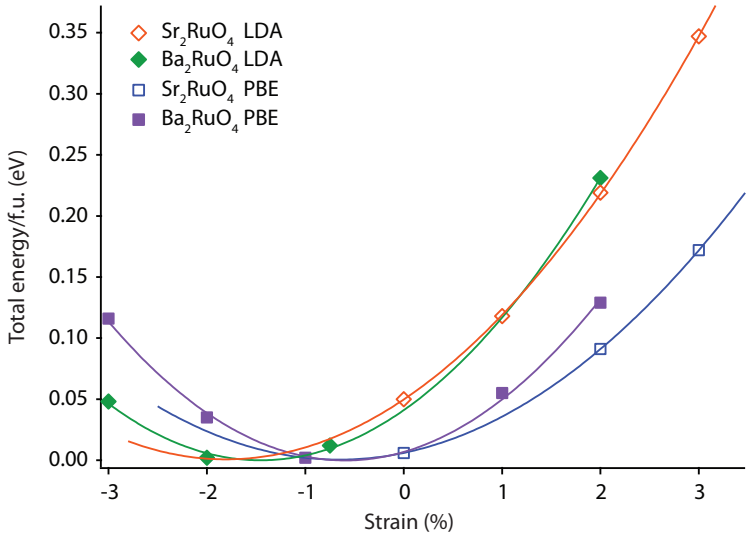

Figure A.1: Total energy of Sr_2RuO_4 and Ba_2RuO_4 calculated with LDA and GGA-PBE exchange correlation potentials for different strain states.

strain (%)	a (fixed)	c	z_{Sr}	z_{O1}	Ru-O in plane	Ru-O out of plane
0	3.8624	12.4845	0.3534	0.1636	1.9312	2.042
1	3.901	12.4092	0.3541	0.1639	1.9505	2.033
2	3.9396	12.3277	0.3551	0.164	1.9698	2.021
3	3.978	12.2507	0.3560	0.1642	1.9891	2.0121

Biaxial Strain, Sr_2RuO_4 VASP LDA, c and ions relaxed 123

strain (%)	a (fixed)	c	z_{Sr}	z_{O1}	Ru-O in plane	Ru-O out of plane
0	3.8624	12.8344	0.3525	0.1612	1.9312	2.068
2	3.9396	12.654	0.3541	0.1615	1.9698	2.043
3	3.9782	12.5595	0.3551	0.1615	1.989	2.0288

Biaxial Strain, Sr_2RuO_4 ABINIT PBE (GGA), c and ions relaxed

Pressure (GPa)	a (fixed)	c (fixed)	z_{Sr}	z_{O1}	Ru-O in plane	Ru-O out of plane
-10	3.942	13.03126	0.353	0.16020	1.970	2.0877
-1	3.868	12.74686	0.353	0.16230	1.9341	2.068
0	3.86	12.7153	0.3529	0.1625	1.93	2.0663
1	3.8518	12.6837	0.3528	0.16270	1.9218	2.0611
10	3.778	12.3993	0.3527	0.1644	1.889	2.0379

Hydrostatic Pressure, Sr_2RuO_4 VASP LDA, a and c fixed to values in PRB 57 5067 (1998)

strain (%)	a (fixed)	c	z_{Sr}	z_{O1}	Ru-O in plane	Ru-O out of plane
-3	3.8703	13.4029	0.353	0.15454	1.9352	2.071
-2	3.9102	13.3143	0.353	0.15484	1.9551	2.061
-0.75	3.96	13.2013	0.354	0.15512	1.98	2.0478
2	4.0698	12.9556	0.3560	0.15550	2.0349	2.0146

Biaxial Strain, Ba_2RuO_4 VASP LDA, c and ions relaxed

strain (%)	a (fixed)	c	z_{Sr}	z_{O1}	Ru-O in plane	Ru-O out of plane
-3	3.8703	13.6268	0.353	0.154044	1.93515	2.099
-2	3.9102	13.5318	0.353	0.15435	1.9551	2.0887
-1	3.9501	13.4397	0.354	0.15465	1.97505	2.0784
1	4.0299	13.2500	0.355	0.154981	2.01495	2.0534
2	4.0698	13.1569	0.355	0.15508	2.0349	2.0404

Biaxial Strain, Ba_2RuO_4 VASP PBEsol, c and ions relaxed

Table A.1: Structural parameters

APPENDIX B

Calculation of the energy eigenstates

In this Appendix we provide the programming code that was used to find the eigenstates and eigenvalues of the two-site and four-site systems in chapter 8. We first express the Hamiltonian in the second-quantized form. Then, we generate the occupation basis states and calculate the matrix elements. Finally, the Hamiltonian is diagonalized using the standard built-in routines.

```
import numpy as np
from scipy.special import factorial
from numpy.linalg import eigh
from scipy.sparse.linalg import eigsh
import matplotlib.pyplot as plt
import blockdiag
import timeit

def generate_orb_states(n_el, n_sites):
    if n_el == 0:
        return np.zeros((1, n_sites))
    elif n_el == n_sites:
        return np.ones((1, n_sites))
    else:
        states = np.zeros((0, n_sites))
        for last_pos in range(n_el-1, n_sites):
            tmp = generate_orb_states(n_el-1, last_pos)
            ones_arr = np.ones((tmp.shape[0], min(1,n_sites-last_pos)))
            zeros_arr = np.zeros((tmp.shape[0], max(0,n_sites-1-last_pos)))
            tmp1 = np.concatenate((np.concatenate((tmp,ones_arr),axis=1),zeros_arr),axis=1)
            states = np.concatenate((states, tmp1), axis=0)
        return states

def generate_all_states(n_orb_spin, n_sites):
```

```
    xyup = generate_orb_states(n_orb_spin[0], n_sites)
    xzup = generate_orb_states(n_orb_spin[1], n_sites)
    yzup = generate_orb_states(n_orb_spin[2], n_sites)
    xydn = generate_orb_states(n_orb_spin[3], n_sites)
    xzdn = generate_orb_states(n_orb_spin[4], n_sites)
    yzdn = generate_orb_states(n_orb_spin[5], n_sites)
    n_states = xyup.shape[0]*xzup.shape[0]*yzup.shape[0]*xydn.shape[0]*xzdn.shape[0]*yzdn.shape
        [0]
    states = np.zeros((n_states, 6*n_sites))
    k = 0
    for k0 in range(xyup.shape[0]):
        for k1 in range(xzup.shape[0]):
            for k2 in range(yzup.shape[0]):
                for k3 in range(xydn.shape[0]):
                    for k4 in range(xzdn.shape[0]):
                        for k5 in range(yzdn.shape[0]):
                            states[k, 0:n_sites] = xyup[k0]
                            states[k, n_sites:2*n_sites] = xzup[k1]
                            states[k, 2*n_sites:3*n_sites] = yzup[k2]
                            states[k, 3*n_sites:4*n_sites] = xydn[k3]
                            states[k, 4*n_sites:5*n_sites] = xzdn[k4]
                            states[k, 5*n_sites:6*n_sites] = yzdn[k5]
                            k+=1
    return states

def onsite_energy(state, U, J):
    n_sites = state.shape[0]/6
    energy = 0
    for k in range(n_sites):
        n_el = np.sum(state[k::n_sites])
        n_up = np.sum(state[k:3*n_sites:n_sites])
        n_dn = np.sum(state[3*n_sites+k:6*n_sites:n_sites])
        energy += (U-1.5*J)*0.5*n_el*(n_el-1) - 0.25*J*(n_up-n_dn)**2
    return energy

def Kanamori_diag_energy(state, U, J):
    n_sites = state.shape[0]/6
    energy = 0
    for k in range(n_sites):
        siteoccup = state[k::n_sites]
```

```
64          energy += U*(siteoccup[0]*siteoccup[3]+siteoccup[1]*siteoccup[4]+siteoccup[2]*siteoccup
                [5]) #U
65          energy += (U-3*J)*(siteoccup[0]*(siteoccup[1]+siteoccup[2])+siteoccup[1]*siteoccup[2]) #
                up's
66          energy += (U-3*J)*(siteoccup[3]*(siteoccup[4]+siteoccup[5])+siteoccup[4]*siteoccup[5]) #
                dn's
67          energy += (U-2*J)*(siteoccup[0]*(siteoccup[4]+siteoccup[5])+siteoccup[1]*(siteoccup[3]+
                siteoccup[5])+siteoccup[2]*(siteoccup[3]+siteoccup[4])) #up-dn
68      return energy
69
70  def Kanamori_offdiag_energy(state1, state2, J):
71      statediff = state1 - state2
72      if np.sum(np.abs(statediff))!=4 or np.sum(statediff)!=0:
73          return 0.
74      n_sites = state1.shape[0]/6
75      diffind = np.argwhere(statediff)
76      siteind = np.mod(diffind[0],6)
77      orb_occup_diff = statediff[siteind::n_sites]
78
79      if np.sum(orb_occup_diff[0:3])!=0 or np.sum(np.abs(orb_occup_diff[0:3]))!=2 or np.sum(
            orb_occup_diff[3:6])!=0 or np.sum(np.abs(orb_occup_diff[3:6]))!=2:
80          return 0. #
81      if all(orb_occup_diff[0:3]==-orb_occup_diff[3:6]):
82          return J
83      elif all(orb_occup_diff[0:3]==orb_occup_diff[3:6]):
84          return J
85      else:
86          return 0.
87
88  def nn_hopping_term(state1, state2, site_coords): #nearest neighbor hopping
89      statediff = state1 - state2
90      if np.sum(np.abs(statediff))!=2:
91          return 0.
92      else:
93          diff1 = np.argwhere(statediff<0)
94          diff2 = np.argwhere(statediff>0)
95          if diff1/site_coords.shape[0] != diff2/site_coords.shape[0]: #changes in different
                orbitals (this should never occur at this point)
96              print 'smth wrong with states'
97              return 0.
```

```
98          orbital = diff1/site_coords.shape[0] # from 0 to 5: xy-up,xz-up,yz-up,xy-dn,xz-dn,yz-dn
99          coord1 = np.mod(diff1,site_coords.shape[0])
100         coord2 = np.mod(diff2,site_coords.shape[0])
101
102         if (np.abs(site_coords[coord1] - site_coords[coord2])==np.array([1,0,0])).all() and
                orbital in [0,1,3,4]:
103             return -1.
104         elif (np.abs(site_coords[coord1] - site_coords[coord2])==np.array([0,1,0])).all() and
                orbital in [0,2,3,5]:
105             return -1.
106         elif (np.abs(site_coords[coord1] - site_coords[coord2])==np.array([0,0,1])).all() and
                orbital in [1,2,4,5]:
107             return -1.
108         else:
109             return 0.
110
111 def exchange_diag_energy(state, Jex):
112     # Jex > 0 FM, Jex<0 AFM
113     n_sites = state.shape[0]/6
114     thisbasis = state.reshape(6,n_sites)
115     spins = np.sum(thisbasis[0:3,]-thisbasis[3:6,],axis=0)*0.5
116     energy = -Jex*np.sum(spins*np.roll(spins,1))
117     return energy
118
119 def calc_eigenstates(site_coords, n_orb_spin, U, J, Jex, tvals):
120     if site_coords.shape[1]==2:
121         site_coords = np.concatenate((site_coords, np.zeros((site_coords.shape[0],1))),axis=1)
122     n_sites = site_coords.shape[0]
123     states = generate_all_states(n_orb_spin, n_sites)
124     n_states = states.shape[0]
125
126     Hamilt_kanamori = np.zeros((n_states, n_states))
127     Hamilt_hop = np.zeros((n_states, n_states))
128     for k in range(n_states):
129         Hamilt_kanamori[k,k] = Kanamori_diag_energy(states[k,:], U, J) + exchange_diag_energy(
                states[k,:], Jex)
130
131     total_hop=0
132     for k0 in range(n_states):
133         for k1 in range(k0):
```

```
            hop = nn_hopping_term(states[k0,:], states[k1,:], site_coords)
            kanamoffdiag = Kanamori_offdiag_energy(states[k0,:], states[k1,:], J)
            Hamilt_kanamori[k0,k1] = kanamoffdiag
            Hamilt_kanamori[k1,k0] = kanamoffdiag
            Hamilt_hop[k0,k1] = hop
            Hamilt_hop[k1,k0] = hop
            total_hop += hop

    print total_hop
    print n_states

    eigvals = np.zeros((tvals.size, n_states))
    eigvecs = []
    k=0

    for t in tvals:
        Hamilt = Hamilt_kanamori + t*Hamilt_hop
        [w, v] = eigh(Hamilt)
        eigvals[k] = w
        eigvecs.append(v)
        k+=1

    return eigvals, eigvecs, states

def calc_avg_spin(w,v,basis):
    #calculates spin per site in
    basis_spin=np.zeros((basis.shape[0]))
    basis_spin_correl=np.zeros((basis.shape[0]))
    n_sites = basis.shape[1]/6
    for k in xrange(basis.shape[0]):
        thisbasis = basis[k,:].reshape(6,n_sites)
        spins = np.sum(thisbasis[0:3,]-thisbasis[3:6,],axis=0)*0.5
        basis_spin[k] = np.mean(np.abs(spins))
        basis_spin_correl[k] = np.mean(spins*np.roll(spins,1))

    avg_spin = np.zeros((w.shape[0]))
    avg_spin_correl = np.zeros((w.shape[0]))
    totweight = np.zeros((w.shape[0]))
    for k in xrange(w.shape[0]):
        for m in xrange(basis.shape[0]):
```

```
174             avg_spin[k] += v[k][m,0]**2*basis_spin[m]
175             avg_spin_correl[k] += v[k][m,0]**2*basis_spin_correl[m]
176             totweight[k] += v[k][m,0]**2
177
178     return (avg_spin, avg_spin_correl, totweight, basis_spin)
```

References

[1] J. P. Locquet *et al.*, *Nature* **394**, 453 (1998).

[2] K. J. Choi *et al.*, *Science* **306**, 1005 (2004).

[3] J. H. Lee *et al.*, *Nature* **466**, 954 (2010).

[4] H. K. Yoo *et al.*, *Sci. Rep.* **5**, 8746 (2015).

[5] Y. Maeno *et al.*, *Nature* **372**, 532 (1994).

[6] S. A. Grigera *et al.*, *Science* **294**, 329 (2001).

[7] R. A. Borzi *et al.*, *Science* **315**, 214 (2007).

[8] C. Lester *et al.*, *Nat. Mater.* **14**, 1 (2015).

[9] J. M. Longo *et al.*, *J. Appl. Phys.* **39**, 1327 (1968).

[10] S. Nakatsuji *et al.*, *Phys. Rev. Lett.* **84**, 2666 (2000).

[11] J. P. Carlo *et al.*, *Nat. Mater.* **11**, 323 (2012).

[12] Hertz H., *Ann. Physik* **31**, 983 (1887).

[13] W. Hallwachs, *Wiedmannsche Annalen* **33**, 301–312 (1888).

[14] J. J. Thompson, *Phil. Mag.* **48**, 547 (1899).

[15] P. Lenard, *Ann. Physick* **2**, 359 (1900).

[16] *Ann. Physik* **17**, 132 (1905).

[17] R.A. Millikan, *Phys. Rev.* **7**, 355 (1916).

[18] G. Beck, *Z. Phys.* **41**, 443 (1927).

[19] G. Wentzel, *Z. Phys.* **41**, 828 (1927).

[20] J. R. Oppenheimer *Z. Phys.* **41**, 268 (1927).

[21] K. Siegbahn *et al.*, Atomic, Molecular and Solid State Structure Studied by Means of Electron Spectroscopy. *Almqvist and Wiksells* (1967).

[22] C. Nordling, E. Sokolowski, and K. K. Siegbahn, *Phys. Rev.* **105**, 1676 (1957).

[23] K. Siegbahn *et al.*, ESCA Applied to Free-Molecules. *North-Holland* (1969).

[24] M. I. Al-Joboury *et al.*, *J. Chem. Soc.* **616**, 4434 (1965).

[25] D.W. Turner *et al.*, Molecular Photoelectron Spectroscopy. *Wiley Interscience* (1970).

[26] D.W. Turner and MI. Al-Joboury, *J. Chem. Phys.* **37**, 3007 (1962).

[27] C. N. Berglund and W. E. Spicer, *Phys. Rev.* **136**, A1030 (1964).

[28] G.W. Gobeli *et al.*, *Phys. Rev. Lett.* **12**, 94 (1964).

[29] E. O. Kane, *Phys. Rev. Lett.* **12**, 97 (1964).

[30] S. Huefner. Photoemission Spectroscopy, Principles and Applications. *Springer* (2003).

[31] Mahan, G. D., *Phys. Rev. B* **2**, 4334 (1970).

[32] Liebsch, A., *Phys. Rev. B* **13**, 544 (1976).

[33] Seah, M. P. and Dench, W. A., *Surf. Interface Anal.* **1**, 2 (1979).

[34] D.A. Shirley, *Phys. Rev.* **55**, 4709 (1972).

[35] A.A. Abrikosov, L.P. Gorkov, I.E. Dzyaloshinskii, Quantum Field Theoretical Methods in Statistical Physics. *Pergamon Press*, Oxford (1965).

[36] G.D. Mahan, Many-Particle Physics *Plenum Press*, New York (1981).

[37] G. Rickayzen, Green's Functions and Condensed Matter in Techniques of Physics, v. 7 *Academic Press*, London (1991).

[38] A. Dmascelli, *Rev. Mod. Phys.* **75**, 473 (2003).

[39] H. Iwasawa *et al.*, *Phys. Rev. Lett* **109**, 066404 (2012).

[40] A. Georges *et al.*, *Annu. Rev. Condens. Matter Phys.* **4**, 137 (2013).

[41] J. J. Randall and R. Ward, *J. American Chem. Soc.* **81**, 2629 (1959).

[42] A. Callaghan *et al.*, *Inorg. Chem.* **5**, 1572 (1966).

[43] J. M. Longo, P. M. Raccah, and J. B. Goodenough, *J. Appl. Phys.*, **39**, 1327 (1968).

[44] R. J. Bouchard and J. L. Gilson, *Mat. Res. Bull.*, **7**, 873 (1972).

[45] J. A. Kafalas and J. M. Longo, *J. Solid State Chem.* **4**, 55 (1972).

[46] J. G. Bednorz and K. A. Muller, *Z. Phys. B* **64**, 189 (1986).

[47] C. B. Eom *et al.*, *Science*, **258**, 1766 (1992).

[48] Y. Maeno *et al.*, *Nature*, **372**, 532 (1994).

[49] A. P. Mackenzie, *Phys. Rev. Lett.* **76**, 3786 (1996).

[50] T. Oguchi, *Phys. Rev. B* **51**, 1385 (1995).

[51] T. M. Rice and M. Sigrist, *J. Phys. :Condens. Matter*, **7**, L643-L648 (1995).

[52] K. Ishida, H. Mukuda, Y. Kitaoka, K. Asayama, Z. Mao, Y. Mori, and Y. Maeno, *Nature* **396**, 658 (1998).

[53] K. Ishida, H. Mukuda, Y. Kitaoka, Z. Q. Mao, Y. Mori, and Y. Maeno, *Phys. Rev. Lett.* **84**, 5387 (2000).

[54] H. Murakawa, K. Ishida, K. Kitagawa, Z. Q. Mao, and Y. Maeno, *Phys. Rev. Lett.* **93**, 167004 (2004).

[55] J. A. Duffy, S. M. Hayden, Y. Maeno, Z. Mao, J. Kulda, and G. J. McIntyre, *Phys. Rev. Lett.* **85**, 5412 (2000).

[56] G. Luke *et al.*, *Nature* **394**, 558 (1998).

[57] . Jing Xia *et al.*, *Phys. Rev. Lett.* **97**, 167002 (2006).

[58] S. A. Grigera *et al.*, *Science* **294**, 329 (2001).

[59] C. Lester *et al.*, *Nat. Mater.* **14**, 373 (2015).

[60] R. A. Borzi *et al.*, *Science* **315**, 214 (2007).

[61] V. I. Anisimov *et al.*, *Eur. Phys. J. B* **25**, 191-201 (2002).

[62] S. Nakatsuji and Y. Maeno, *Phys. Rev. Lett.* **84**, 2666 (2000).

[63] J. P. Carlo *et al.*, *Nat. Mater.* **11**, 323 (2012).

[64] M. Zhu *et al.*, *Phys. Rev. Lett.* **116**, 216401

[65] R. D. Shannon *Acta Crystallogr A* **32**, 751-767 (1976).

[66] C. -Q. Jin *et al.*, *PNAS*, **105**, 7115-7119 (2007).

[67] I. I. Mazin and D. J. Singh *Phys. Rev. Lett* **79**, 733 (1997).

[68] Carter S A *et al.*, *Phys. Rev. B* **51** 17184 (1995).

[69] A. P. Mackenzie and Y. Maeno, *Rev. Mod. Phys.*, **75** 657 (2003).

[70] Y. Jia *et al.*, *Appl. Phys. Lett.* **74**, 3830 (1999).

[71] D.G. Schlom *et al.*, *SPIE* **3481**, 226 (1998).

[72] W. Tian, X.Q. Pan, J.H. Haeni, D.G. Schlom, *J. Mater. Res.* **16**, 2013 (2001).

[73] Che-Hui Lee *et al.*, *Appl. Phys. Lett.* **102**, 122901 (2013).

[74] M. A. Zurbuchen, Y. Jia, S. Knapp, A. H. Carim, D. G. Schlom, X. Q. Pan. *Appl. Phys. Lett.* **83**, 3891 (2003).

[75] M.A. Zurbuchen, W. Tian, X.Q. Pan, D. Fong, S.K. Streiffer, M.E. Hawley, J. Lettieri, Y. Jia, G. Asayama, S.J. Fulk, D.J. Comstock, S. Knapp, A.H. Carim, D.G. Schlom. *J. Mat. Res.* **22**, 1439 (2007).

[76] Y. Krockenberger, M. Uchida, K. S. Takahashi, M. Nakamura, M. Kawasaki, Y. Tokura, *Appl. Phys. Lett.* **97**, 082502 (2010).

[77] Schlom, D. G. *et al.*, **91**, 2429–2454 (2008).

[78] L. Waltz, F. Lichtenberg, *Acta Crystallogr., Sect. C: Cryst. Struct. Commun.* **49**, 1268 (1993).

[79] R. Uecker *et al.*, *Acta Phys. Pol., A* **124**, 295 (2013).

[80] J. Kafalas *et al.*, *J. Solid State Chem.* **4**, 55 (1972).

[81] D. G. Schlom *et al.*, *MRS Bulletin* **39**, 118 (2014).

[82] A. Damascelli *et al.*, *Phys. Rev. Lett.* **85**, 5194 (2000).

[83] K. M. Shen *et al.*, *Phys. Rev. B* **64**, 180502 (2001).

[84] Y. Krockenberger *et al.*, *Appl. Phys. Lett.* **97**, 082502 (2010).

[85] L. J. van der Pauw, *Philips Technical Review* **20**, 220-224 (1958).

[86] E. P. Abrahams *et al.*, *Phys. Rev. B* **24**, 6783 (1981).

[87] Y. Maeno *et al.*, *J. Phys. Soc. Jpn.* **81** 011009 (2012).

[88] G. E. Volovik and L. P. Gorkov, *Zh. Eksp. Teor. Fiz.* **88**, 1412-1428 (1985).

[89] Maki K. *et al.*, *Supercond. Nov. Magn.* **22**, 71 (2009).

[90] H. Mukuda *et al.*, *J. Phys. Soc. Jpn.* **67** 3945 (1998).
[91] H. Mukuda *et al.*, *Phys. Rev. B* **60** 12279 (1999).
[92] H. Murakawa *et al.*, *J. Phys. Soc. Jpn.* **76** 024716 (2007).
[93] K. Ishida *et al.*, *J. Phys. Chem. Solids* **69**, 3108 (2008).
[94] K. Deguchi *et al.*, *Phys. Rev. Lett.* **92**, 047002 (2004).
[95] K. D. Nelson *et al.*, *Science* **306**, 1151 (2004).
[96] M. Rice, *Science* **306**, 1142 (2004).
[97] J. Xia *et al.*, *Appl. Phys. Lett.*, **89** 062508 (2006).
[98] Y. Ueno *et al.*, *Phys. Rev. Lett.* **111**, 087002 (2013).
[99] P. M. R. Brydon *et al.*, *Phys. Rev. Lett.* **104**, 197001 (2010).
[100] Bergemann C. *et al.*, *Physica B* **294**, 371 (2001).
[101] Maeno, Y. *et al.*, *Physica C* **282**, 206 (1997).
[102] G. R. Stewart, *Rev. Mod. Phys.* **56**, 755 (1984).
[103] Maeno, Y. *et al.*, *J. Phys. Soc. Jpn.* **66**, 1405 (1997).
[104] A. Damascelli *et al.*, *Phys. Rev. Lett.* **85**, 5194–5197 (2000).
[105] J. Mravlje *et al.*, *Phys. Rev. Lett.* **106**, 096401 (2011).
[106] Ohmichi, E. *et al.*, *Phys. Rev. B* **61**, 7101 (2000).
[107] Mackenzie, A. P. *et al.*, *Phys. Rev. Lett.* **80**, 3890 (1996).
[108] Yoshida, Y. *et al.*, *J. Phys. Soc. Jpn.* **67**, 2551 (1998).
[109] Bergemann C. *et al.*, *Phys. Rev. Lett.* **84**, 2662 (2000).
[110] D. J. Singh *Phys. Rev. B*, **52** 1358 (1995).
[111] Mazin, I. I. *et al.*, *Phys. Rev. B* **61**, 5223 (2000).
[112] P. K. de Boer and R. A. de Groot, *Phys. Rev. B* **59**, 9894 (1999).
[113] A. Fang and K. Terakura, *Phys. Rev. B* **64**, R020509 (2001).
[114] S.-I. Ikeda *et al.*, *J. Phys. Soc. Jpn.* **73**, 1322-1325 (2004).
[115] H. Yaguchi *et al.*, *AIP Conf. Proc.* **850**, 1203 (2006).
[116] C. N. Veenstra *et al.*, *Phys. Rev. Lett.* **110**, 097004 (2013).
[117] R. Matzdorf *et al.*, *Science* **289**, 746 (2000).
[118] R. D. Shannon *et al.*, *Acta Crystallogr. Sect. A* **32**, 751 (1976).
[119] M. W. Haverkort *et al.*, *Phys. Rev. Lett.* **101**, 026406 (2008).
[120] A. P. Mackenzie *et al.*, *Phys. Rev. B* **54**, 7425 (1996).
[121] C. Bergemann *et al.*, *Adv. Phys.* **52**, 639 (2003).
[122] K. M. Shen *et al.*, *Phys. Rev. Lett.* **99**, 187001 (2007).

[123] N. Kikugawa *et al.*, *Phys. Rev. B* **70**, 134520 (2004).

[124] A. P. Mackenzie *et al.*, *Phys. Rev. Lett.* **80**, 161 (1998).

[125] N. E. Hussey *et al.*, *Phys. Rev. B* **57**, 5505 (1998).

[126] A. P. Mackenzie *et al.*, *Phys. Rev. Lett.* **80**, 161 (1998).

[127] C. Bergemann *et al.*, *Phys. Rev. Lett.* **84**, 2662 (2000).

[128] V. B. Zabolotnyy *et al.*, arXiv:1212.3994 (2013).

[129] C. Bergemann, A. P. Mackenzie, S. R. Julian, D. Forsythe, and E. Ohmichi, *Adv. Phys.*, **52**, 639-725 (2003).

[130] S. Hill, J. S. Brooks, Z. Q. Mao, and Y. Maeno, *Phys. Rev. Lett.* **84**, 3374-3377 (2000).

[131] A. Liebsch and A. Lichtenstein, *Phys. Rev. Lett.* **84**, 1591 (2000).

[132] G. R. Stewart, *Rev. Mod. Phys.* **83**, 1589 (2011).

[133] N. Shirakawa *et al.*, *Phys. Rev. B* **56**, 7890 (1997).

[134] D. Forsythe *et al.*, *Phys. Rev. Lett.* **89**, 166402 (2002).

[135] D. M. Newns, H. R. Krishnamurthy, P. C. Pattnaik, C. C. Tsuei, and C. L. Kane, *Phys. Rev. Lett.* **69**, 1264 (1992).

[136] R.S Markiewicz, *J. Phys. Chem. Solids* **58**, 1179-1310 (1997).

[137] K. Gofron, J. C. Campuzano, A. A. Abrikosov, M. Lindroos, A. Bansil, H. Ding, D. Koelling, and B. Dabrowski, *Phys. Rev. Lett.* **73**, 3302 (1994).

[138] Gonzalez, J., *Phys. Rev. B* **78**, 205431 (2008).

[139] R. Nandkishore, L. S. Levitov and A. V. Chubukov, *Nature Physics* **8**, 158-163 (2012).

[140] J. L. McChesney, Aaron Bostwick, Taisuke Ohta, Thomas Seyller, Karsten Horn, J. Gonzalez, and Eli Rotenberg, *Phys. Rev. Lett.* **104**, 136803 (2010).

[141] P. A. Igoshev, A. A. Katanin, H. Yamase, V. Yu. Irkhin, *J. Mag. Mag. Phenom. 321*, 899-902 (2009).

[142] E. C. Stoner, *Proc. Royal Soc. A: Math. Phys. Eng. Sc.* **165**, 372 (1938).

[143] J. Mravlje *et al.*, *Phys. Rev. Lett.* **106**, 096401 (2011).

[144] P. Monthoux and G. G. Lonzarich, *Phys. Rev. B* **71**, 054504 (2005).

[145] S. Raghu *et al.*, *Phys. Rev. Lett.* **105**, 136401 (2010).

[146] Y. Hsu *et al.*, *Phys. Rev. B* **94**, 045118 (2016).

[147] C. W. Hicks *et al.*, *Science* **344**, 283 (2014).

[148] J-H She et.al., arXiv:1603.0292 (2016).

[149] Xia J. *et al.*, *Phys. Rev. B* **79**, 140407(R). (2009).

[150] Shen X. *et al.*, *J. Appl. Phys.* **117**, 015307 (2015).

[151] P. D. C. King, H. I. Wei, Y. F. Nie, M. Uchida, C. Adamo, S. Zhu, X. He, I. Bozovic, D. G. Schlom, K. M. Shen, *Nature Nanotechnology* 9, 443-447 (2014).

[152] Y. J. Chang, C. H. Kim et al., *Phys. Rev. Lett.* 103, 057201 (2009).

[153] D. E. Shai *et al.*, *Phys. Rev. Lett.* **110**, 087004 (2013).

[154] H. F. Yang, C. C. Fan, Z. T. Liu, Q. Yao, M. Y. Li, J. S. Liu, M. H. Jiang, D. W. Shen, *Phys. Rev. B* 94, 115151 (2016).

[155] J. -S. Zhou *et al.*, *Phys. Rev. Lett.* **101**, 077206 (2008).

[156] C. -Q. Jin *et al.*, *Proc. Natl. Acad. Sci.* **105**, 7115 (2008).

[157] M. K. Lee *et al.*, *Appl. Phys. Lett.* **78**, 329 (2001).

[158] L. Abbes *et al.*, *Results in Physics*, **5**, 38 (2015).

[159] M. Kobayashi *et al.*, *Phys. Rev. Lett.* **115**, 076801 (2015).

[160] R. Scherwitzl *et al.*, *Phys. Rev. Lett.* **106**, 246403 (2011).

[161] Mermin, N. D. ; Wagner, H. , *Phys. Rev. Lett.* **17**, 1133 (1966).

[162] Hohenberg, P. C. , *Phys. Rev.* **158** 383 (1967).

[163] Bert, J. A. *et al.*, *Nat. Phys.* **7**, 767 (2011).

[164] Brinkman, A. *et al.*, *Nat. Mater.* **6**, 493 (2007).

[165] Dikin, D. A. *et al.*, *Phys. Rev. Lett.* **107**, 056802 (2011).

[166] J.-G. Cheng *et al.*, *Proc. Natl. Acad. Sci.* **110**, 13312-13315 (2013).

[167] A. Kanbayasi *et al.*, *J. Phys. Soc. Jpn.* **41**, 1876 (1976).

[168] Gan, Q. , R. A. Rao, C. B. Eom, J. L. Garrett, and M. Lee, *Appl. Phys. Lett.* **72**, 978 (1998).

[169] Allen, P. B. , H. Berger, O. Chauvet, L. Forro, T. Jarlborg, A. Junod, B. Revaz, and G. Santi, *Phys. Rev. B* **53**, 4393 (1996).

[170] J. S. Ahn *et al.*, *Phys. Rev. Lett.* **82**, 5321 (1999).

[171] Singh, D. J. , *J. Appl. Phys.* **79**, 4818 (1996).

[172] G. Koster *et al.*, *Rev. Mod. Phys.* **84**, 253 (2012).

[173] A. Arrott, *Phys. Rev* **108**, 1394 (1957).

[174] E. P. Wohlfarth, *J. Appl. Phys.* **39**, 1061 (1968).

[175] D. Kim *et al.*, *Phys. Rev. B* **67**, 100406 (2003).

[176] L. Klein *et al.*, *Phys. Rev. Lett.* **77**, 2774 (1996).

[177] I. I. Mazin and D. J. Singh, *Phys. Rev. B* **56**, 2556 (1997).

[178] Middley S. *et al.*, *Phys. Rev. B* **83**, 014416 (2011).

[179] H. T. Dang *et al.*, *Phys. Rev. B* **91**, 195149 (2015).

[180] Han Q. *et al.*, *Phys. Rev. B* **93**, 155103 (2016).

[181] Ranjan R. *et al.*, *Appl. Phys. Lett.* **90**, 251913 (2007).

[182] Kolesnik S. *et al.*, *Phys. Rev. B* **78**, 214425 (2008).

[183] T. Moriya. Spin Fluctuations in Itinerant Electron Magnetism, *Springer-Verlag*, Berlin

(1985).

[184] P. Langevin, *J. Phys.* **4**, 678 (1905).

[185] P. Weiss, *J. Phys. Radium* **6**, 661 (1907).

[186] M. Higashiguchi *Phys. Rev. B* **72**, 214438 (2005).

[187] T. Moriya and A. Kawabata, *J. Phys. Soc. Jpn.* **34**, 639 (1973).

[188] Yi Li *et al.*, *Phys. Rev. Lett.* **112**, 217201 (2014).

[189] Yi Li, *Phys. Rev. B* **91**, 115122 (2015).

[190] M. Imada, A. Fujimori, and Y. Tokura, *Rev. Mod. Phys.* **70**, 1039 (1998).

[191] O. Nganba Meetei *et al.*, *Phys. Rev. B* **91**, 054412 (2015).

[192] P. E. Blöchl, *Phys. Rev. B* **50**, 17953 (1994).

[193] G. Kresse, J. Furthmüller, *Phys. Rev. B* **54**, 11169 (1996).

[194] Ortmann J. E. *et al.*, *Sci. Rep.* **3**, 2950 (2013).

[195] N. Kikugawa *et al.*, *Phys. Rev. B* **70**, 060508R (2004).

[196] W. L. McMillan and J.M. Rowell, *Phys. Rev. Lett.* **14**, 108–112 (1965).

[197] Y. A. Ying, *Nat. Comm.* **4**, 2596 (2013).

[198] Z. Q. Mao *et al.*, *Phys. Rev. Lett.* **90**, 186601 (2003).

[199] L. de Medici *et al.*, *Phys. Rev. Lett.* **107**, 256401 (2011).

[200] A. Steppke *et al.*, arXiv:1604.06669 (2016).

[201] T. Willimas *et al.*, *Mat. Res. Bull.*, **26**, 763 (1991).

[202] A. A. Abrikosov and L. P. Gor'kov, *Zh. Eksp. Teor. Fiz.* **39**, 1781 (1960).

[203] V. M. Goldschmidt, "Die Gesetze der Krystallochemie". *Die Naturwissenschaften* **21**, 477-485 (1926).

[204] S. Huefner. Very High Resolution Photoemission Spectroscopy. *Springer* (2007).

[205] H. K. Muller-Buchbaum and J. Wilkens, *Z. Anorg. Allg. Chem*, **591**, 161 (1990).

[206] Z. Q. Mao *et al.*, *Phys. Rev. B* **60**, 610 (1999).

[207] Oura K. *et al.*, Surface Science: An Introduction *Springer*, (2010).

[208] K. Maiti *et al.*, *Phys. Rev. B* **71**, 161102 (2005).

[209] I. I. Mazin *et al.*, *Phys. Rev. Lett.* **79**, 733 (1997).

[210] L. de Medici, J. Mravlje, and A. Georges, *Phys. Rev. Lett.* **107**, 256401 (2011).

[211] M. Minakata and Y. Maeno, *Phys. Rev. B* **63**, 180504(R) (2001).

[212] A. Damascelli, *Physica Scripta* **109**, 61 (2004).

[213] Neil W. Ashcroft, N. David Mermin, Solid State Physics. *Cengage Learning* (1976).

[214] C. Etz *et al.*, *Phys. Rev. B* **86**, 064441 (2012).

[215] H. Taniguchi, *J. Phys. Soc. Jpn.* **84**, 014707 (2015).

[216] M. de Broglie, *J. Phys et Rad.* **2**, 265 (1921).

[217] K. Siegbahn. Conf. of the Swedish nat. committee for physics, Stockholm. *Ark. Fys.* **7**, 86 (1954).

[218] F. Lichtenberg *et al.*, *Appl. Phys. Lett.*,**60**, 1138 (1992).

[219] J.-W. Huo *et al.*, *Phys. Rev. Lett.* **110**, 167003 (2013).

[220] P. D. Innes, *Proc. Royal Soc.* **79**, 442 (1907).